First-principles thermodynamic study of oxygen vacancies in ABO_3-type perovskites

Von der Fakultät Chemie der Universität Stuttgart
zur Erlangung der Würde eines

Doktors der Naturwissenschaften

(Dr. rer. nat.) genehmigte Abhandlung

Vorgelegt von
Marco Arrigoni
aus Bergamo, Italien

Hauptberichter:	Prof. Dr. Joachim Maier
Mitberichter:	Prof. Dr. Johannes Kästner
Prüfungsvorsitzender:	Prof. Dr. Anke Weidenkaff
Tag der Einreichung:	10.01.2017
Tag der mündlichen Prüfung:	22.02.2017

Max-Planck-Institut für Festkörperforschung

Stuttgart
2017

Erklärung

Die vorliegende Doktorarbeit wurde vom Autor selbst in der Abteilung von Prof. Joachim Maier am Max-Planck-Institut für Festkörperforschung, im Zeitraum von August 2013 bis Dezember 2016 angefertig. Der Inhalt ist die eigene Arbeit des Autors, Ausnahmen sind gekennzeichnet, und wurde noch nicht zur Erlangung einer Qualifizierung oder eines Titels an einer akademischen Institution eingerecht.

Stuttgart, 10. Januar 2017 Marco Arrigoni

Declaration

The work described in this thesis was carried out by the author in the Department of Prof. Joachim Maier at the Max Planck Institute for Solid State Research from August 2013 to December 2016. The contents are the original work of the author, except where indicated otherwise, and have not been previously submitted for any other degree or qualification at any academic institution.

Stuttgart, 10th January 2017 Marco Arrigoni

To my family.

Abstract

ABO_3-type perovskite oxides comprise a wide class of materials with numerous technological applications, ranging from optics to electrochemistry. The ideal perovskite structure is cubic, but this form usually exists only at high temperatures; while most perovskites have lower symmetry at room temperature and below. Oxygen vacancies are, perhaps, the most common intrinsic point defects observed in these compounds and their concentration can be increased by the introduction of acceptor impurities. It is well known that oxygen vacancies cause considerable changes in the electroconductivity and affect material hardening, aging and fatigue properties. For these reasons, particular emphasis has been given in recent decades to their study and characterization.

First-principles (*ab initio*) calculations have been extensively used in the last decade for describing the physical properties of perovskite oxides and oxygen vacancies therein. Such calculations offer a very useful source of information to accompany experimental measurements. The most common approximations to the density functional theory (DFT), namely the local density approximation (LDA) or the generalized gradient approximation (GGA), usually fail to predict important properties of these materials; such as the fundamental band gap and structural distortions. The reason lies in the strong electron-correlation effects, which arise from the partially filled d or f electron shells on the B-type transition metal ions. The most common solution to this problem has been the inclusion of a Hubbard-U term in the DFT Hamiltonian. This approach brings about an improvement to the description of the material ground-state properties; however the results can strongly depend on the chosen value of the U parameter. More recently hybrid functionals, which mix the DFT Hamiltonian with part of the Hartree-Fock non-local exchange, have proven to be able to accurately describe perovkite materials without relying on the U parameter. Since technological, specifically electrochemical, devices usually operate at elevated temperatures, the calculation of lattice vibrations, and their contribution to the material thermodynamics, offers a straightforward way to extend the standard DFT formalism beyond its zero-temperature limit. However, the computation of phonons in large systems, such as those necessary to correctly describe point defects, may require extensive computational resources. Furthermore,

the zero-temperature limit of standard DFT does not allow one to correctly evaluate phonon frequencies of the high-temperature cubic structure if phase transitions occur at lower temperatures, such as is the case for the anti-ferro-distortive transition in $SrTiO_3$ at 105 K.

From this point of view, $BaZrO_3$ can be considered as an ideal model compound for first-principles investigations of ABO_3 perovskites. As a matter of fact, it is one of a few perovskites which preserves the computationally desirable highly symmetric cubic structure down to very low temperatures. In addition, it possesses many remarkable properties, such as low thermal conductivity, high melting point and small thermal expansion coefficient, which make its study interesting also for technological applications. In particular, $BaZrO_3$ has attracted great interest as a promising high-temperature proton conductor, showing an excellent protonic conductivity after the introduction of trivalent acceptor dopants. The doping leads to the formation of charge-compensating oxygen vacancies, the presence of which allows for the absorption of water molecules from the atmosphere. The OH^- part of the H_2O molecule occupies the vacancy, while the remaining H^+ combines with a regular O^{2-} to form another OH^-. However, the segregation of oxygen vacancies toward the material grain boundaries is responsible for the formation of space charge zones which strongly decrease the bulk protonic conductivity. Recently, thin films of $BaZrO_3$ have shown to be particularly promising due to a very high crystalline quality and a low concentration of grain boundaries.

In the present study, we aim to investigate, by means of first-principles calculations and using $BaZrO_3$ as a model material, the properties of oxygen vacancies in ABO_3 perovskites in the limit of low concentrations and under realistic external conditions. In particular, we emphasize the contribution of lattice vibrations to the thermodynamic properties of point defects in both bulk solid, surfaces and thin films. For this purpose, we employ the Perdew-Burke-Ernzerhof functional mixed with a 25% of the Hartree-Fock exchange, known in the literature as PBE0, which has proven to give a very accurate description of the ground-state of ABO_3 perovskites. All the first-principles calculations are carried out with the computer code CRYSTAL which employs a localized basis set.

Firstly, we show that our computational setup predicts the main ground-state properties of $BaZrO_3$, such as the fundamental band gap, lattice parameter, dielectric constant and phonon frequencies, being in a very good agreement with the experimental data. Next, we consider the properties of oxygen vacancies in the bulk material, on surfaces and in thin films. In the latter case, we analyze how the film thickness affects the defect properties (confinement effects).

The oxygen vacancies are modeled with the supercell approach and we consider

the three different charge states that can occur in ABO_3 perovskites according to the external conditions: the neutral ($v_O^{\times}$), the singly-charged ($v_O^{\bullet}$) and the doubly-charged state ($v_O^{\bullet\bullet}$). For the bulk material, we calculate and compare the formation energy of each of these defects and we show that the most likely type of oxygen vacancy to occur is $v_O^{\bullet\bullet}$; while $v_O^{\bullet}$ and $v_O^{\times}$ appear only for a narrower energy range of the electron chemical potential. Due to the long range nature of the Coulomb interaction, proper correction schemes are applied to compensate the spurious electrostatic interactions between the periodically repeated array of charged defects which arises from the supercell method.

Due to the high computational costs, phonon frequencies are seldom explicitly calculated in defective solids; however, in this study we show that their contribution can noticeably affect the defect Gibbs energy of formation at high temperature. This is particularly true for $v_O^{\bullet\bullet}$, where we show that phonon contributions are responsible for the increase of the defect formation Gibbs energy by almost 1 eV at 1000 K, making the defect less energetically favorable than other charge states at high temperature.

Moreover, we show that lattice vibrations affect the relative stability of defective-free ABO_3 perovskite surfaces at high temperatures. In particular, we apply a simple thermodynamic model which makes some predictions about the relative stability of the two possible terminations of the $BaZrO_3$ (001) surface: BaO and ZrO_2. We find that, at room temperature and below, the BaO termination is the thermodynamically most stable one. However, at higher temperatures (around 500 K), the model predicts that both BaO and ZrO_2 terminations can coexist; and, at even higher temperatures (around 900 K), the ZrO_2 termination turns out to become the most stable.

Next, we consider two types of oxygen vacancies, $v_O^{\times}$ and $v_O^{\bullet\bullet}$, on the (001) surface of $BaZrO_3$ and calculate their segregation Gibbs energy, which indicates the defect tendency to migrate from the bulk to the surface. We find that lattice vibrations have an important contribution also in this case, giving rise to a positive segregation entropy which stabilizes the surface $v_O^{\bullet\bullet}$ over the bulk defect, especially at high temperatures.

Lastly, we consider oxygen vacancies in extremely thin perovskite films, with a thickness in the range from approximately 0.4 to 1.3 nm (that is, between three and seven atomic planes), and we study the dimensional confinement effects on the defect properties. We find that, except for the thinnest films, the defect properties do not noticeably differ from the bulk, indicating that they are affected only by their nearest neighborhood.

In summary, the findings presented in this thesis demonstrate the importance of

lattice vibrations for evaluating the thermodynamic properties of point defects in perovskite oxides and their surfaces at relatively high temperatures. In particular, their inclusion is relevant for the calculation of the Gibbs formation and segregation energies of charged oxygen vacancies and for the determination of the relative thermodynamic stabilities of different surface terminations.

Zusammenfassung

Die zur Klasse der Perowskite (ABO_3-Typ) gehörigen Oxide umfassen eine große Bandbreite von Materialien, welche in einer Vielzahl von technischen Anwendungen - von der Optik bis hin zur Elektrochemie - verwendet werden. Im Idealfall kristallisieren Perowskite im kubischen Kristallsystem, jedoch liegt diese Struktur meist nur bei hohen Temperaturen vor; die meisten Perowskite weisen eine geringere Symmetrie bei und unterhalb von Raumtemperatur auf. Sauerstoffleerstellen sind die am vermutlich häufigsten vorzufindenden nativen Punkdefekte in dieser Art von Materialien. Durch die Einführung von Akzeptor-Störstellen kann die Konzentration dieser Leerstellen weiter erhöht werden. Da Sauerstoffleerstellen bekanntermaßen die elektrische Leitfähigkeit stark beeinflussen können, sowie Effekte auf das Aushärtungsverhalten, Altern und auf Ermüdungserscheinungen haben können, lag in den vergangenen Jahrzehnten ein besonderes Augenmerk der Forschung in diesem Gebiet auf der Untersuchung und Charakterisierung solcher Effekte.

Ab initio Berechnungen wurden in den letzten Jahren ausgiebig genutzt, um die physikalischen Eigenschaften von Oxiden der Perowskit-Klasse und der darin enthalten Sauerstoffleerstellen zu beschreiben. Informationen, die aus dieser Art von Berechnungen erhalten werden, sind reichhaltig und eignen sich gut, experimentell gewonnene Daten zu ergänzen. Gebräuliche Näherungen zur Dichtefunktionaltheorie (*density functional theory*, DFT) wie die lokale Dichtenäherung (*local density approximation*, LDA) oder das Nutzen eines Gradiententerms für den Ausgleich örtlicher Dichteschwankungen (*generalized gradient approximation*, GGA) ermöglichen es häufig nicht, wichtige physikalische Eigenschaften, wie z.B. die Bandlücke oder Strukturverzerrungen, vorauszusagen. Die Ursache dafür liegt in den starken elektronischen Korrelationseffekte, die auf Grund der teilweise besetzten *d*- oder *f*-Orbitale bei den Übergangsmetall Kationen auf B-Platz auftreten. Die gängige Herangehensweise zur Lösung dises Problems ist die Einführung des sogenannten Hubbard-U-Terms in die Hamilton-Operator der DFT Rechnung, wodurch eine bessere Beschreibung der Materialeigenschaften im Grundzustand ermöglicht wird. Dabei ist zu berücksichtigen, dass die Verlässlichkeit der Ergebnisse stark von den eingesetzten Werten für den U-Term abhängt. In den vergangenen Jahren haben sich darüber hinaus Hybridfunktionale, welche die Hamilton-Operator der DFT

Rechnung teilweise mit dem ortsunabhängigen Hartree-Fock-Austausch vereinen, als vom U-Term unabhängige Alternativen zur genauen Beschreibung von Perowskiten erwiesen. Da in der technischen Anwendung elektrochemischer Prozesse meist erhöhlte Arbeitstemperaturen herrschen, ist die Berechnung der Gitterschwingungsenergien und deren thermodynamische Beitragas zum Gesamtsystem ein geeigneter Ansatz zur Erweiterung der DFT Berechnung über den Nullpunkt der Temperatur hinaus. Die Berechnung von Phononen in Systemen hinreichender Größe, sodass Punktdefekte zuverlässig beschrieben werden könnten, würde einen erheblichen Rechenaufwand mit sich bringen. Darüber hinaus ist zu beachten, dass die Limitierung der Standard-DFT-Berechnung auf den Nullpunkt vor allem dann kritisch ist, wenn unterhalb der Arbeitstemperatur eine Phasenumwandlung stattfindet. Dies ist der Fall für $SrTiO_3$, bei dem sich ein antiferrodistortiver Übergang bei 105 K ereignet.

Basierend auf diesen Überlegungen eignet sich $BaZrO_3$ ideal als Modellverbindung für *ab initio* Untersuchungen von Perowskiten des ABO_3-Typs. Es handelt sich um einen der wenigen Perowskiten, welche ihre hochsymmetrische kubische Struktur bis zu sehr geringen Temperaturen beibehalten, was sich in Hinsicht auf die Berechenbarkeit besonders positiv auswirkt. Darüber hinaus besitzt $BaZrO_3$ einige bemerkenswerte Eigenschaften, welche es auch für die Anwendung interessant machen, wie eine geringe thermische Leitfähigkeit, einen hohen Schmelzpunkt und einen kleinen thermischen Expansionskoeffizienten. Besonders als Protonenleiter in Hochtemperaturanwendungen erweckte $BaZrO_3$ auf Grund seiner exzellenten Leitfähihkeit - nach Einführung von trivalenten Akzeptor-Dotierungen - in den vergangenen Jahren viel Aufsehen. Durch die Dotierung bilden sich ladungsausgleichende Sauerstoffleerstellen, wodurch die Absorption von Wassermolekülen aus der umgebenden Atmosphäre ermöglicht wird. Die Leerstelle wird daraufhin durch ein OH^- Ion besetzt, während sich das übrige H^+ Kation mit einem O^{2-} zu einem weiteren OH^- verbindet. Ein wichtiger Aspekt ist, dass sich auf Grund der räumlichen Trennung von Sauerstoffleerstellen in der Nähe von Korngrenzen dort Raumladungszonen ausbilden, welche die protonische Gesamtleitfähigkeit stark beeinträchen. Zuletzt haben sich deswegen dünne Bariumzirkonatfilme wegen ihrer hohen Kristallqualität und geringen Korngrenzenkonzentration als äußerst vielversprechend herausgestellt.

In der vorliegenden Studie versuchen wir mittels *ab initio* Berechnungen und unter Verwendung von $BaZrO_3$ als Modellverbindung die Eigenschaften von Sauerstoffleerstellen in ABO_3 Perowskiten am realistischen Limit geringer Konzentrationen und unter realistischen äußeren Bedingungen zu untersuchen. Dabei heben wir den Beitrag der Gitterschwingungsenergie zu den thermodynamischen Eigenschaften von Punktdefekten im Volumen, an Oberflächen und für dünne Filme besonders

hervor. Hierfür verwenden wir das Perdew-Burke-Ernzerhof- (PBE) Funktional gemischt mit 25% des Hartree-Fock-Austausch - in der Literatur als PBE0 bekannt - welches äußerst präzise Beschreibungen des Grundzustands von ABO_3 Perowskiten ermöglichen sollte. Alle *ab initio* Berechnungen werden mit Hilfe des CRYSTAL-Codes durchgeführt, welcher ein lokalisiertes Basis-Set verwendet.

Zunächst zeigen wir, dass unsere Berechnungsgrundlagen geeignet sind, die Haupteigenschaften von $BaZrO_3$ im Grundzustand wie Bandlücke, Gitterparameter, dielektrische Konstante, und Phononenfrequenzen vorherzusagen, und dass die Ergebnisse in sehr guter Übereinstimmung mit experimentell gewonnen Daten stehen. Darauf aufbauend untersuchen wir die Eigenschaften der Sauerstoffleerstellen im Volumenmaterial, an Oberflächen, und in dünnen Filmen. Auch der Effekt der Dicke der Filme auf die Eigenschaften der Leerstellen wird analysiert. Die Sauerstoffleerstellen werden gemäß des Superzellen-Ansatzes modelliert und alle drei unterschiedlichen Ladungszustände, die in einem ABO_3 Perowskit in Abhängigkeit von den äußeren Bedingungen auftreten können, berücksichtigt: der neutrale Zustand ($v_O^\times$), den einfach geladenen ($v_O^\bullet$), sowie den zweifach geladenen Zustand ($v_O^{\bullet\bullet}$). Für das Volumenmaterial berechnen und vergleichen wir die Bildungsenergien jeder dieser Defekte und zeigen, dass der am wahrscheinlichsten auftretende Defekttyp der zweifach geladene, $v_O^{\bullet\bullet}$, ist, während der einfach geladene, $v_O^\bullet$, und der ungeladene, $v_O^\times$, lediglich in bestimmten Bereichen des Fermi-Niveau vorkommen. Die Langreichweitigkeit von coulombschen Wechselwirkungen macht die Verwendung geeigneter Korrekturmodelle zur Kompensierung der auf Grund der Superzellenmethode zwischen sich periodisch wiederholenden Gittern aus geladenen Defekten auftretenden, unerwünschten elektrostatischen Wechselwirkungen notwendig. Wegen des großen Rechenaufwands werden Phononenfrequenzen für Festkörper mit Defekten selten explizit berechnet; in unsere Studie zeigen wir jedoch, dass deren Beitrag die Freie Bildungsenergie von Defekten bei hohen Temperaturen wesentlich beeinflussen kann. Dies trifft insbesondere auf $v_O^{\bullet\bullet}$ zu: es zeigt sich, dass Phononenbeiträge für den Anstieg der freien Bildungsenergie von Defekten um fast 1 eV bei 1000 K verantwortlich sind und den zweifach geladenen Defekttyp dadurch energetisch weniger günstig als andere Ladungszustände unter hohen Temperaturen werden lassen.

In unserer Studie zeigen wir, dass Gittervibrationen die relative Stabilität von defektfreien ABO_3-Perowskitoberflächen bei hohen Temperaturen beeinflussen. Dies geschieht durch die Verwendung eines einfachen thermodynamischen Modells, welches Vorhersagen über die relative Stabilität der beiden möglichen Grenzschichten einer $BaZrO_3$ (001) Oberflächen - BaO- und ZrO_2-Terminierung - erlaubt. Es zeigt sich, dass die BaO-Terminierung bei und unterhalb von Raumtemperatur die thermodynamisch stabilere ist. Unter erhöhten Temperaturen (um ca. 500 K) sagt das

Modell eine Koexistenz beider Terminierungen, BaO- und ZrO_2, voraus, und bei hohen Temperaturen (ab ca. 900 K) wird die ZrO_2 Grenzschicht sogar die stabilere von beiden.

In einem weiteren Teil der Arbeit betrachten wir die beiden Sauerstoffleerstellen, $v_O^{\times}$ und $v_O^{\bullet\bullet}$ auf der (001) Oberfläche von $BaZrO_3$ und berechnen deren Freie Segregationsenergien, welche Auskunft über die Tendenz des Defekts gibt, sich aus dem Volumenmaterial an die Oberfläche hin zu verschieben. Auch hier findet sich ein wichtiger Beitrag in den Gittervibrationen, welche eine positive Segregationsentropie erzeugen, die wiederum den $v_O^{\bullet\bullet}$ Defekt an der Oberfläche gegenüber dessen Auftreten im Volumenmaterial stabilisieren.

Im letzten Teil der Studie untersuchen wir Sauerstoffleerstellen in extrem dünnen Perowskitfilmen mit Dicken von ca. 0.4 - 1.3 nm (entsprechen drei bis sieben Atomschichten) und betrachten dabei Confinementeffekte auf die Defekteigenschaften. Es zeigt sich, dass sich die Eigenschaften der Defekte in den dünnen Filmen (außer in den dünnsten) nicht merklich von den Eigenschaften im Volumenmaterial unterscheiden, was darauf hindeutet, dass deren Eigenschaften nur von der unmittelbaren Umgebung der Defekte beeinflusst werden.

Zusammenfassend lässt sich sagen, dass die Ergebnisse, die in der vorliegenden Arbeit präsentiert werden, die bedeutende Rolle, welche Gittervibrationen zur korrekten thermodynamischen Beschreibung von Punktdefekten in Perowskiten und an deren Oberflächen bei erhöhten Temperaturen spielen, deutlich machen. Es wird gezeigt, wie wichtig die Berücksichtigung der Gittervibrationsbeiträge besonders für die Berechnung von Freien Bildungs- und Segregationsenergien geladener Sauerstoffleerstellen und für die Bestimmung der relativen thermodynamischen Stabilitäten unterschiedlicher Oberflächengrenzschichten ist.

Contents

I. Introduction and Theoretical Background **1**

1. Introduction and Motivations **2**

2. Theoretical Background: First-principles Simulations in the Solid State **11**

2.1. The Many-body Problem 11

2.1.1. The Born-Oppenheimer Approximation 12

2.1.2. The Hartree-Fock Approximation 14

2.1.3. The Density Functional Theory 17

2.2. The Linear Combination of Atomic Orbitals in Periodic Systems . . 28

2.3. The Calculation of Vibrational Frequencies in Solids and the Frozen-Phonon method 32

2.3.1. Classical Determination of the Normal Modes of Vibration and their Characteristic Frequencies 32

2.3.2. First-principles Determination of the Hessian Matrix: the Frozen-Phonon Method 35

3. Extension of the First-principles Formalism **37**

3.1. *Ab Initio* Thermodynamics 37

3.1.1. ABO_3 Perovskite Surface Stability 42

3.2. The Supercell Approach and Calculations of Defective Systems . . . 48

3.2.1. The Supercell Approach 50

3.2.2. First-principle Calculation of the Defect Formation Energy . 53

II. Results **61**

4. Pristine bulk $BaZrO_3$ **62**

4.1. Atomic Structure 62

4.2. Electronic Structure 64

4.3. Vibrational Properties 68

5. Oxygen vacancies in bulk $BaZrO_3$ **74**
5.1. Electronic Structure 75
5.2. Atomic Structure 79
5.3. Vibrational Properties 82
5.4. Defect Formation Energy 87

6. Two Dimensional Defects in ABO_3 Perovskites: The $BaZrO_3$ (001) Surface **92**
6.1. The Clean (001) Surface 93
6.2. Surface Energy and Thermal Stability of its Terminations 97
6.3. Oxygen Vacancies on the (001) Surface 102

7. Ultra-thin Films and Oxygen Vacancies Therein **107**
7.1. Defective-free $BaZrO_3$ Ultra-thin Films 107
7.2. Oxygen Vacancies in $BaZrO_3$ Ultra-thin Films 114

8. Conclusions **120**

Appendices **126**

A. Computational Details **127**

B. Choice of the Monkhorst-Pack mesh **131**

C. Determination of the Valence Band Maximum in Charged Supercells **133**

List of Figures

1.1. The ideal ABO_3 perovskite structure. 2
1.2. Solid fuel cells employing oxygen or proton conducting electrolytes . 8

3.1. The cleavage of an ABO_3 perovskite. 44
3.2. Supercell expansion of the primitive unit cell of an ideal ABO_3 perovskite. 51

4.1. The cubic cell of $BaZrO_3$. 63
4.2. Electronic charge density map plots for pristine $BaZrO_3$. 65
4.3. Band structure and electronic density of states of pristine $BaZrO_3$. . 67
4.4. First Brillouin Zone of the $Pm\bar{3}m$ space group. 68
4.5. Phonon dispersion relations for $BaZrO_3$. 70
4.6. Vibrational contributions to the free energy of $BaZrO_3$ considering only phonons at Γ-point of the first Brillouin Zone. 72
4.7. Molar constant volume heat capacity calculated including more than one phonon wave vector. 73

5.1. Electronic density of states of bulk $BaZrO_3$ with oxygen vacancies. . 76
5.2. Electronic density projected on the defective level induced by the introduction of $v_O^{\times}$ in bulk $BaZrO_3$. 77
5.3. Electronic density redistribution in bulk $BaZrO_3$ with oxygen vacancies. 78
5.4. Atomic structure of bulk $BaZrO_3$ containing an oxygen vacancy. . . 81
5.5. Vibrational density of states calculated when an oxygen vacancy is introduced in bulk $BaZrO_3$. 83
5.6. Vibrational entropy, S^{vib} as a function of the vibrational frequency of a single mode, ω, at different temperatures T. 84
5.7. Lattice vibrations contribution to the defect formation energy. 86
5.8. Oxygen vacancies Gibbs free energy of formation as a function of the Fermi level. 90

6.1. Slab models for the $BaZrO_3$ (001) surface. 93
6.2. Electronic density redistribution on the $BaZrO_3$ (001) surface. . . . 95
6.3. Electronic DOS for the $BaZrO_3$ (001) surface. 96
6.4. Thermal contributions to the Gibbs free energy of $BaZrO_3$ and O. . 99
6.5. Stability diagrams for the $BaZrO_3$ (001) surface at different temperatures. 101
6.6. Oxygen vacancies on the $BaZrO_3$ (001) surface. 102
6.7. DOS for oxygen vacancies on the $BaZrO_3$ (001) surface. 104
6.8. Vibrational contributions to the segregation free energy of $v_O^{\bullet\bullet}$. . . . 105

7.1. Slab models for $BaZrO_3$ ultra-thin films. 108
7.2. Electronic DOS for the $BaZrO_3$ ultra-thin films. 110
7.2. (Continued) Electronic DOS for the $BaZrO_3$ ultra-thin films. 111
7.3. Electronic density redistribution in $BaZrO_3$ ultra-thin films. 112
7.4. VDOS of $BaZrO_3$ ultra-thin films. 113
7.5. VDOS for oxygen vacancies in $BaZrO_3$ ultra-thin films. 117
7.6. Phonons contribution to the oxygen vacancy formation free energy for $BaZrO_3$ ultra-thin films. 118
7.7. Formation energy of $v_O^{\times}$ in $BaZrO_3$ ultra-thin films. 119

B.1. Convergence of the system electronic energy with respect to the Monkhorst-Pack mesh size. 132

C.1. Extrapolation of the electron chemical potential value. 134

List of Tables

2.1. Atomic units 13

4.1. Crystallographic information on the structure of $BaZrO_3$. 63
4.2. Ground-state properties of $BaZrO_3$, comparison with the literature. 64
4.3. Vibrational frequencies of $BaZrO_3$ at the Γ-point of the first Brillouin Zone. 69

5.1. Electronic properties of the defective level induced by oxygen vacancies in bulk $BaZrO_3$. 77
5.2. Structural relaxations induced by oxygen vacancies in bulk $BaZrO_3$. 79
5.3. Ground-state properties of the O_2 molecule. 87
5.4. Correction energy due to finite-size effects for charged defects in bulk $BaZrO_3$. 88
5.5. Oxygen vacancies formation Gibbs free energy and charge transition levels in bulk $BaZrO_3$ at selected temperatures. 91

6.1. Relaxation parameter for the $BaZrO_3$ (001) surface. 94
6.2. Cleavage, relaxation and surface energies for the $BaZrO_3$ (001) surface. 97
6.3. Formation energy of selected oxides calculated at different temperature. 98
6.4. Structural relaxations induced by oxygen vacancies on the (001) surface of $BaZrO_3$. 103

7.1. Relaxation parameter for $BaZrO_3$ ultra-thin films. 109
7.2. Relaxation parameter for oxygen vacancies in $BaZrO_3$ ultra-thin films. 115
7.3. Electronic properties of the defective level induced by oxygen vacancies in $BaZrO_3$ ultra-thin films. 116

Part I.

Introduction and Theoretical Background

1. Introduction and Motivations

Perovskite oxides are a wide class of materials with considerable technological importance. The ideal perovskite oxide structure is cubic and can be represented by the formula ABO_3, where A and B are cations, respectively 12-fold and 6-fold coordinated with oxygen anions. The B cation lies in the center of a regular octahedron which corners are made of oxygen anions. Corner-sharing $[BO_6]$ octahedra form a three-dimensional regular net in which each A cation lies in a cavity formed by four of such polyhedra, as illustrated in Figure 1.1.

The ideal perovskite structure can undergo a broad range of structural distortions, and an extremely extensive variety of cations can occupy the A and B sites. The stability of the (ideal) cubic perovskite structure with respect to other structures can be defined in terms of the ionic radii of the constituent ions through the Goldschmidt tolerance factor t:

$$t = \frac{r_A + r_O}{\sqrt{2}(r_B + r_O)}, \tag{1.1}$$

where r_A, r_B and r_O are the the ionic radii of the A-site cation, B-site cation and oxygen anion, respectively. The ideal cubic structure is obtained when $t = 1$; the more t deviates from unity, the more the cubic structure becomes distorted with the lattice becoming first rhombohedral and then orthorhombic [1]. Stable perovskite structures are predicted in the range of $0.77 \leq t \leq 1.00$ [2]; while for

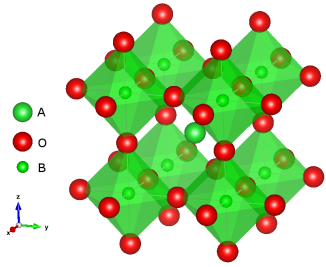

Figure 1.1.: The ideal ABO_3 perovskite structure. The $[BO_6]$ octahedra are highlighted.

$t > 1$ only the hexagonal structure is stable [2]. The perovskite structure is also highly stable with respect to the introduction of vacancies and cation substitutions, and many classes of materials with different compositions stem from this simple structure. For example, the family of tungsten bronzes, based on the $NaWO_3$ compound, can be seen as strongly A-deficient ABO_3 perovskites; while the family of $SrFrO_x$ compounds is an example of oxygen-deficient perovskites. Furthermore, dopant cations can substitute some of the ions occupying the A- and/or B-sites, originating a variety of structures with different compositions and properties. An example is the structures of the high temperature superconductors $YBa_2Cu_3O_{7-x}$ or that of the relaxor ferroelectrics $Pb(Zr, Ti)O_3$; in both cases, cations of different valence randomly occupy part of both the A- and B-sites of the perovskite structure. Such a variety of structures and chemical compositions endow perovskite oxides and perovskite-like oxides with an enormous variety of electronic, dielectric, ferroic and magnetic properties [3]. In addition, the ability to tailor such properties modifying the material chemical composition make perovskite oxides and related material of utmost importance in several technological fields such as optics, electrochemistry, catalysis, superconductivity and thin film growth [3, 4, 5, 6, 7].

As in all solids, point defects can affect the properties of ABO_3 perovskites in a significant way. In particular, oxygen vacancies are probably the most common point defect in these systems and their presence is relevant for many applications [8]. For example, ferroelectric perovskites are being used as memory elements in microcircuits and oxygen vacancies are known to be related to polarization degradation phenomena, as fatigue and aging [9, 10, 11]. Furthermore, the concentration of oxygen vacancies, easily modified by tuning the atmosphere oxygen partial pressure, highly influences the type of conductivity of ABO_3 perovkistes, as in the case of $SrTiO_3$-$BaTiO_3$ solid solutions, where, as the concentration of oxygen vacancies decreases, the material conductivity switches from n-type to p-type [12]; or as in the case of the mixed conducting $Sr(Fe_xTi_{1-x})O_{3-\delta}$ perovskite, where, according to the concentration of oxygen vacancies, the conductivity changes from electronic to ionic [13]. In addition, the content of oxygen vacancies can affect the magnetic properties of materials, such as the magnetoresistance in $SrFeO_{3-x}$ perovskites [14]; and can also influence the critical temperature for the conductor to superconductor phase transition in the $YBa_2Cu_3O_{7-x}$ perovskite-like oxide [15]. Finally, oxygen vacancies are the most relevant charge carriers in several ion-conducting perovskite oxides and their presence is fundamental for the function and performance of many electrochemical devices, first of all, solid oxide fuel cells (see e.g. Refs. [4, 16] and references therein).

Nowadays, first principles calculations are routinely applied to the study of ox-

ides, and they have proved to be a very useful complement to experimental measurements, due to their ability to give a deep insight on the material atomic structure. In particular, due to the decisive role of point defects in determining the properties of materials, first principles calculations of such defects became with time more and more popular, and are nowadays able to estimate many quantities which can be compared directly with experiments, such as defect concentrations, NMR chemical shifts, local atomic structure and vibrational frequencies [17]. Most of first principles studies rely on the density functional theory (DFT), in which the time-independed, non-relativistic, many-body problem is translated in a one-particle problem with an effective potential which is usually obtained approximately (e.g. by the local density approximation [18] or the generalized-gradient approximation [19]. A more detailed introduction to DFT is reported in Section 2). Standard DFT approximations are inadequate to describe systems containing rare-earth or transition metal atoms with localized d and/or f electrons, due to the "averaged" way in which the Coulombic potential is represented; therefore, first-principles studies of ABO_3 perovskites often employ the DFT+U method, in which the strong Coulombic repulsion between localized electrons is taken into account introducing an additional term (the Hubbard-like U parameter) to the system hamiltonian [20]. However, there is no unique choice for the U parameter and the predicted properties can show a very strong dependence on the U-value; furthermore, this term is selectively applied to the orbitals of the localized electrons only, and as a consequence, parts of the same system result treated with different frameworks. An alternative to the DFT+U method is given by the hybrid functionals, which have proved to describe very accurately the structural, electronic, magnetic and energetics properties of ABO_3 perovskites [21] and oxygen vacancies therein [22, 23].

A key quantity in the characterization of point defects is the defect Gibbs energy of formation, which value can be readily obtained from first-principles calculations. In the case of low defect concentrations (dilute limit) the significance of the defect Gibbs energy of formation is particularly meaningful for defect chemistry, due to its simple relation with the point defect electrochemical potential, $\tilde{\mu}_\mathrm{d}$ [24]:

$$\tilde{\mu}_\mathrm{d} = \mu^0_\mathrm{d} + \mathrm{k_B T} \ln \mathrm{x_d} + z_\mathrm{d} e\phi \tag{1.2}$$

where, $\mathrm{x_d} = \frac{N_d}{N}$ is defect molar fraction, i.e. the ratio between the number of point defects and the number of the possible equivalent sites in which the defect can occur; k_B is the Boltzmann constant, z is the defect charge, e is the electron charge and ϕ is the local electrostatic potential. The *standard state chemical potential* of the defect, μ^0_d, corresponds thus to the Gibbs energy of formation of a single defect:

$\Delta_f g_d$. For point defects, this quantity cannot be easily measured and, therefore, first-principles calculations offer an invaluable tool in complementing experiments. As the study of ionic transport at the nanoscale (nanoionics) is gaining momentum for applications in the field of energy conversion and storage (e.g. nanostructured electrodes and electrolytes in solid oxide fuel cells (SOFCs) and batteries) [25, 26], the investigation of point defects in confined systems and, the dependence of the standard state chemical potential on the system size in particular, acquires special importance.

Even though, in its original formulation, DFT is principally limited to a system ground-state, a connection with classical and statistical thermodynamics is possible. Such a connection assumes particular importance since many technological applications of ABO_3 perovskites involve temperatures considerably above room one. A straightforward and successful way to extend DFT to finite temperatures in given by the so-called method of *ab initio* atomistic thermodynamics [27], outlined in Section 3.1. This approach consists in combining the system total energy, provided by the DFT calculations, with statistical thermodynamics arguments, in order to calculate the thermodynamic potentials of interest for the studied system. As vibrational degrees of freedom are usually the most relevant contribution to the partition function of most ABO_3 perovskites, and of solids in general, the calculation of lattice vibrations becomes a fundamental point in determining the temperature dependence of thermodynamic quantities; above all the Gibbs energy, which characterizes the equilibrium state of a system under the common experimental conditions of constant temperature and pressure. The harmonic approximation is usually adequate to reproduce the vibrational spectrum of many materials in non-pathological conditions (e.g. near the melting point) but calculation of lattice vibrations is inherently a very time-consuming task and, therefore, is rarely performed on large systems. This is specially true when hybrid functionals are employed and/or the system has a very low symmetry due to the presence of point defects.

Notwithstanding the fact that the ideal cubic perovskite structure can be regarded as a starting template for a very large class of materials, the majority of ABO_3 perovskites are cubic only at high temperatures (room temperature and above) and undergo structural phase transitions at low temperatures. A well studied example of such structural changes is the cubic-to-tetragonal phase transition in $SrTiO_3$ which occurs at around 105 K. This is a typical example of an antiferrodistortive (AFD) phase transition mediated by the condensation of a phonon mode [28]. Both first- and second-order phase transitions can be triggered by a soft mode; i.e. a phonon mode which frequency decreases lowering the temperature and vanishes (or almost) as the temperature reach the phase transition critical temperature T_c.

In particular, as the temperature reaches T_c, the atomic displacements related to the soft mode (i.e. the ionic motions described by the soft mode eigenvector) begin to "freeze", imposing a structural distortion that lead to the phase transition (see for example Refs. [29, 30]). The AFD phase transition in $SrTiO_3$ occurs due to the condensation of a soft mode at the R-point of the first Brillouin Zone, which leads to a rotation of the $[ZrO_6]$ octahedra and a lowering of the crystal symmetry to tetragonal [28, 31]. Calculations of lattice vibrations for the high-temperature perovskite cubic structure often show unphysical imaginary phonon frequencies, which reflect the fact that the ground state structure of that particular material is really not cubic at 0 K. This has been shown in detail in first principles calculations of $SrTiO_3$ [32, 33, 34]. The low-temperature structure of many ABO_3 perovskites can contain a much larger number of atoms than the ideal cubic structure and therefore its modeling can require considerably larger computational resources, especially when the model includes the presence of point defects, which additionally lowers the system symmetry. On the other hand, at the working temperature range of many technological applications, these perovskites are already in the cubic phase. A cubic symmetry is desirable since requires the least computational resources; but, due to the zero-temperature formalism of DFT, first-principles calculations cannot predict the vibrational frequencies of perovskites which do not possess a cubic ground-state structure. Therefore, the wish, on the one hand, to model materials at realistic working conditions, and, on the other hand, to keep the computational model as simple as possible, leads to the necessity to find a perovskite material which maintains the cubic structure not only at high, but also at low temperatures. One of a few such perovskites is $BaZrO_3$.

$BaZrO_3$ (BZO) is a ceramic oxide with the ideal cubic perovskite structure, which is remarkably preserved down to 2 K [35]. In addition, BZO possesses several important properties, as high melting point, small thermal expansion coefficient, low thermal conductivity and low dielectric loss (see e.g. Refs. [36] and [37]) which make it suitable for different technological applications, such as wireless communications [38], production of substrates for deposition of superconducting thin films [39] and production of hybrid perovskite-polymer magnetic nanocomposites [40].

Since the last decade, BZO has been receiving a great deal of attention as a very promising high-temperature proton conductor (HTPC) electrolyte. These are solid materials able to efficiently conduct protons at temperatures between 400 and 700 °C; much higher than the 100 °C at which polymer proton conductors usually work. Remarkably, Y-doped BZO shows both an excellent protonic conductivity ($> 10^{-2}$ S cm^{-1} at around 700 °C) [41, 42] and a very high chemical stability at high temperatures [43, 44], which make the material a perfect HTPC candidate for

ceramic fuel cells. Ceramic fuel cells based on proton conducting electrolytes are becoming more and more important and they are nowadays generally referred to as protonic ceramic fuel cells (PCFCs).

Ceramic fuel cells are electrochemical devices that convert chemical energy into electricity with a much higher efficiency than conventional systems based on combustion (around 50-70% and up to 90%, including heat recovery, for fuel cells compared to an average of 20-30% for combustion engines) [45]. In the most basic set up, a fuel cell consists of two electrodes (anode and cathode) separated by an electrolyte (in ceramic fuel cells all the components are solid), hydrogen is the most employed fuel and oxygen is the oxidant gas. The fuel is fed to the anode and the oxygen to the cathode and the two electrodes are connected by an electric circuit. The reaction between hydrogen and oxygen gives as the only exhaust gas water, making fuel cells ideal devices for the environmental-friendly energy policies required in modern societies. Fuel cells benefit of additional features; such as the ability to produce power constantly, as long as the fuel and oxidant are provided, and a high versatility in the fuel choice, since hydrogen can be extracted from many natural gases. The electrolyte plays a crucial role in the fuel cell performance and should possess a high ionic conductivity and negligible electronic conductivity.

According to the nature of the mobile species in the electrolyte, ceramic fuel cells can be divided in different technological classes. Fuel cells based on oxygen conductors (SOFCs) are perhaps the most well established thereof. As the name suggests, in these devices, the solid electrolyte is an oxygen anion conductor; the most popular of which is probably yttria-stabilized zirconia. The oxygen is reduced at the cathode triple phase boundary: the zone where the electrolyte, cathode and gas come into contact. After this electrochemical reaction, the newly created O^{2-} species migrate through the porous cathode toward the electrolyte by means of which they reach the anode and can react with the fuel [4, 46], as illustrated in Figure 1.2. SOFCs operate usually in the temperature range of 900-1000 °C to ensure an adequate ionic conductivity. If on the one hand, the high temperatures can also allow the internal reforming of hydrocarbon fuels [47], on the other hand, they result detrimental for the device lifetime; hastening the components degradation and increasing the operational costs, due to the need of specific and expensive interconnecting materials [48].

PCFCs make a promising class of ceramic fuel cell which employs HTPC electrolytes and can work at much lower temperatures than SOFCs, since the proton migration mechanisms require much lower activation energies than those necessary for the transport of the much larger oxygen anions (activation energies around 0.3-0.6 eV for proton diffusion [50, 43], compared to around 1 eV found for oxygen

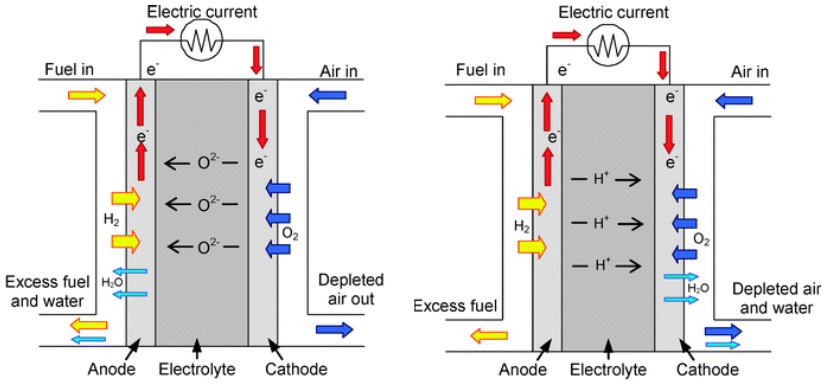

(a) SOFC (b) PCFC

Figure 1.2.: Schematic representation of processes involved in solid oxide fuel cells (a) and protonic ceramic fuel cells (b). Picture adapted from reference [49] with permission from the Royal Society of Chemistry.

anions in yttria-stabilized zirconia [51]). The electrochemical processes occurring in PCFC are similar to those described for SOFCs; as shown in Figure 1.2, the main difference is that, this time, the mobile species are protons, which migrate from the anode, through the electrolyte, to the cathode, where they react with the oxygen atoms.

Several ABO_3 perovskites show protonic conductivity after being doped with trivalent acceptors, such as Y, Gd, Nd, Eu, *etc.* The dopant, M, usually substitutes a B cation, generating charge compensating oxygen vacancies. In Kröger-Vink notation [52] this process can be described by the following equation [53, 49]:

$$2B_B^{\times} + O_O^{\times} + M_2O_3 \rightleftharpoons 2M_B' + v_O^{\bullet\bullet} + 2BO_2 \tag{1.3}$$

Doping with too large cations can lead to a substitution of the dopant M with the A cations, decreasing the concentration of oxygen vacancies $v_O^{\bullet\bullet}$ from the ideal value: $[v_O^{\bullet\bullet}] = \frac{[M_B']}{2}$ [54]. The presence of oxygen vacancies is crucial in the mechanism involving the incorporation and formation of mobile protons inside the electrolyte [55], since the most important process, which allows the creation of protonic defects in these materials, is the dissociative adsorption of water [56, 54, 42]. This reaction involves the adsorption of water molecules, present as vapour in the atmosphere, into oxygen vacancies, with their subsequent dissociation into a proton and an

hydroxide anion:

$$H_2O + v_O^{\bullet\bullet} + O_O^{\times} \rightleftharpoons 2(OH)_O^{\bullet} \tag{1.4}$$

The detailed study of the formation of oxygen vacancies represents therefore a necessary step in the characterization of this process.

As already mentioned above, Y-doped BZO possess both an excellent protonic conductivity and chemical stability to all the fuel cell components in the intermediate temperature range of 400 and 700 °C; unfortunately, its implementation in actual devices has been hindered so far, due to two principal factors: firstly, the conductivity in the grain boundary region is much lower than in the bulk and, secondly, the material has a very poor sinterability which leads to sintered pellets with a large grain- boundary-volume-to-total-material-volume ratio. Different methods have been applied recently to solve this problem. There are two main strategies: either to improve the grain boundary conductivity, or increase the grain size, minimizing thus the grain boundary contribution to the total ionic conductivity. The latter approach has proved to be more successful; in particular, epitaxially grown thin films, deposited through pulsed laser deposition techniques, have shown the most promising results, with a high crystalline quality, and the consequent reduction of grain boundary effects. These systems possess an ionic conductivity just slightly lower than that observed in the bulk [57].

The aim of this study is to investigate the properties of oxygen vacancies in ABO_3 perovskites; considering the bulk material, surfaces and ultra-thin films, which can be used as a model of a solid electrolyte. The results can be compared in order to analyze possible spatial confinement effects on the defect properties. Throughout the study, $BaZrO_3$ is considered as a model material and particular emphasis in given to the contribution of lattice vibrations to the defect formation energy at high operational temperatures. The Thesis is organized as follows:

- Chapter 2 and Chapter 3 introduce the theoretical framework on which this study is based. From Section 2.1 to Section 2.2 , the basics of density functional theory and its implementation in the linear combination of atomic orbitals method are outlined. Section 2.3 summarizes the ideas behind the frozen-phonon method, employed in this study to calculate lattice vibrations in the harmonic approximation. Section 3.1 introduces the *ab initio* atomistic thermodynamics formalism, with applications to the study of ABO_3 perovskite surfaces stability reported in Section 3.1.1. Section 3.2 outlines the concepts behind the first-principles determination of the defect formation energy and illustrates the strategies employed for its determination.

- Chapter 4 demonstrates the ability of our theoretical method to reproduce

the main properties of pristine bulk $BaZrO_3$. The results are compared with experiments and other computational studies and show that our computational scheme can describe the system ground-state properties with extreme accuracy.

- Chapter 5 reports the results obtained for bulk $BaZrO_3$ containing neutral or charged oxygen vacancies. The electronic (Section 5.1), atomic (Section 5.2) and vibrational (Section 5.3) properties of the system are considered and the defect formation energy is calculated over a range of temperatures (Section 5.4).

- In Chapter 6 we consider the (001) surface of $BaZrO_3$. Firstly, we study, in Section 6.1, the electronic, atomic and vibrational properties of the clean surface. Then, we apply the methods outlined in Sections 3.1 and 3.1.1 to calculate the relative stability between the two possible surface terminations as a function of the temperature (Section 6.2). Finally, in Section 6.3, we consider oxygen vacancies on the surface and we calculate their segregation energy, with particular focus on the vibrational contribution to the segregation enthalpy and entropy.

- In Chapter 7 we study $BaZrO_3$ ultra-thin films and oxygen vacancies therein. Firstly, the electronic, atomic and vibrational properties of defective-free ultra-thin films are studied as a function of the film thickness (Section 7.1). Afterwards, we introduce oxygen vacancies in the system and we study how the defect properties are affected by the film thickness; with particular focus on how the vibrational contribution to the defect formation energy is affected (Section 7.2).

- The last Chapter, Chapter 8, summarizes the results and draws the conclusions of this work.

2. Theoretical Background: First-principles Simulations in the Solid State

Quantum mechanical simulations of solids are nowadays extremely popular and offer an essential contribution to the study of advanced materials. Since the first appearance in the 1970s, quantum mechanical *ab initio* simulations have been rapidly gaining greater importance due to the increase in computer performances, the availability of well implemented computer programs and the improvement of their capabilities. From the late 1970s to the present time, the most widespread *ab initio* method in the calculations of the electronic structure of periodic systems combines the use of a plane wave (PW) basis set and the local density approximation (LDA) [18] in the density functional theory (DFT). Due to their analytical simplicity, PWs are very desirable functions for computer calculations and are well suited for describing systems with delocalized electrons, such as metals. On the other hand, their employment for the study of covalent systems suffers the loss in chemical insight typical of localized atomic basis sets, which are commonly used in molecular quantum chemistry since the 1960s. The development of *ab initio* methods based on local basis sets occurred simultaneously with that of PW-based methods. CRYSTAL [58] has been one of the first periodic *ab initio* computer codes using this approach and was the first to be widely distributed internationally outside its own research group, starting from 1989. Today, it offers powerful tools for calculating a wide range of properties of periodic systems with different chemical compositions and dimensionality (0D, 1D, 2D and 3D systems).

The following sections gives a brief introduction on the basics of quantum chemistry applied to periodic systems. Only the topics relevant to this Thesis are summarized and some attention is given to explain the approach employed by the CRYSTAL code.

2.1. The Many-body Problem

Quantum chemistry focuses its attention on the study of atoms, molecules and condensed systems. Its main task consists in solving the time-independent non-

relativistic Schrödinger equation:

$$\hat{H}\Psi = E\Psi, \tag{2.1}$$

i.e. in finding the eigenstates, Ψ, of the Hamiltonian operator $\hat{H}$. These represent *stationary states* and can be trivially used to solve the time-dependent Schrödinger equation. The Hamiltonian operator $\hat{H}$ is obtained from the system classical Hamiltonian $H(\{\mathbf{x}_j\},\{\mathbf{p}_j\})$ with the canonical substitution:

$$\begin{aligned} \mathbf{x}_j &\rightarrow \mathbf{X}_j, \\ \mathbf{p}_j &\rightarrow \mathbf{P}_j = -i\hbar\nabla_j, \end{aligned} \tag{2.2}$$

where the position operator $\mathbf{X}_j$ simply multiplies by the position of the j-th particle, and the momentum operator $\mathbf{P}_j$ differentiates with respect to the coordinates of the j-th particle.

The main forces acting between electrons and nuclei are electrostatic and these are usually the only interactions explicitly considered in quantum chemistry. In this respect, considering a system composed of M nuclei and and N electrons, the Hamiltonian operator in equation (2.1) takes the form:

$$\begin{aligned} \hat{H} = &-\sum_{j=1}^{N}\frac{1}{2}\nabla_j^2 - \sum_{A=1}^{M}\frac{1}{2M_A}\nabla_A^2 - \sum_{j=1}^{N}\sum_{A=1}^{M}\frac{Z_A}{|\mathbf{r}_j-\mathbf{R}_A|} + \\ &\sum_{j=1}^{N}\sum_{k>i}^{N}\frac{1}{|\mathbf{r}_j-\mathbf{r}_k|} + \sum_{A=1}^{M}\sum_{B>A}^{M}\frac{Z_A Z_B}{|\mathbf{R}_A-\mathbf{R}_B|}, \end{aligned} \tag{2.3}$$

where $\mathbf{r}$ and $\mathbf{R}$ represent, respectively, the electrons and nuclei positions, which are the independent variables of the many-body wavefunction $\Psi = \Psi(\{\mathbf{r}_j\},\{\mathbf{R}_A\})$. M_A is the mass of the A-th nucleus and Z_A is its atomic number. Equation (2.3) is written in *atomic units*, which relationship with common SI units is reported in Table 2.1. The terms composing the Hamiltonian operator of equation (2.3) are, from left to right: the electronic kinetic energy, the nuclear kinetic energy, the electrostatic attraction between nuclei and electrons, the electrostatic repulsion between electrons and the electrostatic force between nuclei.

2.1.1. The Born-Oppenheimer Approximation

A very useful approximation, with a central role in quantum chemistry, is the *Born-Oppenheimer*. It allows one to simplify the many-body problem (equations (2.1)

Dimension	Name	Symbol	Value in SI units
Length	Bohr	a_0	$5.291\,77 \times 10^{-11}$ m
Mass	Electron rest mass	m_e	$9.109\,38 \times 10^{-31}$ kg
Angular momentum	Reduced Planck's constant	$\hbar$	$1.051\,57 \times 10^{-34}$ J s
Charge	Elementary charge	e	$1.602\,18 \times 10^{-19}$ C
Energy	Hartree	E_h	$4.359\,74 \times 10^{-18}$ J

Table 2.1.: Relationship between atomic units and the SI units.

and (2.3)), decoupling the motion of electrons from that of nuclei. Very informally, due to their much smaller mass with respect to nuclei, we can just consider the motion of electrons, while the nuclei are held in a fixed configuration described by their coordinates $\{\mathbf{R}_A\}$. This allows one to split the many-body equation (2.1) into two parts (details can be found for example in ref. [59]):

$$\hat{H}_{elec}\Phi_{elec}(\{\mathbf{r}_j\};\{\mathbf{R}_A\}) = E_{elec}(\{\mathbf{R}_A\})\Phi_{elec}(\{\mathbf{r}_j\};\{\mathbf{R}_A\}), \tag{2.4a}$$

$$\hat{H}_{nucl}\Phi_{nucl}(\{\mathbf{R}_A\}) = E_{nucl}\Phi_{nucl}(\{\mathbf{R}_A\}), \tag{2.4b}$$

where $\hat{H}_{elec}$ is the Hamiltonian describing the interaction of N electrons with M point charges representing the nuclei and $\hat{H}_{elec}$ is the Hamiltonian for the M nuclei in the average field generated by the electrons. This average field is represented by the *potential energy surface*, $E_{PES}(\{\mathbf{R}_A\}) = E_{elec}(\{\mathbf{R}_A\}) + \sum_{A=1}^{M}\sum_{B>A}^{M}\frac{Z_A Z_B}{|\mathbf{R}_A - \mathbf{R}_B|}$, which is obtained from solving equation (2.4a) and is a function of the position of the nuclei $\{\mathbf{R}_A\}$. In conclusion, the Hamiltonians of equations (2.4a) and (2.4b) usually takes the form:

$$\hat{H}_{elec} = -\sum_{j=1}^{N}\frac{1}{2}\nabla_j^2 - \sum_{j=1}^{N}\sum_{A=1}^{M}\frac{Z_A}{|\mathbf{r}_j - \mathbf{R}_A|} + \sum_{j=1}^{N}\sum_{k>i}^{N}\frac{1}{|\mathbf{r}_j - \mathbf{r}_k|}, \tag{2.5a}$$

$$\hat{H}_{nucl} = -\sum_{A=1}^{M}\frac{1}{2M_A}\nabla_A^2 + E_{PES}(\{\mathbf{R}_A\}). \tag{2.5b}$$

Quantum chemistry methods for solids are usually developed to solve the electronic many-body problem, equation (2.4a), which determines the electronic structure of the system and thus most of its chemical properties. On the other hand, for molecular systems, equation (2.4b) is usually also solved, obtaining, in addition to

the electronic energy, the vibrational, rotational and translational contributions to the total energy of the system.

2.1.2. The Hartree-Fock Approximation

The Hartree-Fock (HF) approximation played a central role in quantum chemistry for a long time. Nowadays, it is not so popular anymore; nevertheless, it is worth illustrating its basic principles and introducing some terminology and concepts which are also part of the Density Functional Theory (subsection 2.1.3), especially in the framework of hybrid functionals. Furthermore, the HF approximation offers the starting point for developing more accurate theories such as the Configuration Interaction, Coupled Cluster and perturbation theory methods [60, 61].

It is not possible to analytically solve the many-electron problem, i.e. finding the eigenfunctions of the electronic Hamiltonian in equation (2.5a), and many approximation can be made. As a starting point, one can expect that, since the eigenfunctions $\Phi_{elec}(\{\mathbf{r}_j\};\{\mathbf{R}_A\})$ of equation (2.5a) belong to some function space, it can be found a basis of orthonormal functions which allows one to express any function as a proper linear combination of them. Such 'many-particle' basis functions may, in turn, be expressed employing 'single-particle' functions. We will generally call *spin orbitals* any set of orthonormal single-particle functions:

$$\chi(\mathbf{x}) = \phi(\mathbf{r})\gamma(\omega). \tag{2.6}$$

A general spin orbital, χ, is a function of both the spatial variables $\mathbf{r}$ and the spin variable ω and can be expressed as a product of a *spatial orbital*, $\phi(\mathbf{r})$, and a spin function, $\gamma(\omega)$. In quantum chemistry, the spin is usually introduced only formally since relativistic effects are normally not included in the Hamiltonian. Thus the two possible orientations of the electron spin are simply considered introducing two arbitrary orthonormal functions: $\alpha(\omega)$ and $\beta(\omega)$. The use of spin orbitals allows one to take into account from the beginning the Pauli exclusion principle and to form correct antisymmetric wave functions. For a system containing N electrons, described by spatial and spin coordinates $\{\mathbf{x}_1, \mathbf{x}_2, \cdots, \mathbf{x}_N\} = \{\mathbf{x}_j\}$, one can build an N-electron antisymmetric wave function, $\Phi_{S,elec}(\{\mathbf{x}_j\})$, as the *Slater determinant* of N spin orbitals $\{\chi_i, \chi_j, \cdots, \chi_k\}$, taken from a wider set of K spin orbitals:

$$\Phi_{S,elec}(\{\mathbf{x}_j\}) = (N!)^{-\frac{1}{2}} \begin{vmatrix} \chi_i(\mathbf{x}_1) & \chi_j(\mathbf{x}_1) & \cdots & \chi_k(\mathbf{x}_1) \\ \chi_i(\mathbf{x}_2) & \chi_j(\mathbf{x}_2) & \cdots & \chi_k(\mathbf{x}_2) \\ \vdots & \vdots & \ddots & \vdots \\ \chi_i(\mathbf{x}_N) & \chi_j(\mathbf{x}_N) & \cdots & \chi_k(\mathbf{x}_N) \end{vmatrix}. \tag{2.7}$$

In addition, the system many-particle wave function could be approximated with a better accuracy using a linear combination of such Slater determinants.

The HF method approximates this many-particle wave function through a single Slater determinant and, by means of a variational principle, selects the best N spin orbitals, among a set of K of them, which give the lowest expectation value for the electronic Hamiltonian. Using the Slater determinant wave function of equation (2.7), we can calculate the expectation value of the electronic Hamiltonian:

$$\langle \hat{H}_{elec} \rangle_{\Phi_{S,elec}} \equiv \langle \Phi_{S,elec} | \hat{H}_{elec} | \Phi_{S,elec} \rangle = \sum_{i}^{k} \langle i|h|i\rangle + \frac{1}{2} \sum_{i,j}^{k} \left([ii|jj] - [ij|ji] \right), \tag{2.8}$$

where the one- and two-electron integrals are given by:

$$\langle i|h|i\rangle = \int \chi_i^*(\mathbf{x}) \left(-\frac{1}{2}\nabla_{\mathbf{x}}^2 - \sum_A \frac{Z_A}{|\mathbf{r} - \mathbf{R}_A|} \right) \chi_i(\mathbf{x})\, d\mathbf{x}; \tag{2.9a}$$

$$[ii|jj] = \int \frac{|\chi_i(\mathbf{x})|^2 |\chi_j(\mathbf{x}')|^2}{|\mathbf{r} - \mathbf{r}'|}\, d\mathbf{x}\, d\mathbf{x}'; \tag{2.9b}$$

$$[ij|ji] = \int \frac{\chi_i^*(\mathbf{x})\chi_j(\mathbf{x})\chi_j^*(\mathbf{x}')\chi_i(\mathbf{x}')}{|\mathbf{r} - \mathbf{r}'|}\, d\mathbf{x}\, d\mathbf{x}'. \tag{2.9c}$$

Integrals in the form of equation (2.9b) are called *Coulomb integrals* since they give the classical electrostatic interaction energy between the charge distributions $|\chi_i(\mathbf{x})|^2$ and $|\chi_j(\mathbf{x}')|^2$. The sum $\frac{1}{2}\sum_{i,j}^{k}[ii|jj]$ of Coulomb integrals is called *Hartree energy*. Integrals in the form of equation (2.9c) are called *exchange integrals* and they have no classical counterpart. The sum $-\frac{1}{2}\sum_{i,j}^{k}[ij|ji]$ of exchange integrals is called *exchange energy*. A single Slater determinant does not consider electron correlation, except through the Pauli exclusion principle, and this make the HF approximation not useful for the study of systems in which electron-correlation effects are not negligible.

It can be shown (e.g. [60]) that the set of N spin orbitals $\{\chi_a, \chi_b, \cdots, \chi_n\}$, forming the Slater determinant which minimize the expectation value of the electronic Hamiltonian ,$\langle \hat{H}_{elec} \rangle_{\Phi_{S,elec}}$ (equation (2.8)), with the constraint that their spatial parts $\phi(\mathbf{r})$ are mutually orthonormal, can be obtained solving the *Hartree-Fock equations*:

$$\hat{f}\phi_a(\mathbf{r}) = \epsilon_a \phi_a(\mathbf{r}). \tag{2.10}$$

Once the spatial orbitals are found solving the Hartree-Fock equations, the spin orbitals are simply obtained from equation (2.6). Despite its simple appearance, equation (2.10) is not linear. The *Fock operator*, $\hat{f}$, has the form:

$$\hat{f} = \hat{h} + \sum_{b=a}^{n} \left(\hat{J}_b - \hat{K}_b \right), \tag{2.11}$$

where $\hat{h}$, $\hat{J}_b$ and $\hat{K}_b$ are, respectively, the *core-Hamiltonian operator*, *Coulomb operator* and *exchange operator*:

$$\hat{h}\phi_a(\mathbf{r}) = \left(-\frac{1}{2}\nabla^2_{\mathbf{x}} - \sum_A \frac{Z_A}{|\mathbf{r} - \mathbf{R}_A|} \right) \phi_a(\mathbf{r}); \tag{2.12a}$$

$$\hat{J}_b\phi_a(\mathbf{r}) = \left(\int \frac{|\phi_b(\mathbf{x}')|^2}{|\mathbf{r} - \mathbf{r}'|}\, d\mathbf{x}' \right) \phi_a(\mathbf{r}); \tag{2.12b}$$

$$\hat{K}_b\phi_a(\mathbf{r}) = \left(\int \frac{\phi^*_b(\mathbf{x}')\phi_a(\mathbf{x}')}{|\mathbf{r} - \mathbf{r}'|}\, d\mathbf{x}' \right) \phi_a(\mathbf{r}). \tag{2.12c}$$

The core-Hamiltonian operator describes a single electron moving in the potential originated by the fixed nuclei. The Coulomb and exchange operators bring into account the electron-electron interaction. The Coulomb operator has a classical interpretation for which it describes the electrostatic potential generated by an electron originating a charge distribution $|\phi_b(\mathbf{x}')|^2$. The exchange operator has no classical analogue, but can be thought as an electrostatic potential generated when an electron is exchanged between two different orbitals: ϕ_b and ϕ_a. Since the orbitals $\{\phi_a, \phi_b, \cdots, \phi_n\}$ explicitly appear in the definition of the Fock operator through the Coulomb and exchange operators, equation (2.10) can only be solved iteratively and this is done through the self-consistent field scheme. Such procedure will be outlined in Section 2.2 through the use of a basis set.

For a closed shell system composed of N electrons, the ground-state electronic energy, equation (2.8), can be written in terms of the $N/2$ Hartree-Fock spatial orbitals $\phi(\mathbf{r})$:

$$E_{elec,0} = 2\sum_{a}^{N/2} \langle a|\hat{h}|a\rangle + \sum_{a}^{N/2}\sum_{b}^{N/2} \left(2[aa, bb] - [ab, ba]\right); \tag{2.13}$$

where the Coulomb, $[aa, bb]$, and exchange, $[ab, ba]$ integrals have analogous form of those in equation (2.9b) and (2.9c), respectively. In terms of the Hartree-Fock eigenvalues:

$$\epsilon_a = \langle a|\hat{f}|a\rangle = \langle a|\hat{h}|a\rangle + \sum_{b}^{N/2} \left(2[aa, bb] - [ab, ba]\right); \tag{2.14}$$

equation (2.13) takes the form:

$$E_{elec,0} = \sum_{a}^{N/2} \Big(\langle a|\hat{h}|a\rangle + \epsilon_a\Big). \tag{2.15}$$

2.1.3. The Density Functional Theory

Density functional theory (DFT) is one of the most successful quantum mechanical method for the investigation of solids. It is an extremely versatile method and finds applications in many branches of natural science; such as physics, chemistry, biology and mineralogy. The success of DFT is mainly due to its flexibility and optimized implementation in computer codes, which allow one to accurately describe a broad variety of systems with affordable computational resources. The core idea of DFT is based on two main papers: the 1964 paper of Hohenberg and Kohn [62], which outlines the two fundamental theorems on which the theory lies, and the 1965 paper of Kohn and Sham [18], which introduces a method for practically solving the many-body quantum mechanical problem within the theory framework. In this subsection, we outline the fundamentals of the original formulation of DFT, which provides only the ground-state properties of the system and is adequate for the work presented in this Thesis.

Equation (2.4a) formulates the fundamental problem of quantum chemistry. For our purposes, the electronic Hamiltonian of equation (2.5a) can be rewritten in a more concise way as:

$$\hat{H} = \hat{T} + \hat{U} + \hat{V}, \tag{2.16}$$

where for a system of N electrons, $\hat{T}$ represents the kinetic energy operator:

$$\hat{T} = -\sum_{j=1}^{N} \frac{1}{2}\nabla_j^2, \tag{2.17}$$

$\hat{U}$ is the electron-electron operator:

$$\hat{U} = \sum_{j=1}^{N}\sum_{k>i}^{N} U(\mathbf{r}_j, \mathbf{r}_k) = \sum_{j=1}^{N}\sum_{k>i}^{N} \frac{1}{|\mathbf{r}_j - \mathbf{r}_k|}, \tag{2.18}$$

and $\hat{V}$ is the external potential operator:

$$\hat{V} = v(\mathbf{r}) = \sum_{j=1}^{N} v(\mathbf{r}_j) = -\sum_{j=1}^{N}\sum_{A=1}^{M} \frac{Z_A}{|\mathbf{r}_j - \mathbf{R}_A|}. \tag{2.19}$$

The operators $\hat{T}$ and $\hat{U}$ are called *universal operators* since their form depends only on the system of N interacting electrons itself, and is thus fixed once the number of electrons has been chosen. The *external potential*, $v(\mathbf{r})$ in equation (2.19), defines the particular properties of the system. According to the form of $v(\mathbf{r})$, we can describe N electrons of a molecule, a solid, a gas or something else.

The key quantity in DFT is the *electronic density* $n(\mathbf{r})$ which is given by the expectation value of the density operator $\hat{n}(\mathbf{r}) = \sum_{j=1}^{N} \delta(\mathbf{r} - \mathbf{r}_j)$ in a given state Ψ:

$$n(\mathbf{r}) = \langle \Psi | \hat{n}(\mathbf{r}) | \Psi \rangle. \tag{2.20}$$

The expectation value of the electronic energy for a system in the state Ψ is therefore:

$$\langle \Psi | \hat{H} | \Psi \rangle = \langle \Psi | \hat{T} + \hat{U} + \hat{V} | \Psi \rangle = \langle \Psi | \hat{T} + \hat{U} | \Psi \rangle + \int n(\mathbf{r}) v(\mathbf{r})\, d\mathbf{r}. \tag{2.21}$$

If Ψ_0 is the exact system ground-state, then $\langle \Psi_0 | \hat{H} | \Psi_0 \rangle = E_0$, where E_0 is the system ground-energy. In their original paper, reference [62], Hohenberg and Kohn proved that, for a given external potential $v(\mathbf{r})$, there exist an *universal* functional of the electronic density, $F[n] \equiv \langle \Psi | \hat{T} + \hat{U} | \Psi \rangle$, which is independent on the external potential itself and has the property that the functional:

$$E[n] \equiv F[n] + \int n(\mathbf{r}) v(\mathbf{r})\, d\mathbf{r} = T[n] + U[n] + V[n], \tag{2.22}$$

has its minimum value equal to the exact ground-state energy E_0. The importance of this result consists in highlighting the role of the electronic density as a fundamental variable for the many-body problem. The two fundamental consequences of this result, are the two Hohenberg-Kohn theorems, which can be summarize as (see for example reference [63]):

1. The *nondegenerate* ground-state wave function, Ψ_0, is *univocally* defined by the ground-state electronic density, n_0, which is in turn uniquely defined by the external potential $v(\mathbf{r})$ (within an additive constant):

$$\Psi_0(\mathbf{r}_1, \mathbf{r}_2, \cdots, \mathbf{r}_N) = \Psi[n_0]. \tag{2.23}$$

There is therefore a one-to-one correspondence between the system ground-state density and its wave function. Since the wave function completely describes a quantum system, it follows that knowing the ground-state electronic density is enough to determine the ground-state expectation value of any physical observable. The ability of DFT to fully describe a system with a function of only three variables (the electronic density) rather than with one of at least $3N$ variables (the wave function) led to a paradigm shift in many-body quantum theory.

2. The system energy generally depends on the external potential v. For a fixed external potential, the energy expectation value, with respect to a state of the system with some density $n' \neq n_0$, is always larger than the energy expectation value for the system in its ground-state:

$$E_v[n_0] = \langle \Psi[n_0] | \hat{H} | \Psi[n_0] \rangle \leq \langle \Psi[n'] | \hat{H} | \Psi[n'] \rangle = E_v[n']. \tag{2.24}$$

This result offers a practical way to find the closest approximation to the ground-state density, n_0, through a variational process in which equation (2.22) is minimized with respect to the density n. However, such process readily leads to an insurmountable problem, since, in general, only the form of the term $V[n]$ of equation (2.21) is known. In practice, it is necessary to represent the functionals $T[n]$ and $U[n]$ through appropriate approximations.

The most widely used approach to implement density functional theory is the Kohn-Sham method [18] which reduces the problem to find the electronic ground-state density, through a minimization of the functional $E[n]$ for a system on interacting electron, to the problem of solving a single-particle Schrödinger equation for a system of non-interacting electrons. Equation (2.22) may be rewritten in such a way to emphasize the presence of functionals of known form. In particular, it is usually considered an auxiliary system of electrons with density n which is exactly described by a single Slater determinant (equation (2.7)), i.e. a system of *uncorrelated* electrons. The orbitals, $\{\phi_j[n]\}$, forming the determinant, are still a functional of the system electronic density; however their introduction allows one to express part of the functional $F[n]$ of equation (2.22) in terms known from the Hartree-Fock method. In particular, for such a system, the energy functional (equation (2.22)) ca be written as:

$$E[n] \equiv F[n] + \int n(\mathbf{r})v(\mathbf{r})\,d\mathbf{r} = T_S(\{\phi_j[n]\}) + U_H(\{\phi_j[n]\}) + U_X(\{\phi_j[n]\}) + V[n], \tag{2.25}$$

where the notation $f(\{\phi_j[n]\})$ emphasizes that the functionals explicitly depend on the single-particle orbitals, ϕ_j, and through them, implicitly on the system density n. T_S, U_H and U_X are, respectively, the kinetic energy, the Hartree energy and the exchange energy, which have the form (cf. with equations (2.9a), (2.9b) and (2.9c), respectively):

$$T_S[n] = -\frac{1}{2}\sum_{j=1}^{N}\int \phi_j^*(\mathbf{r})\nabla^2\phi_j(\mathbf{r})\,d\mathbf{r}; \tag{2.26a}$$

$$U_H[n] = \frac{1}{2}\sum_{i,j=1}^{N}\int\int \frac{\phi_i^*(\mathbf{r})\phi_j^*(\mathbf{r}')\phi_i(\mathbf{r})\phi_j(\mathbf{r}')}{|\mathbf{r}-\mathbf{r}'|}\,d\mathbf{r}\,d\mathbf{r}'; \tag{2.26b}$$

$$U_X[n] = -\frac{1}{2}\sum_{i,j=1}^{N}\int\int \frac{\phi_i^*(\mathbf{r})\phi_j^*(\mathbf{r}')\phi_i(\mathbf{r}')\phi_j(\mathbf{r})}{|\mathbf{r}-\mathbf{r}'|}\,d\mathbf{r}\,d\mathbf{r}'. \tag{2.26c}$$

The *correlation energy* is defined as the difference between the exact energy of the system and the energy obtained by the Hartree-Fock approximation. Therefore, for a general system of electrons, we can express the energy functional by equation (2.25) plus an extra term which takes into account all the correlations effects neglected by the Hartree-Fock method; that is, the universal functional, $F[n]$, introduced by Hohenberg and Kohn can always be written as:

$$\begin{aligned} F[n] \equiv T[n] + U[n] &\equiv T_S[n] + U_H[n] + U_X[n] + E_C[n] \\ &\equiv T_S[n] + U_H[n] + E_{XC}[n], \end{aligned} \tag{2.27}$$

where E_C is called the *correlation energy* and $E_{XC} = U_X + E_C$ is called the *exchange-correlation energy*. In general, in the density functional theory, the exchange energy is different from that obtained from the HF method (equation (2.26c)) and its form is related to the approximation made to study the particular electron system. Furthermore, expressing the exchange-correlation energy as a sum of the exchange and correlation energy is another common approximation due to the difficulty of finding an expression for E_{XC}, even for simple systems. With this formalism, the energy functional for an electronic system with electron density n can be written as:

$$E[n] = T_S[n] + U_H[n] + E_{XC}[n] + V[n]. \tag{2.28}$$

No approximation was made to derive equation (2.28); we simply transfered all the difficulties related in finding the correct functional form of $T[n]$ and $U[n]$ to the problem of finding the functional form of E_{XC}. Indeed, a very important aspect of DFT calculations consists in choosing an adequate approximation of E_{XC}.

It would be possible to obtain the ground-state density by minimizing equation (2.28) with respect to n and invoke the second Hohenberg-Kohn theorem:

$$\begin{aligned} 0 = \frac{\delta E[n]}{\delta n(\mathbf{r})} &= \frac{\delta T_S[n]}{\delta n(\mathbf{r})} + \frac{\delta U_H[n]}{\delta n(\mathbf{r})} + \frac{\delta E_{XC}[n]}{\delta n(\mathbf{r})} + \frac{\delta V[n]}{\delta n(\mathbf{r})} \\ &= \frac{\delta T_S[n]}{\delta n(\mathbf{r})} + v_H(\mathbf{r}) + v_{xc}(\mathbf{r}) + v(\mathbf{r}), \end{aligned} \tag{2.29}$$

where $v_{xc}(\mathbf{r}) \equiv \frac{\delta E_{XC}[n]}{\delta n(\mathbf{r})}$. $v_H(\mathbf{r})$ is the Hartree potential, which for a system of electrons with density n, takes the form:

$$\frac{1}{2} \int \frac{n(\mathbf{r}')}{|\mathbf{r} - \mathbf{r}'|} \, d\mathbf{r}', \tag{2.30}$$

and finally, $v(\mathbf{r})$ is the external potential of equation (2.19) (cf. with equation (2.22)). The idea of Kohn and Sham was to introduce a system of *non-interacting* electrons moving in an external potential v_{ni}. For such non-interacting electrons, equation (2.29) simply becomes:

$$\begin{aligned} 0 = \frac{\delta E_{ni}[n_{ni}]}{\delta n_{ni}(\mathbf{r})} &= \frac{\delta T_{ni}[n_{ni}]}{\delta n_{ni}(\mathbf{r})} + v_{ni}(\mathbf{r}) \\ &= \frac{\delta T_S[n_{ni}]}{\delta n_{ni}(\mathbf{r})} + v_{ni}(\mathbf{r}). \end{aligned} \tag{2.31}$$

Comparing this equation with equation (2.29), we see that both minimizations lead to the same ground-state density, $n = n_{ni}$, *if* v_{ni} is choosen to be equal to:

$$v_{ni}(\mathbf{r}) = v_H(\mathbf{r}) + v_{xc}(\mathbf{r}) + v(\mathbf{r}). \tag{2.32}$$

Therefore, we can find the electronic density which minimizes the energy functional of equation (2.29) by solving the single-particle Schrödinger equation:

$$\left(-\frac{1}{2}\nabla^2 + v_{ni}(\mathbf{r}) \right) \psi_j(\mathbf{r}) = \epsilon_j \psi_j(\mathbf{r}), \tag{2.33}$$

where the potential v_{ni} is expressed as in equation (2.32) and acts as an effective

potential for the auxiliary system of non-interacting electrons. The equations (2.33) are called the *Kohn-Sham equations*; the ground-state electronic density can be retrieved from the Kohn-Sham orbitals $\{\psi_j(\mathbf{r})\}$, noticing that for an non-interacting electron gas the electronic density is simply:

$$n(\mathbf{r}) = \sum_{j=1}^{N} f_j |\psi_j(\mathbf{r})|^2, \tag{2.34}$$

where f_j is the occupational number of the orbital ψ_j. The Kohn-Sham equations are solved iteratively, in an analogous way as in the Hartree-Fock equations. The general procedure is outlined in Section 2.2.

We can express the system electronic ground-state energy, equation (2.28), in term of the Kohn-Sham eigenvalues, $\epsilon_j = \langle j|-1/2\nabla^2|j\rangle + \langle j|v_{ni}|j\rangle$, which sum gives the total energy of the auxiliary non-interacting system: $E_{ni}[n] = T_s[n] + V_{ni}[n]$. The various terms of equation (2.28) can be expressed as a function of the electron density n:

$$T_s[n] = \sum_{j}^{N} \epsilon_j - V_{ni}[n]; \tag{2.35}$$

next, the Hartree energy, $U_H[n]$ is given by:

$$U_H[n] = \frac{1}{2}\int v_H(\mathbf{r})\, d\mathbf{r} = \frac{1}{2}\int\int \frac{n(\mathbf{r})n(\mathbf{r}')}{|\mathbf{r}-\mathbf{r}'|}\, d\mathbf{r}\, d\mathbf{r}'; \tag{2.36}$$

and finally, from equation (2.32), we can find the value of $V[n]$:

$$\begin{aligned} V[n] = \int v(\mathbf{r})n(\mathbf{r})\, d\mathbf{r} &= \int \left[v_{ni}(\mathbf{r}) - v_H(\mathbf{r}) - v_{xc}(\mathbf{r})\right] n(\mathbf{r})\, d\mathbf{r} \\ &= V_{ni}[n] - \int \left[v_H(\mathbf{r}) + v_{xc}(\mathbf{r})\right] n(\mathbf{r})\, d\mathbf{r} \\ &= V_{ni}[n] - 2U_H[n] - \int v_{xc}(\mathbf{r})n(\mathbf{r})\, d\mathbf{r}. \end{aligned} \tag{2.37}$$

Plugging the results of the last three equations into the corresponding term of equation (2.28), we obtain the expression:

$$E_{elec,0} = \sum_{j}^{N} \epsilon_j - \frac{1}{2}\int\int \frac{n_0(\mathbf{r})n_0(\mathbf{r}')}{|\mathbf{r}-\mathbf{r}'|}\, d\mathbf{r}\, d\mathbf{r}' - \int v_{xc}(\mathbf{r})n_0(\mathbf{r})\, d\mathbf{r} + E_{XC}[n_0]. \tag{2.38}$$

In practice, the solution of the Kohn-Sham equations, (2.33), requires two main

approximations: the choice of the basis set used to express the Kohn-Sham orbitals, and the choice of the functional which approximates the exchange-correlation energy $E_{XC}[n]$. Considerations related to the basis set will be outlined in Section 2.2; here we will briefly introduce the most common functionals used to approximate $E_{XC}[n]$.

Local Functionals

Local functionals give the first and most important type of approximation for the exchange-correlation energy. The most relevant local functional for estimate the exchange-correlation energy is given by the Local Density Approximation (LDA) [62, 18]:

$$E_{XC}^{LDA} = \int n(\mathbf{r})\varepsilon_{xc}[n]\, d\mathbf{r}, \tag{2.39}$$

where ε_{xc} is the exchange-correlation energy per particle for the system with density $n(\mathbf{r})$. It is related to the exchange-correlation potential $v_{xc}(\mathbf{r})$ of equation (2.29) by:

$$v_{xc}(\mathbf{r}) \approx v_{xc}^{LDA}(\mathbf{r}) = \varepsilon_{xc}[n] + n(\mathbf{r})\frac{\delta\varepsilon_{xc}[n]}{\delta n(\mathbf{r})}. \tag{2.40}$$

For practical purposes, $\varepsilon_{xc}[n]$ is then split into the exchange and correlation contributions. The exchange part is estimated considering an homogeneous interacting gas with constant density n, a many-body problem studied in the 1930s for which the exchange energy can be analytically found [64]:

$$\varepsilon_x[n] = -\frac{3}{4}\left(\frac{3}{\pi}\right)^{\frac{1}{3}} n. \tag{2.41}$$

Within the local density approximation, the density of the general inhomogeneous system $n(\mathbf{r})$ is locally treated as the density of the homogeneous electron gas; therefore:

$$\varepsilon_x[n] \equiv -\frac{3}{4}\left(\frac{3}{\pi}\right)^{\frac{1}{3}} n(\mathbf{r}). \tag{2.42}$$

The correlation part of ε_{xc} is not known even for the homogeneous interacting gas and, nowadays, is usually estimated through Quantum Montecarlo Calculations [65].

The LDA has proven to be extremely successful for a great variety of solid systems; in particular metals, where the electron density slowly varies in space and the system behaves similarly to the homogeneous interacting electron gas, and semicon-

ductors which bonds have *sp* character. In the latter case, the good results obtained by LDA, are actually caused by a systematic error cancellation, since LDA understimates the correlation energy but overestimates the exchange energy [66, 67] . On the other hand, the LDA tends to over-bind molecules and the disagreement with experiments is particularly severe for weakly-bonded system where van der Waals forces or hydrogen bonds are relevant [68].

Semi-local Functionals

To improve the description of an inhomogeneous electron system, it seemed reasonable, at the beginning of DFT, to include in the expression of the exchange-correlation energy also the gradient of the electron-density and higher order terms. Such a series expansion of the electron density, around the uniform limit considered in the LDA, was thought to explicitly take into account the inhomogeneity of the systems electron density. On this idea is based the gradient expansion approximation (GEA) [62]:

$$E_{XC} \approx E_{XC}^{GEA} = E_{XC}^{LDA} + \int C_{xc}[n] \frac{|\nabla n(\mathbf{r})|^2}{n(\mathbf{r})^{4/3}} \, d\mathbf{r}, \tag{2.43}$$

where the gradient coefficient C_{xc} is known [69]. Unfortunately, the GEA does not give any noticeable improvement over the LDA. Higher terms in the expansion of n are furthermore difficult to calculate and, therefore, these kind of approximation are not commonly employed. A different approach consisted in express the exchange-correlation energy, not as a series expansion of the electron density, but as a function of some general functional of both n and ∇n:

$$E_{XC} \approx E_{XC}^{GGA} = \int f[n(\mathbf{r}), \nabla n(\mathbf{r})] \, d\mathbf{r}. \tag{2.44}$$

Such an expression for the exchange-correlation energy has been named general gradient approximation (GGA) [70]. Different GGAs are possible, according to the functional form of $f[n(\mathbf{r}), \nabla n(\mathbf{r})]$. These GGAs are usually obtained by fitting some parameters; either to experimental data, obtained for a particular sample of compounds, or to correctly describe physical constraints on the system. Two of the most popular GGAs are the functionals proposed by Perdew, Burke and Ernzerhof (PBE) [71] and the functional BLYP, obtained from the combination of the exchange functional proposed by Becke [72] and the correlation functional of Lee, Yang and Parr [73].

The GGAs offer a noticeable improvement over LDA, in particular in describing covalent and hydrogen-bonded systems. On the other hand, as LDA, it poorly

estimates the band gap of semiconductors and insulator solids and it fails to describe van der Waals interactions.

Non-local Functionals

The severe underestimate of the band gap of semiconductors and insulators by LDA and GGA is a well known issue in the implementation of DFT for solids [74]. The fundamental gap is defined as the difference between the system ionization energy, I, and (negative) electron affinity, A, and represents the minimum energy difference between the system ground-state and an excited state. Ionization energy and electron affinity for the species X are respectively defined by the reactions:

$$X \to X^+ + e^-, \tag{2.45}$$

$$X^- \to X + e^-. \tag{2.46}$$

Setting the energy reference of the vacuum level to zero, we can calculate I and A, relative to a neutral system with N electrons, through the total energies:

$$I = E_0(N-1) - E_0(N); \tag{2.47}$$

$$A = E_0(N) - E_0(N+1), \tag{2.48}$$

where $E_0(M)$ represents the ground-state energy of the M-electron system. Janak's theorem [75] helps to give some physical significance to the Kohn-Sham eigenvalues (ϵ_j in the Kohn-Sham equations (2.33)). It states that the derivative of the system energy, equation (2.28), with respect to the occupational number of the j-th Kohn-Sham eigenfunction, f_j, is equal to the Kohn-Sham j-th eigenvalue ϵ_j:

$$\frac{\partial E}{\partial f_j} = \epsilon_j. \tag{2.49}$$

From equation (2.49), it follows that:

$$-I = E_0(N) - E_0(N-1) = \int_0^1 \epsilon_N(N-1+f)\, df, \tag{2.50}$$

$$-A = E_0(N+1) - E_0(N) = \int_0^1 \epsilon_{N+1}(N+f)\, df, \tag{2.51}$$

where $\epsilon_M(S+f)$ is the M-th eigenvalue of the M-th Kohn-Sham eigenfunction for the $S+f$-electron system. In practice, when one considers extended systems such

as solids, $M \to \infty$ and adding or removing one electron affects in a negligible way the ground-state density and, thus, the Kohn-Sham eigenvalues. Therefore, it is commonly accepted to approximate I and A for a crystal with N electron as:

$$I = -\epsilon_N(N) = -\epsilon_{VBM}(N); \tag{2.52}$$

$$A = -\epsilon_{N+1}(N) = -\epsilon_{CBM}(N), \tag{2.53}$$

where $\epsilon_{VBM}(N)$ and $\epsilon_{CBM}(N)$ are, respectively, the Kohn-Sham eigenvalues of the valence band maximum and conduction band minimum of the N-electron crystal. The fundamental gap of solids is commonly calculated in first-principles calculations through these single-particle eigenvalues: $E_g = \epsilon_{CBM}(N) - \epsilon_{VBM}(N)$. Calculating the band gap in this way is a very convenient approximation because it requires just a single band structure calculation instead of three and, foremost, it avoids altogether the problem of calculate the total energy of a charged periodic system . However, for LDA and GGA, this approach severely underestimates the band gap and this issue is known as the "energy gap problem".

The error behind the relation $E_g = \epsilon_{CBM}(N) - \epsilon_{VBM}(N)$, consists in the fact that even for an infinitesimal change in the density n, due to the removal of one electron from an infinite crystal, the exchange-correlation energy has, in general, a discontinuity with respect to the number of electrons in the system:

$$\left.\frac{\delta E_{XC}[n]}{\delta n}\right|_{N+\sigma} - \left.\frac{\delta E_{XC}[n]}{\delta n}\right|_{N-\sigma} = v^{+}_{xc}(\mathbf{r}) - v^{-}_{xc}(\mathbf{r}) \neq 0, \tag{2.54}$$

for any $\sigma > 0$ [76, 77]. Therefore, the Kohn-Sham eigenvalues predict, in general, the fundamental band gap plus a system-dependent constant equal to $v^{+}_{xc}(\mathbf{r}) - v^{-}_{xc}(\mathbf{r})$. Such a constant is generally positive and, therefore, the Kohm-Sham implementation of DFT will generally underestimate the band gap. The underestimation is particularly severe in LDA and GGA, which also fail to reproduce the discontinuity in the exchange-correlation energy.

It has been shown that non-local, and in particular orbital-dependent, functionals are able, on the other hand, to predict very accurately the band gap values through the single-particle eigenvalues. One example of orbital-dependent functionals is the self-interaction correction (SIC) [78], introduced to remove the spurious self-interaction term in the LDA and GGAs. The main idea behind SIC is to subtract, from each Kohn-Sham orbital, the Hartree and exchange-correlation energy corresponding to a single-electron system. The self-interaction term particularly affects systems with very localized electrons, such as transition-metal compounds, which

are overdelocalized within the LDA and GGAs, and thus SIC offers a good solution to this problem. Another orbital-dependent approach is that of the Meta-GGA functionals, for which the exchange-correlation energy is a functional of the density, n, its gradient ∇n and the orbital-dependent Kohn-Sham kinetic energy density $\tau(\mathbf{r})$ [79]:

$$\tau(\mathbf{r}) = \frac{1}{2}\sum_j |\nabla\psi_j(\mathbf{r})|^2 \,. \tag{2.55}$$

The most popular class of orbital-dependent functionals is probably that of hybrid functionals. The basic approach was originally proposed by Becke in the 1990s [80] and consists in correcting the exchange-correlation energy by incorporating a fraction of the Hartree-Fock non-local exchange energy (equation (2.26c)). The remaining contribution to the exchange-correlation energy is usually taken from LDA or GGAs; the ratio between the various terms in the expression of E_{XC} is tuned by a variable number of parameters which are generally found empirically, for example by calibration on a wide class of molecules. The theory of hybrid functionals is justified by the adiabatic connection formula [81], which allows one to decompose the exchange-correlation energy, $E_{XC}[n]$, with respect to the coupling strength constant λ:

$$E_{XC}[n] = \int_0^1 E_{XC,\lambda}[n]\, d\lambda. \tag{2.56}$$

This constant describes the strength of the system electron-electron interaction. For $\lambda = 0$, electrons interact weakly between each other and therefore the Hartree-Fock method represents an adequate approximation; whereas, for a strong electron-electron coupling DFT is better suited. Remarkably, hybrid functionals predict with a high accuracy both the fundamental band gap, due to the orbital-dependence of the Hartree-Fock exchange, and correct the self-interaction error, again thanks to the presence of the Hartree-Fock exchange. Perhaps, the most popular functional in quantum chemistry of molecules is the Becke-three-parameter-Lee-Yang-Parr hybrid functional (B3LYP), which combine the Becke-Lee-Yang-Parr (BLYP) GGA correlation [73] with the Becke three-parameters B3 hybrid functional [82].

In this Thesis, we employed the PBE0 hybrid functional [83]. It consists in mixing the Hatree-Fock exchange, E_X^{HF}, with the Perdew-Burke-Ernzerhof (PBE) exchange [71], E_X^{PBE}, in ratio 1:3; while keeping the PBE correlation energy, E_C^{PBE}:

$$E_{XC} \approx E_{XC}^{PBE0} = \frac{1}{4}E_X^{HF} + \frac{3}{4}E_X^{PBE} + E_C^{PBE}. \tag{2.57}$$

This functional is attractive since it does not rely on fitted parameters and avoids

the empiricism of traditional hybrid functional; as a matter of fact, the parameters values are fixed according to physical constraints (the choice of 25% of HF exchange in equation (2.57) is justified by some general considerations [84]) rather than by fitting to experimental data as done for B3LYP and other hybrid functionals. In particular, this functional has shown to be particularly suitable for the study of perovskite materials and surfaces [21].

2.2. The Linear Combination of Atomic Orbitals in Periodic Systems

Solving either the Hartree-Fock equations (equation (2.10)) or the Kohn-Sham equations (equation (2.33)), requires to find an analytical expression of the HF or KS orbitals, respectively. As the name suggests, the linear combination of atomic orbitals (LCAO) method approximates the one-electron (molecular) HF or KS orbitals through a linear combination of localized atomic orbitals. For periodic systems, both the Fock operator and the Kohn-Sham Hamiltonian are invariant under the action of the underlining lattice translations and therefore, according to Bloch's theorem, the single-electron wave function will have the form:

$$\psi_{\mathbf{k}}(\mathbf{r}) = e^{i\mathbf{k}\cdot\mathbf{r}} u_{\mathbf{k}}(\mathbf{r}), \tag{2.58}$$

where $u_{\mathbf{k}}(\mathbf{r})$ is a periodic function, with the same periodicity of the crystalline lattice, and $\mathbf{k}$ is the wave function wave vector which labels the $\mathbf{k}$-th irreducible representation of the crystal translational group [61]. To be able to normalize the functions in equation (2.58), periodic boundary conditions are imposed. These conditions consider a finite crystal made of $M = M_1 M_2 M_3$ unit cells (with $M \to \infty$ and where the subscript j indicates the number of cells along the lattice vector $\mathbf{a}_j$) and assume the cyclic relation between translations:

$$\mathbf{r} + mM_j\mathbf{a}_j = \mathbf{r} \qquad \text{for any integer } m \text{ and } j = 1, 2, 3. \tag{2.59}$$

We denote, hereafter, with ψ a general HF or KS orbital since the LCAO formulation is formally identical both for the HF and the KS equations. In the framework of quantum chemistry of molecules, such ψ are called *molecular orbitals* (MOs); while when periodic systems are considered, they are referred as *crystalline orbitals* (COs).

The LCAO is extremely popular in the quantum chemistry of molecules and the basis functions used for solids are derived from those employed for molecules. The general idea behind the concept of a basis set is the search for a (finite) set

of functions which can accurately approximate a given family of functions, in our case the COs. The LCAO proposes to use as basis functions single-electron atomic orbitals (AOs). For building a CO, AOs are chosen in the reference primitive cell (denoted by the lattice vector $\mathbf{0}$) and are replicated in all the other primitive cells (labeled by the lattice vector $\mathbf{R_n}$). If we denote the AO of type ν of the atom in position μ in the $\mathbf{R_n}$-cell, as $\chi_\nu(\mathbf{r}-\mathbf{r}_\mu-\mathbf{R_n})$, one can build a function with the translational symmetry of the lattice using a combination of such AOs:

$$u_{\nu,\mathbf{k}}(\mathbf{r}) = \frac{1}{\sqrt{M}} e^{-i\mathbf{k}\cdot\mathbf{r}} \sum_{\mathbf{R_n}\mu} e^{i\mathbf{k}\cdot\mathbf{R_n}} \chi_\nu(\mathbf{r}-\mathbf{r}_\mu-\mathbf{R_n}), \tag{2.60}$$

where the μ-sum runs over all the atoms of type μ in the $\mathbf{0}$-cell. From this function one can build the Bloch function of type ν by multiplying the function of equation (2.60) by a plane wave:

$$\phi_{\nu,\mathbf{k}}(\mathbf{r}) = \frac{1}{\sqrt{M}} \sum_{\mathbf{R_n}\mu} e^{i\mathbf{k}\cdot\mathbf{R_n}} \chi_\nu(\mathbf{r}-\mathbf{r}_\mu-\mathbf{R_n}). \tag{2.61}$$

Finally, one can express the n-th CO as a linear combination of the Bloch functions of equation (2.61):

$$\psi_{\mathbf{k},n}(\mathbf{r}) = \sum_\nu c_{\nu,n}(\mathbf{k})\phi_{\nu,\mathbf{k}}(\mathbf{r}). \tag{2.62}$$

In the basis of Bloch functions $\phi_{\nu,\mathbf{k}}(\mathbf{r})$, we can express the HF or KS equations in matrix form:

$$\mathbf{H}(\mathbf{k})\mathbf{C}(\mathbf{k}) = \mathbf{S}(\mathbf{k})\mathbf{C}(\mathbf{k})\mathbf{E}(\mathbf{k}), \tag{2.63}$$

where the entries for the matrix $\mathbf{H}(\mathbf{k})$ are given by $H^{\mathbf{R_n}}_{\nu\rho}(\mathbf{k}) = \langle\phi_{\nu,\mathbf{k}}(\mathbf{r}-\mathbf{r}_\mu)|\hat{H}|\phi_{\rho,\mathbf{k}}(\mathbf{r}-\mathbf{r}_\mu-\mathbf{R_n})\rangle$ (the operator $\hat{H}$ can be either the Fock operator or the Kohn-Sham Hamiltonian), $\mathbf{C}(\mathbf{k})$ is the matrix of the coefficients, $c_{\nu,n}(\mathbf{k})$, and the overlap matrix $\mathbf{S}(\mathbf{k})$ takes into account the non-orthogonality of the Bloch functions of equation (2.61), $S^{\mathbf{R_n}}_{\nu\rho}(\mathbf{k}) = \langle\phi_{\nu,\mathbf{k}}(\mathbf{r}-\mathbf{r}_\mu)|\phi_{\rho,\mathbf{k}}(\mathbf{r}-\mathbf{r}_\mu-\mathbf{R_n})\rangle$.

In principle, the analytical formula of the AOs is known, but it is too complicated to be practically handled. Therefore, the AOs are themselves typically expressed as a linear combination of a given number of simpler functions. The choice normally falls on Gaussian-type functions (GTFs) which are particular useful, given the large number of integrals in equation (2.63) and the possibility to calculate analytically integrals involving GTFs. The GTF centered on the atom in position $\mathbf{R}_\mu$ has the following form:

$$g^{GTF}_P(\mathbf{r}-\mathbf{R}_\mu) = Ax^l y^m z^n e^{-\alpha|\mathbf{r}-\mathbf{R}_\mu|^2}, \tag{2.64}$$

where α is the GTF exponent, which describe the extension of the GTF in space, A is the normalization constant and l, m, n are natural numbers which define the GTF angular momentum quantum number, $L = l + m + n$. A GTF with angular momentum L, or a linear combination thereof, approximates an atomic orbital with the same angular momentum quantum number. GTFs are easy to handle, but a single GTF describes an AO quite poorly; especially for $\mathbf{r} \to \mathbf{R}_\mu$ and for $\mathbf{r} \to \infty$. A more accurate analytical approximation of AOs are given by Slater-type functions (STFs):

$$\chi^{STF}_{nlm}(\mathbf{r} - \mathbf{R}_\mu) = A|\mathbf{r} - \mathbf{R}_\mu|^{n-1} e^{-\zeta|\mathbf{r}-\mathbf{R}_\mu|} Y_{l,m}(\theta, \phi), \tag{2.65}$$

where $Y_{l,m}(\theta, \phi)$ is the l, m-th spherical harmonic and ζ is the STF exponent. STFs are however much more computationally expensive than GTFs; therefore, in practice, most LCAO codes approximate STFs with a certain number of GTFs, called *primitive Gaussians*. The STFs resulting from the linear combination of Gaussian primitives are called *contractions* and the basis set employed in the calculation is formed by these contractions. The use of contractions, instead of primitive Gaussians only, allows one to employ a smaller number of total primitive Gaussians keeping the same accuracy. In general a contraction has the form:

$$\chi^c_j(\mathbf{r} - \mathbf{R}_\mu) = \sum_{k=1}^{N_c} d_k g^{GTF}_P(\mathbf{r} - \mathbf{R}_\mu); \tag{2.66}$$

where the primitive Gaussians used to form the contraction have the same L but different exponents α. By tuning the contraction coefficients d_k, the number of primitive Gaussians N_c and the exponents α, it is possible to approximate any AO.

We will now outline the general procedure to solve equation (2.63) employed in the LCAO approach for solids.

1. A basis set $\{\chi_{nu}\}$ is chosen for describing the AOs of the atoms forming the system. Each AO is represented by a contraction of primitive Gaussians. The COs (equation (2.62)) are formed using an initial guess for the value of the coefficients $\{c_{\nu,n}\}$. In practice and in a completely equivalent way, the initial guess is made on the *density matrix* $P_{\nu,\rho}(\mathbf{k}) = \sum_n c^*_{\nu,n}(\mathbf{k}) c_{\rho,n}(\mathbf{k})$.

2. The elements of the Hamiltonian matrix $\mathbf{H}$ are evaluated:

$$H^{\mathbf{R_n}}_{\nu\rho} = \langle \phi_\nu(\mathbf{r} - \mathbf{r}_\mu) | \hat{H} | \phi_\rho(\mathbf{r} - \mathbf{r}_\mu - \mathbf{R_n}) \rangle, \tag{2.67}$$

   where $\mathbf{R_n}$ indicates that the considered AO lies in the $\mathbf{R_n}$-th unit cell.

3. The overlap matrix $\mathbf{S}$, the density matrix $\mathbf{P}(\mathbf{k})$ and the Hamiltonian matrix $\mathbf{H}$ are also evaluated, with respect to the Bloch functions of equation (2.61), for any wave vector $\mathbf{k}$:

$$H_{\nu\rho}(\mathbf{k}) = \sum_{\mathbf{R_m}} e^{i\mathbf{k}\cdot\mathbf{R_m}} \langle \phi_\nu(\mathbf{r}-\mathbf{r}_\mu)|\hat{H}|\phi_\rho(\mathbf{r}-\mathbf{r}_\mu-\mathbf{R_m})\rangle. \tag{2.68}$$

   An analogous formula holds for the overlap and density matrices. Equation (2.68) is the Fourier transform of the Hamiltonian matrix of equation (2.67) and includes information about the reciprocal space influence over the Hamiltonian.

4. Equation (2.63) is solved, giving the entries of $\mathbf{E}(\mathbf{k})$ (eigenvalues) and $\mathbf{C}(\mathbf{k})$.

5. The eigenvalues are filled according to the Aufbau principle: the lowest available energy levels are filled before any other level with higher energy. The Fermi energy E_F is determined as the highest energy value among the occupied state energies (at every $\mathbf{k}$).

6. A new density matrix is then formed from $\mathbf{C}(\mathbf{k})$. In particular, the density matrix is obtained as the Fourier anti-transform of the density matrix representation in reciprocal space of step 3.

7. Steps 3 through 6 are repeated until the new obtained density matrix differs from the one obtained in the the previous iteration by less than a predefined threshold value. When this happens at the outlined cycle, it is said to have reached self-consistency.

8. Once the self-consistency is reached, the system ground-state properties can be calculated employing the self-consistent density matrix.

The self-consistent procedure outlined above is similar to the analogous procedure employed for molecules; the two main differences are that matrix elements have to be evaluated for AOs in an infinite number of primitive cells and that they have to take into account an infinite number of reciprocal space points $\mathbf{k}$. In practice, one can handle only a finite number of matrix elements. For the direct space sums, threshold parameters are introduce in such a way to set to zero the matrix elements arising from AOs which overlap less than the threshold value (for more details see CRYSTAL manual, reference [58]). For the reciprocal space sums, the finite number of $\mathbf{k}$-points to take into account is specified by some algorithm. The most popular was proposed by Monkhorst and Pack [85] and consists to create a

homogeneous mesh of reciprocal lattice points in the first Brillouin zone by choosing a given number of **k**-points to take into account along each of the reciprocal lattice basis vectors. As a general rule, the mesh is built to avoid **k**-points with high symmetry, since this would reduce the number of symmetry-independent points in the reciprocal space summations. However, for semiconductors and insulators, even a small number of **k**-points (on the order of 100) could already be sufficient for obtaining convergence of the the reciprocal lattice sums. More details on quantum chemical methods for solids can be found in reference [61].

2.3. The Calculation of Vibrational Frequencies in Solids and the Frozen-Phonon method

This section summarizes the usual techniques employed to calculate the vibrational frequencies and normal modes of a solid system within a first-principles scheme. A more complete general introduction can be found in textbooks (for example, [86]); while the specific way in which the computer code CRYSTAL calculates vibrational frequencies can be found in reference [87].

2.3.1. Classical Determination of the Normal Modes of Vibration and their Characteristic Frequencies

The calculation of vibrational frequencies in solids is related to the old problem of finding the normal modes, and their characteristic frequencies, for a system of coupled oscillators. Consider a crystal with p atoms in the primitive unit cell and let $\mathbf{R}_\alpha(0) = (R_{1,\alpha}(0), R_{2,\alpha}(0), R_{3,\alpha}(0))$ $(\alpha = 1, 2, \cdots, p)$ be the Cartesian coordinates of atom α in the equilibrium configuration. Due to the translational symmetry of the crystal, for every direct lattice vector $\mathbf{T} = \sum_{j=1}^{3} n_j \mathbf{a}_j = (n_1, n_2, n_3) = \mathbf{n}$, we have an atom with coordinates $\mathbf{R}_\alpha(0) + \mathbf{T} = \mathbf{R}_{\alpha,\mathbf{n}}(0)$ $(\alpha = 1, 2, \cdots, p)$. We will use the notation $R_{i,\alpha,\mathbf{n}}$ to indicate the i-th Cartesian coordinate for the atom α in the **n**-th unit cell.

The atoms will generally oscillate around their equilibrium position and their trajectories are described by some vector valued function:

$$\mathbf{R}(t) = (\mathbf{R}_1(t), \mathbf{R}_2(t), \cdots, \mathbf{R}_p(t), \mathbf{R}_{1,(1,0,0)}(t), \mathbf{R}_{2,(1,0,0)}(t), \cdots), \tag{2.69}$$

where one has to sum over all the direct lattice vectors $\mathbf{T} = (n_1, n_2, n_3) = \mathbf{n}$. For notational convenience, we use the symbol $\mathbf{R}(t)$ also for indicating the column

vector:

$$\begin{bmatrix} \mathbf{R}_1(t) \\ \mathbf{R}_2(t) \\ \vdots \\ \mathbf{R}_p(t) \\ \vdots \end{bmatrix} = \begin{bmatrix} R_{1,1}(t) \\ R_{2,1}(t) \\ R_{3,1}(t) \\ R_{1,2}(t) \\ \vdots \\ R_{1,p}(t) \\ R_{2,p}(t) \\ R_{3,p}(t) \\ \vdots \end{bmatrix}, \tag{2.70}$$

We can express the crystal potential $V(\mathbf{R}(t))$ as a Taylor series around the equilibrium configuration and we will include only terms up to the second order (*harmonic approximation*). This is a valid approximation if we assume the amplitude of atomic vibrations to be rather small (i.e. temperatures far from the melting point). Noticing that in the equilibrium configuration the forces acting on the atoms are zero, the potential expansion acquires a rather simple form:

$$V(\mathbf{R}(t)) = V(\mathbf{R}(0)) + \frac{1}{2}\mathbf{u}^{\mathsf{T}}\mathbf{D}^2[V(\mathbf{R}(0))]\mathbf{u}, \tag{2.71}$$

where the column vector $\mathbf{u}$ represents the atomic displacements with respect to the equilibrium configuration: $\mathbf{u} = \mathbf{u(t)} = \mathbf{R}(t) - \mathbf{R}(0)$ and $\mathbf{D}^2[V(\mathbf{R}(0))]$ is the Hessian matrix of $V(\mathbf{R}(0))$, and each of its entries defines a force constant:

$$\mathbf{D}^2[V(\mathbf{R}(0))]_{i\alpha\mathbf{n},j\beta\mathbf{m}} = \left[\frac{\partial V(\mathbf{R})}{\partial R_{i\alpha\mathbf{n}}\partial R_{j\beta\mathbf{m}}}\right]_{\mathbf{R}=\mathbf{R}(0)} = \left[\frac{\partial V(\mathbf{R})}{\partial u_{i\alpha\mathbf{n}}\partial u_{j\beta\mathbf{m}}}\right]_{\mathbf{R}=\mathbf{R}(0)}. \tag{2.72}$$

Equation (2.71) represents the potential energy of a system of coupled harmonic oscillators and the force acting on atom α in the $\mathbf{n}$-th unit cell, along the Cartesian direction i, is given by:

$$F_{i\alpha\mathbf{n}} = -\frac{\partial V(\mathbf{R})}{\partial u_{i\alpha\mathbf{n}}} = -\sum_{j\beta\mathbf{m}} \mathbf{D}^2[V(\mathbf{R}(0))]_{i\alpha\mathbf{n},j\beta\mathbf{m}} u_{j\beta\mathbf{m}}, \tag{2.73}$$

therefore, the newtonian equations of motion take the form:

$$\mathbf{M}\ddot{\mathbf{u}} = -\mathbf{D}^2[V(\mathbf{R}(0))]\mathbf{u}, \tag{2.74}$$

where $\mathbf{M}$ represents the mass matrix: $\mathbf{M}_{i\alpha\mathbf{n},j\beta\mathbf{m}} = m_\alpha \delta_{i\alpha\mathbf{n},j\beta\mathbf{m}}$. A solution of the

differential equation (2.74) can be found using the ansatz:

$$u_{j\alpha\mathbf{n}}(t) = U_{j\alpha}(\mathbf{q})e^{i(\mathbf{q}\mathbf{R}_{\alpha\mathbf{n}}-\omega(\mathbf{q})t)}. \tag{2.75}$$

Equation (2.75) defines the system *normal modes of vibration*, characterized by the wave vector $\mathbf{q}$ and frequency $\omega(\mathbf{q})$. Note that for each unit cell, containing p atoms, and for a fixed $\mathbf{q}$, there are $3p$ different normal modes. Furthermore, the three normal modes relative to atom α in the unit cell $\mathbf{n}$ differ from those relative to the same atom in the primitive unit cell situated at the origin, only by a phase factor $exp[i(\mathbf{qn})]$ (see equation (2.75)). This phase factor arises from the translational symmetry of the crystal and, as for electronic states, the number of wave vectors $\mathbf{q}$ is equal to the number of distinct irreducible representations of the crystal translational group, which is, in turn, equal to the number of primitive unit cells in the crystal (assuming periodic boundary conditions are applied). Therefore, each $\mathbf{q}$ can be represented by a point in the crystal first Brillouin zone.

Substituting equation (2.75) into equation (2.74), we obtain simple algebraic equations:

$$\begin{aligned} &-\omega^2\mathbf{M}\mathbf{u} = -\mathbf{D}^2[V(\mathbf{R}(0))]\mathbf{u} \\ \longrightarrow &\left(\mathbf{D}^2[V(\mathbf{R}(0))] - \omega^2\mathbf{M}\right)\mathbf{u} = 0 \\ \longrightarrow &\left(\mathbf{M}^{-1}\mathbf{D}^2[V(\mathbf{R}(0))] - \omega^2\mathbf{I}\right)\mathbf{u} = 0. \end{aligned} \tag{2.76}$$

Equation (2.76) is s system of $3pN$ linear equations, where p is the number of atoms in the primitive unit cell and N is the number of unit cells in the crystal (and thus the number of wave vectors $\mathbf{q}$). The square frequencies, ω^2, are the eigenvalues of the matrix $\mathbf{M}^{-1}\mathbf{D}^2[V(\mathbf{R}(0))]$ and can be found by solving the characteristic equation of equation (2.76):

$$\det\left(\mathbf{M}^{-1}\mathbf{D}^2[V(\mathbf{R}(0))] - \omega^2\mathbf{I}\right) = 0. \tag{2.77}$$

Since $\mathbf{M}^{-1}\mathbf{D}^2[V(\mathbf{R}(0))]$ is a self-adjoint matrix, its eigenvalues are real numbers and thus the normal modes frequencies, ω, will be real too. We thus have $3p$ vibrational frequencies for each point $\mathbf{q}$. For a very large N, interpolation methods allow to express ω as a continuous function of $\mathbf{q}$; the functional relation $\omega(\mathbf{q})$ is called *dispersion relation*. Since any $\mathbf{q}$ belongs to the first Brillouin zone, we have $3p$ *branches* of the dispersion relation inside the Brillouin zone. Once the normal modes frequencies are found, we can substitute their values in equation (2.76) and solve for $U_{j\alpha}(\mathbf{q})$. This finally determines the form of the vibrational normal modes.

The secular equation, equation (2.76), can be more easily solved through symmetry arguments, which can be used to simplify the Hessian matrix. For example:

- Since the potential energy $V(\mathbf{R})$ is in general a smooth function, then the Hessian matrix is symmetric:

$$\mathbf{D}^2[V(\mathbf{R}(0))]_{i\alpha\mathbf{n},j\beta\mathbf{m}} = \mathbf{D}^2[V(\mathbf{R}(0))]_{j\beta\mathbf{m},i\alpha\mathbf{n}}$$

- The translational symmetry of the crystal implies that

$$\mathbf{D}^2[V(\mathbf{R}(0))]_{i\alpha\mathbf{n},j\beta\mathbf{m}} = \mathbf{D}^2[V(\mathbf{R}(0))]_{i\alpha\mathbf{0},j\beta(\mathbf{m}-\mathbf{n})}$$

- Additional simplifications occur if the space group symmetry of the particular system is considered.

2.3.2. First-principles Determination of the Hessian Matrix: the Frozen-Phonon Method

In first-principles calculations, the crystal potential, $V(\mathbf{R}(t))$, is generally taken as the system total energy (the potential energy surface of equation (2.5b)) within the Born-Oppenheimer approximation:

$$V(\mathbf{R}(t)) = E_{PES}(\{\mathbf{R}_A\}). \tag{2.78}$$

To calculate phonons and their characteristic frequencies, through the classical approach outlined in Section 2.3.1, it is necessary to compute the force constants, equation (2.72). There are two main approaches to this issue: the *frozen-phonon method* and the *density functional perturbation theory* (DFPT). The former is the older approach, common in the study of molecules and easy to implement also in solids. It is also the approach employed in this Thesis and is briefly described below.

The frozen-phonon method consists in explicitly displacing the $i\alpha\mathbf{n}$-th atom for determining the forces (equation (2.73)) acting on all the other atoms. The force, gradient of the total energy, can be calculated analytically through different algorithms based on the Hellman-Feynman theorem. An example of algorithms used in the CRYSTAL code can found in reference [88]. For each atom, the forces are calculated for a given number of points along the cartesian coordinates. In the code CRYSTAL, the value of the calculated forces is used for numerical evaluation of the force constant through a 2- or 3-point formula (equation (2.79) and equation (2.80) respectively):

$$\mathbf{D}^2[V(\mathbf{R}(0))]_{i\alpha\mathbf{n},j\beta\mathbf{m}} \approx \frac{\frac{\partial V(\mathbf{R})}{\partial u_{i\alpha\mathbf{n}}}\Big|_{u_{i\alpha\mathbf{n}}}}{u_{j\beta\mathbf{m}}}; \tag{2.79}$$

$$\mathbf{D}^2[V(\mathbf{R}(0))]_{i\alpha\mathbf{n},j\beta\mathbf{m}} \approx \frac{\frac{\partial V(\mathbf{R})}{\partial u_{i\alpha\mathbf{n}}}\Big|_{u_{i\alpha\mathbf{n}}} - \frac{\partial V(\mathbf{R})}{\partial u_{i\alpha\mathbf{n}}}\Big|_{-u_{i\alpha\mathbf{n}}}}{2u_{j\beta\mathbf{m}}}. \tag{2.80}$$

The frozen-phonon method is generally much easier to implement and require less computational resources than the DFPT; however the displacement can be used to calculate phonons at the Γ point only and other Brillouin Zone points can be sampled only through expanding the primitive cell into a supercell (Section 3.2). This requires to calculate the forces for a much larger number of atoms making the operation extremely time-consuming.

3. Extension of the First-principles Formalism: Systems in Realistic Environments and Point Defects

The methods for the calculation of the electronic structure, outlined in Chapter 2, are very powerful and accurate but appear somewhat limited for studying real systems. The two main limitations consist in the maximum possible size of the system under study, and the restriction to zero temperatures and pressures. Due to the high consumption of computational resources, first-principles calculations can handle systems containing a maximum of few hundreds of atoms. Nonetheless, this number is sufficient for the study of homogeneous systems and is adequate to accurately describe local microscopic phenomena such as the adsorption of molecules on surfaces or point defects, where *ab initio* methods have proven to be a very reliable source of information from an atomistic point of view. On the other hand, even when microscopic phenomena are concerned, real systems are mostly not isolated and interact with the surrounding environment. Furthermore, the zero-temperature limit appears quite severe, considering that the working conditions of materials, important for technological applications, require finite temperatures and pressures.

In this Section, we outline a straightforward and general method able to extend the *ab initio* formalism to the study of macroscopic systems (in particular surfaces and thin films) in thermodynamic equilibrium with a temperature and pressure reservoirs. This method is based on classical statistical mechanics and in the literature is usually referred to as the *ab initio atomistic thermodynamic* approach (Scheffler, Reuter *et al.* [27, 89, 90] and Finnis *et al.* [91, 92, 93]). In Section 3.2, we apply this approach to the study of point defects, where we describe how to estimate their formation energy.

3.1. Ab Initio Thermodynamics

An important step in the study of a material is its characterization after the thermodynamic equilibrium is reached. Laboratory conditions imply, most of the times, constant pressures and temperatures; this make the Gibbs free energy $G(T, p, \{N_j\})$,

where N_j represents the number of particles of type j in the system, to be the relevant thermodynamic potential. In this section, we illustrate how to employ first-principles electronic calculations to estimate G for macroscopic solids.

A key quantity in first-principles calculations is the system potential energy surface (PES) $E_{PES}(\{\mathbf{R_A}\})$, which expresses the variation of the electronic and nuclear repulsion energy with respect to the nuclear coordinates $\{\mathbf{R_A}\}$:

$$E_{PES}(\{\mathbf{R_A}\}) = E_{elec}(\{\mathbf{R_A}\}) + \sum_{A=1}^{M} \sum_{B>A}^{M} \frac{Z_A Z_B}{|\mathbf{R}_A - \mathbf{R}_B|}, \tag{3.1}$$

where $E_{elec}(\{\mathbf{R_A}\})$ is obtained solving the electronic secular equation (2.4a). A connection between first-principles calculations and classical thermodynamics is given by the PES, which gives a first approximation of the system internal energy $U(S, V, \{N_j\})$. The PES includes only the electronic ground-state energy and the Coulomb interaction between point-charges representing the nuclei; yet, even though many contributions to the system internal energy are left out, it represents the leading term in U for a wide range of materials. First-principles calculations explicitly consider just a microscopic portion of real materials and the PES is obtained for this system. However, choosing the system properly, allows us to predict some properties of a whole macroscopic system.

For a general system, the Gibbs free energy can be written as:

$$G(T, p, \{N_j\}) = E_{PES}(\{\mathbf{R_A}\}) + \sum_k F^k(T, V, \{N_j\}) + pV, \tag{3.2}$$

where F^k is the Helmholtz free energy contribution given by the k-th system excitation and p, V are the system pressure and volume, respectively. The form of G in equation (3.2) indicates a weak interaction between the system possible excitations; for the materials in this study, and for the accuracy level of our interest, we consider this approximation to be always valid. Furthermore, we restrict ourself to consider only the electronic, vibrational, rotational and translational excitations, which are most relevant for the p, T ranges pertinent to the studied material. For example, electronic and nuclear excitations generally require energies much larger than $k_B T$ and, therefore, is enough to consider their ground-state only. For the electronic part, the ground-state energy is fully contained in the PES; whereas, for the nuclear part, only the Coulomb interaction is included and all other contributions are neglected.

Despite we are mainly interested in the study of solids, the gas phase has to be also explicitly taken into account, since it represents the temperature and pressure

reservoir the system is in contact with. Of the possible excitations listed above, only vibrational ones are relevant for solids. This allows one to simplify equation (3.2) to:

$$G(T, p, \{N_j\}) = E_{PES}(\{\mathbf{R_A}\}) + F^{vib}(T, V, \{N_j\}) + pV, \qquad \text{for a solid.} \tag{3.3}$$

This equation emphasizes the fact that, within this model, all the temperature-dependent information are given by the calculation of lattice vibrations. For gases, equation (3.2) takes the more general form:

$$\begin{aligned} G(T, p, \{N_j\}) = E_{PES}(\{\mathbf{R_A}\}) + F^{vib}(T, V, \{N_j\}) + \\ F^{rot}(T, V, \{N_j\}) + F^{trans}(T, V, \{N_j\}) + pV, \quad \text{for a gas.} \end{aligned} \tag{3.4}$$

The various contributions to the Helmholtz free energy can be estimated from statistical thermodynamics. Strictly speaking, our system, a solid, is in contact with the atmosphere, which acts as a temperature and pressure (particle) reservoir. The proper statistical ensemble which can represent such situation is the *grand canonical*; however, we can assume that the exchange of particles, between the system and the reservoir, to be so moderate that the system excitations are affected only by the presence of the heat bath. This approximation is reasonable for the systems of our interest and allows one to consider the system microstates to be distributed according to the canonical distribution, which is easier to handle.

We start with finding the vibrational contribution to the Helmholtz free energy, $F^{vib}(T, V, \{N_j\})$ for a solid. For convenience, throughout this discussion, we employ the usual SI units. Let us consider a system with M nuclei, in the harmonic approximation, the Hamiltonian is given by:

$$\hat{H} = \sum_{s=1}^{3M} \hat{h}_s, \tag{3.5}$$

where $\hat{h}_s = -\frac{\hbar^2\nabla^2}{2m_s} + \frac{1}{2}m_s\omega(\mathbf{k})^2 x_s^2$ is the Hamiltonian of the harmonic oscillator representing the s-th mode of vibration. The n-th eigenvalue of $\hat{h}_s$ represent one of the possible energies of the oscillator:

$$E_{s,n}(\mathbf{k}) = (n_{s,\mathbf{k}} + \frac{1}{2})\hbar\omega_s(\mathbf{k}) = E_{s,0}(\mathbf{k}) + n_{s,\mathbf{k}}\hbar\omega_s(\mathbf{k}), \tag{3.6}$$

where $\omega_s(\mathbf{k})$ is the angular frequency of the oscillator s at the point $\mathbf{k}$ of the first

Brillouin zone and $n_{s,\mathbf{k}} = 0, 1, 2, \cdots$. $E_{s,0}(\mathbf{k}) = \frac{1}{2}\hbar\omega_s(\mathbf{k})$ is the zero-point energy of the mode s at the point $\mathbf{k}$. Each microstate of the system has a total energy specified by the vibrational quantum numbers $(n_1, n_2, \cdots, n_s, \cdots, n_{3M}) \equiv \mathbf{n}$ at any $\mathbf{k}$-point:

$$E_{\mathbf{n}} = \sum_{\mathbf{k}} \sum_{s=1}^{3M} (n_{s,\mathbf{k}} + \frac{1}{2})\hbar\omega_s(\mathbf{k}) = \sum_{\mathbf{k}} \sum_{s=1}^{3M} \left(n_{s,\mathbf{k}}\hbar\omega_s(\mathbf{k}) + E_{s,0}(\mathbf{k})\right). \tag{3.7}$$

The system vibrational canonical partition function is therefore:

$$\begin{aligned} Z^{vib} &= \sum_{\mathbf{n}} e^{-\beta E_{\mathbf{n}}} \\ &= \sum_{\mathbf{n}} \exp\left[-\beta\left(\sum_{\mathbf{k}} \sum_{s=1}^{3M} (n_{s,\mathbf{k}} + \frac{1}{2})\hbar\omega_s(\mathbf{k})\right)\right] \\ &= \left[\prod_{\mathbf{k}} \prod_{s=1}^{3M} \exp\left(-\beta E_{s,0}(\mathbf{k})\right)\right] \times \left[\sum_{n_1, n_2, \cdots} \prod_{\mathbf{k}} \prod_{s=1}^{3M} \exp\left(-\beta\hbar\omega_s(\mathbf{k})\right)^{n_{s,\mathbf{k}}}\right], \end{aligned} \tag{3.8}$$

where $\beta = \frac{1}{k_B T}$ and k_B is the Boltzmann constant. The expression can be simplified by noticing that each geometric series $\sum_{n_{s,\mathbf{k}}=1}^{\infty} \exp\left(-\beta\hbar\omega_s(\mathbf{k})\right)^{n_{s,\mathbf{k}}}$ converges to $\left(1 - \exp\left[-\beta\hbar\omega_s(\mathbf{k})\right]\right)^{-1}$; therefore the vibrational partition function can be written as:

$$\begin{aligned} Z^{vib} &= \prod_{\mathbf{k}} \prod_{s=1}^{3M} \frac{e^{-\beta\frac{\hbar\omega_s(\mathbf{k})}{2}}}{1 - e^{-\beta\hbar\omega_s(\mathbf{k})}} \\ &= \prod_{\mathbf{k}} \prod_{s=1}^{3M} \frac{e^{\beta\frac{\hbar\omega_s(\mathbf{k})}{2}}}{e^{\beta\hbar\omega_s(\mathbf{k})} - 1} \\ &= \prod_{\mathbf{k}} \prod_{s=1}^{3M} e^{\beta\frac{\hbar\omega_s(\mathbf{k})}{2}} \langle n_{s,\mathbf{k}} \rangle, \end{aligned} \tag{3.9}$$

where we introduced the Planck distribution:

$$\langle n_{s,\mathbf{k}} \rangle = \frac{1}{\left(e^{\beta\hbar\omega_s(\mathbf{k})} - 1\right)}, \tag{3.10}$$

which gives the average number of phonons s at the point $\mathbf{k}$. From equation (3.9), we can obtain the thermodynamic potentials of our interest through the relations:

$$F^{vib} = -k_B T \ln Z^{vib}; \tag{3.11}$$

$$U^{vib} = k_B T^2 \frac{\partial \ln Z^{vib}}{\partial T}; \tag{3.12}$$

$$S^{vib} = k_B \left(\ln Z^{vib} + \frac{U^{vib}}{k_B T} \right). \tag{3.13}$$

Evaluation of the expressions 3.11-3.13 gives the following explicit form for the vibrational contribution to the Helmholtz free energy [94]:

$$U^{vib} = \sum_{s=1}^{3M} \sum_{\mathbf{k}} \left(\langle n_{s,\mathbf{k}} \rangle + \frac{1}{2} \right) \hbar \omega_s(\mathbf{k}); \tag{3.14}$$

$$S^{vib} = \sum_{s=1}^{3M} \sum_{\mathbf{k}} \left[\frac{\langle n_{s,\mathbf{k}} \rangle}{T} \hbar \omega_s(\mathbf{k}) - k_B \ln \left(1 - e^{-\frac{\hbar \omega_s(\mathbf{k})}{k_B T}} \right) \right]; \tag{3.15}$$

$$F^{vib} = U^{vib} - T S^{vib}. \tag{3.16}$$

With the methods outlines in Section 2.3, it is possible to calculate $\omega_s(\mathbf{k})$ for every s and for a discrete number of points $\mathbf{k}$. Since these calculations are very time consuming, F^{vib} is usually neglected or estimated with simpler models (e.g. the Einstein model which assign the same angular frequency to all the modes). Such approximation is justified by the fact that only energy differences are relevant and, it is assumed, that the vibrational frequencies are not noticeably affected by the introduction of a point defect or a surface. In Part II, we will show that, at high temperatures, F^{vib} gives a considerable contribution to the formation energy of charged defects and highly influences the relative stability between competitive surfaces.

We will treat the gas reservoir according to the ideal gas model, for which is sufficient to consider the partition function of a single molecule:

$$z = z^{vib} z^{rot} z^{trans}. \tag{3.17}$$

We are concerned here with the study of ABO_3 perovskites and, therefore, the gas reservoir will be made of oxygen molecules. The various contributions to the partition function z of a diatomic molecule can be found in several textbooks (for example, reference [95]) and we will list only the resulting values for the vibrational, rotational and translational contributions to the Helmholtz free energy of an ideal

gas made of N_g molecules:

$$F^{vib} = k_B T N_g \ln\left[2\sinh\left(\frac{\hbar\omega_{O_2}}{2k_B T}\right)\right]; \tag{3.18}$$

$$F^{rot} = -k_B T N_g \ln\left(\frac{2I}{\hbar^2} k_B T\right); \tag{3.19}$$

$$F^{trans} = -\frac{3}{2} k_B T N_g \ln\left(2\pi m_{O_2} k_B T\right). \tag{3.20}$$

where ω_{O_2} is the characteristic frequency of the oxygen molecule vibration, I is the molecule momentum of inertia and m_{O_2} is the mass of the oxygen molecule. Since the systems under study are at the thermodynamic equilibrium, it is sufficient to explicitly consider equation (3.16) just for the small portion of the system included in the first-principles calculations.

3.1.1. ABO_3 Perovskite Surface Stability

In this subsection, we apply the method introduced in Section 3.1 to study the stability of ABO_3 perovskite surfaces, following the ideas discussed in reference [96]. In the thermodynamic equilibrium, the internal energy of a system made by bulk ABO_3 perovskite, is a function of the entropy S, the volume V and the number of atomic species in the system: N_A, N_B and N_O. According to the Euler relation, the internal energy and the Gibbs free energy can be written as:

$$U^{bulk} = TS - pV + \sum_i N_i \mu_i; \tag{3.21}$$

$$G^{bulk} = \sum_i N_i \mu_i. \tag{3.22}$$

When a crystalline surface is created, the system internal energy will be dependent also on the surface area A. The generalized force conjugated to A is called the *surface energy*, ω:

$$U^{surf} = TS - pV + \sum_i N_i \mu_i + \omega A; \tag{3.23}$$

$$G^{surf} = \sum_i N_i \mu_i + \omega A. \tag{3.24}$$

The surface energy can be then rewritten as:

$$\omega = \frac{1}{A}\left(G^{surf} - \sum_i N_i \mu_i\right). \tag{3.25}$$

The definition of ω in equation (3.25) is equivalent to the definition of the system grand canonical potential (per unit area). In the literature, the two terms are used interchangeably.

The surface energy can also be defined by a slightly different equation. As an example, let us consider the (001) surface of an ABO_3 perovskite. The surface can be modeled using a *slab* with a certain number of planes, m, and a total area A. For convenience, we use mostly symmetric slabs which have the same chemical composition for both sides (*terminations*). This entails the presence of a mirror plane in the slab central layer and, consequently, an extra symmetry operator which considerably reduces the calculation time. The (001) surface of an ABO_3 perovskite can have two different chemical compositions: AO or BO_2. We will use such chemical formulas also to label the different slabs, since each symmetrical slab can be uniquely associated with the chemical composition of its surface. We consider the surface in thermodynamic equilibrium with ABO_3 bulk and the external atmosphere, which acts, as already stated, as the temperature and pressure reservoir. When the bulk crystal is cleaved, two types of surfaces are formed. In our model, these two surfaces are represented by two slabs: one terminated by planes with chemical composition AO and the other one by planes with composition BO_2, as shown in Figure 3.1. The *cleavage energy* can be calculated as:

$$G_{cleavage}(m) = \frac{1}{4A}\left(G^{unrel}_{\mathrm{AO}}(m) + G^{unrel}_{\mathrm{BO_2}}(m) - N g^{bulk}_{\mathrm{ABO_3}}\right), \tag{3.26}$$

where $G^{unrel}_{\mathrm{XY}}(m)$ is the Gibbs free energy calculated for an unrelaxed slab made of m planes and with termination plane XY, N is the total number of primitive unit cells in the bulk material, before the cleavage, and $g^{bulk}_{\mathrm{ABO_3}}$ is the Gibbs free energy per unit formula of bulk ABO_3. The factor $\frac{1}{4}$ arises from the fact that we model surfaces using two slabs, and each slab possesses two surfaces.

The cleavage energy indicates the energy cost, per unit area, needed to cleave a surface from the bulk material and gives the first contribution to the surface energy. Unrelaxed surfaces are however metastable, since once the surface is formed, the outer atoms will rearrange themselves in response to the reduction of their coordination numbers. The energy gain due to this process is called the *relaxation energy*:

$$G^{\mathrm{XY}}_{relax}(m) = \frac{1}{2A}\left(G^{rel}_{\mathrm{XY}}(m) - G^{unrel}_{\mathrm{XY}}(m)\right), \tag{3.27}$$

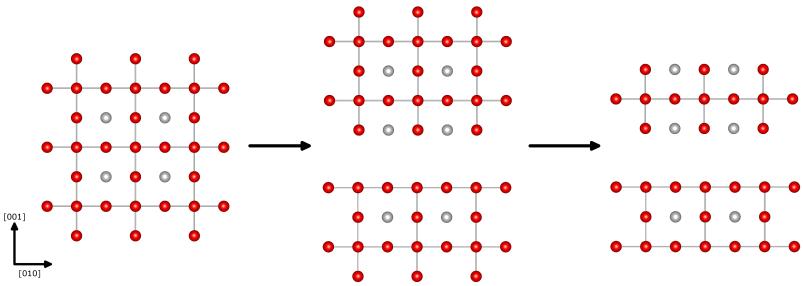

Figure 3.1.: The bulk ABO_3 perovskite (left) is cleaved and two (001) surfaces, with AO (top middle) and BO_2 (bottom middle) terminations, are created. The two surfaces are represented in our model by two symmetric slabs with a finite number of atomic planes (right). The A-type atoms are gray and O are red. Due to the figure prospective, B-type atoms are not visible.

where XY is the kind of termination of the considered slab and G^{rel}_{XY} and G^{unrel}_{XY} are the Gibbs free energy of the relaxed and unrelaxed slabs, respectively. The *surface energy* is obtained combining equation (3.26) with equation (3.27):

$$G^{\mathrm{XY}}_{surface}(m) = G_{cleavage}(m) + G^{\mathrm{XY}}_{relax}(m). \tag{3.28}$$

Equation (3.28) is analogous to equation (3.25) but the former emphasizes the physical process which leads to the surface formation; in particular, the slab relaxation. Using equation (3.24) is equation (3.28), we obtain:

$$\begin{aligned} G^{\mathrm{XY}}_{surface}(m) &= \frac{1}{2A}\left(G^{rel}_{\mathrm{XY}}(m) - \sum_i N_i \mu_i^{unrel}\right) + \frac{\omega^{unrel}_{\mathrm{BO_2}} - \omega^{unrel}_{\mathrm{AO}}}{4}; \\ \omega'_{\mathrm{XY}} &= \frac{1}{2A}\left(G^{rel}_{\mathrm{XY}}(m) - \sum_i N_i \mu_i^{unrel}\right). \end{aligned} \tag{3.29}$$

The superscript '*unrel*' indicates that the quantities are expressed by their value in the unrelaxed system. The extra $\frac{1}{2}$ contribution in the first term, absent in equation (3.25), arises again due to the presence of two surface in the slab. In the literature, both definitions 3.25 and 3.28 are used but we will mainly consider the former.

For a surface, modeled as a XY-terminated symmetric slab with m planes (where m should be sufficiently large so that the two opposite surfaces will not interact and an isolated surface can be well reproduced), equation (3.25) takes the form:

$$\omega_{\mathrm{XY}}(m) = \frac{1}{2A}\left(G^{rel}_{\mathrm{XY}}(m) - \sum_i N_i \mu_i\right). \tag{3.30}$$

Since the surface is in equilibrium with the bulk material, the chemical potential for each atom in the slab assume the same value as in the bulk and, in particular:

$$g^{bulk}_{\mathrm{ABO_3}} = \mu^{bulk}_{\mathrm{ABO_3}} = \mu_{\mathrm{A}} + \mu_{\mathrm{B}} + 3\mu_{\mathrm{O}}. \tag{3.31}$$

Plugging equation (3.31) into equation (3.30) allows one to reduce the number of variables chemical potentials from three to two. For example, after eliminating μ_A, equation (3.30) becomes:

$$\omega_{\mathrm{XY}}(m) = \frac{1}{2A}\left(G^{rel}_{\mathrm{XY}}(m) - N_{\mathrm{A}} g^{bulk}_{\mathrm{ABO_3}} - (N_{\mathrm{B}} - N_{\mathrm{A}})\,\mu_{\mathrm{B}} - (N_{\mathrm{O}} - 3N_{\mathrm{A}})\,\mu_{\mathrm{O}}\right). \tag{3.32}$$

The surface grand canonical potential of equation (3.32) attains a minimum for a system in contact with a temperature and particle reservoir, which in our case is equivalent to a temperature and pressure reservoir, since the chemical potential of an ideal gas is uniquely determined by the values of T and p:

$$\mu_{O_2}(T,p) = \mu^0_{O_2} + k_B T \ln\frac{p}{p^0}. \tag{3.33}$$

The surface grand canonical potential can therefore be employed to study the stability of different surfaces with respect to different environmental conditions (parametrized by the chemical potential values). The values of $G^{rel}_{\mathrm{XY}}(m)$ and $g^{bulk}_{\mathrm{ABO_3}}$ can be obtained directly from first-principles calculations; whereas, the chemical potential values can be obtained as explained in the next subsection.

Range of Allowed Chemical Potentials

The values of the atomic chemical potentials in equation (3.32) depend on the environmental conditions of the system. Except for simple systems, as an ideal gas, it is in general not possible to obtain an explicit relation between chemical potentials and T, p. Therefore, atomic chemical potentials are usually considered as free parameters which can vary in a given limited range. The range can be established from some considerations on the system under study. We denote by $\mu^0_{\mathrm{X}}(T,p)$ the *standard state chemical potential*, that is the chemical potential for the pure species X in the most stable state at given T and p. The first constraint in the chemical potential range, for the atomic species contained in an $\mathrm{ABO_3}$ perovskite, is given

by the fact that the chemical potential $\mu_{\mathrm{X}}(T,p)$ of the species X in the system must be lower than the standard state chemical potential of X. For example, if $\mu_{\mathrm{O}}(T,p) > \mu^0_{\mathrm{O}}(T,p)$, then the oxygen would leave the system and migrate into the atmosphere. Similar considerations affect the range of the metal chemical potentials. Thus the first set of constraints is then given by the relations:

$$\mu_{\mathrm{O}}(T,p) \leq \mu^0_{\mathrm{O}}(T,p); \tag{3.34}$$

$$\mu_{\mathrm{A}}(T,p) \leq \mu^0_{\mathrm{A}}(T,p); \tag{3.35}$$

$$\mu_{\mathrm{B}}(T,p) \leq \mu^0_{\mathrm{B}}(T,p). \tag{3.36}$$

Similar constraints can be introduced to avoid the decomposition of the ABO_3 perovskite into its binary oxides AO and BO_2:

$$\mu_{\mathrm{A}}(T,p) + \mu_{\mathrm{O}}(T,p) \leq \mu^{bulk}_{\mathrm{AO}}(T,p); \tag{3.37}$$

$$\mu_{\mathrm{B}}(T,p) + 2\mu_{\mathrm{O}}(T,p) \leq \mu^{bulk}_{\mathrm{BO_2}}(T,p). \tag{3.38}$$

The standard state chemical potentials (μ^{bulk}_{AO} and $\mu^{bulk}_{\mathrm{BO_2}}$) can be calculated from first-principles, calculating the pure system Gibbs free energy, as outlined in Section 3.1, and using the fact that for pure species, $\mu^{bulk}_{\mathrm{X}}(T,p) = g^{bulk}_{\mathrm{X}}(T,p)$. This approach has an advantage since treats all the terms within the same method and accuracy; however it may be difficult to perform these calculations for certain systems. For example, plane wave-based codes are not very suited to study gas molecules, since the plane wave formalism requires a system with a three-dimensional periodicity. Regarding our computational approach, hybrid functionals are less reliable in calculating properties of metals, due to the presence of the Hartree-Fock exchange which poorly describes the electronic structure near the Fermi energy [97, 98]. Therefore, it is commonly used to take the standard chemical potential values from the available experimental data.

The range in which the chemical potentials, $\mu_{\mathrm{X}}(T,p)$, can vary is defined as:

$$\Delta\mu_{\mathrm{X}}(T,p) \equiv \mu_{\mathrm{X}}(T,p) - \mu^0_{\mathrm{X}}(T,p). \tag{3.39}$$

Equations (3.34)-(3.36) gives an upper-limit to the value of $\Delta\mu_{\mathrm{X}}$:

$$\Delta\mu_{\mathrm{O}}(T,p) \leq 0; \tag{3.40}$$

$$\Delta\mu_{\mathrm{B}}(T,p) \leq 0. \tag{3.41}$$

Using equation (3.31), we can consider only two independent chemical potential ranges, we choose μ_{B} and μ_{O}. From the definition of $\Delta\mu_{\mathrm{X}}$ in equation (3.39) and from the relation (3.31), equation (3.35) becomes:

$$\Delta\mu_{\mathrm{B}}(T,p) + 3\Delta\mu_{\mathrm{O}}(T,p) \geq \Delta_f g^0_{\mathrm{ABO_3}}(T,p), \tag{3.42}$$

where $\Delta_f g^0_{\mathrm{ABO_3}}(T,p) = g^{bulk}_{\mathrm{ABO_3}}(T,p) - \mu^0_{\mathrm{A}}(T,p) - \mu^0_{\mathrm{B}}(T,p) - 3\mu^0_{\mathrm{O}}(T,p)$ is the molar formation energy of the bulk ABO_3 perovskite, defined with respect to the standard state for the pure species. Using the same arguments, equations (3.37) and (3.38) can be written as:

$$\Delta\mu_{\mathrm{B}}(T,p) + 2\Delta\mu_{\mathrm{O}}(T,p) \geq \Delta_f g^0_{\mathrm{ABO_3}}(T,p) - \Delta_f g^0_{\mathrm{AO}}(T,p); \tag{3.43}$$

$$\Delta\mu_{\mathrm{B}}(T,p) + 2\Delta\mu_{\mathrm{O}}(T,p) \leq \Delta_f g^0_{\mathrm{BO_2}}(T,p). \tag{3.44}$$

Equations (3.40) to (3.44) impose the permitted limits for $\Delta\mu_{\mathrm{B}}$ and $\Delta\mu_{\mathrm{O}}$ and allow to calculate the surface grand canonical potential (equation (3.32)) and plot a phase diagram in the $(\Delta\mu_{\mathrm{B}}, \Delta\mu_{\mathrm{O}})$-plane for a fixed value of (p,T). In particular, from these five inequalities one can extract five equations, defining the equilibrium lines in the $(\Delta\mu_{\mathrm{B}}, \Delta\mu_{\mathrm{O}})$-phase diagram:

$$\Delta\mu_{\mathrm{O}}(T,p) = 0; \tag{3.45}$$

$$\Delta\mu_{\mathrm{B}}(T,p) = 0; \tag{3.46}$$

$$\Delta\mu_{\mathrm{B}}(T,p) + 3\Delta\mu_{\mathrm{O}}(T,p) = \Delta_f g^0_{\mathrm{ABO_3}}(T,p); \tag{3.47}$$

$$\Delta\mu_{\mathrm{B}}(T,p) + 2\Delta\mu_{\mathrm{O}}(T,p) = \Delta_f g^0_{\mathrm{ABO_3}}(T,p) - \Delta_f g^0_{\mathrm{AO}}(T,p); \tag{3.48}$$

$$\Delta\mu_{\mathrm{B}}(T,p) + 2\Delta\mu_{\mathrm{O}}(T,p) = \Delta_f g^0_{\mathrm{BO_2}}(T,p). \tag{3.49}$$

We have chosen $\Delta\mu_{\mathrm{B}}$ and $\Delta\mu_{\mathrm{O}}$ as independent variables, but any other chemical potential range can be equivalently used. It is important to recall that this family of equations was obtained from intuitive insight on the chemical system. Such an approach does not take into account all the possible phases that could be formed for given chemical potential ranges, but only those phases, which by inspection, can be

considered the most significant. A scan over the possible configurations and phases can be performed by other techniques, such as Quantum Montecarlo simulations, which usually are much more computationally demanding.

3.2. The Supercell Approach and Calculations of Defective Systems

Finite concentrations of point defects always exits in solids at the thermodynamical equilibrium. Let us consider an isolated system composed of a solid and the surrounding environment, if a single point defect, d, is introduced in the solid, the defect Gibbs energy of formation, $\Delta_{\mathrm{f}}\mathrm{g}_{\mathrm{d}}$ is defined as the Gibbs energy of the process:

$$\text{System with the pristine solid} \rightleftharpoons \text{System with the defective solid.} \tag{3.50}$$

The environment acts as a matter reservoir and has to be taken into account in the formation of extrinsic point defects; i.e. point defects composed by species not existing in the ideal pristine solid. The formation of *intrinsic* point defects does not affect the environment and, therefore, $\Delta_{\mathrm{f}}\mathrm{g}_{\mathrm{d}}$ is given by the Gibbs energy difference between the defective and pristine solids:

$$\Delta_{\mathrm{f}}\mathrm{g}_{\mathrm{d}} = G_{\mathrm{d}} - G_{\mathrm{prist}}, \tag{3.51}$$

where G_{d} and G_{prist} represent the Gibbs free energy of the solid with a point defect d and the Gibbs free energy of the pristine solid, respectively. Throughout this work, we focus mostly on point defects in a very small concentration (*dilute limit*) such that interactions between them are negligible. In such a case, the formation energy of N_{d} point defects d is simply given by $N_{\mathrm{d}}\Delta_{\mathrm{f}}\mathrm{g}_{\mathrm{d}}$, and the Gibbs energy of the system with N_{d} defects is thus given by:

$$G_{\mathrm{d}}(N_{\mathrm{d}}) = G_{\mathrm{prist}} + N_{\mathrm{d}}\Delta_{\mathrm{f}}\mathrm{g}_{\mathrm{d}} + N_{\mathrm{d}}k_B T \ln\left(\frac{N_{\mathrm{d}}}{N - N_{\mathrm{d}}}\right). \tag{3.52}$$

The last term in equation (3.52) gives the contribution to the defective solid Gibbs energy arising from the possible configurations in which N_{d} defects can be distributed over N sites (see, for example, reference [24]). This configurational Gibbs energy is fundamental in ensuring the presence of point defects at the thermodynamic equilibrium.

Equation (3.52) gives explicitly the Gibbs energy of the defective solid as a function of the number of point defects d and, therefore, allows us to define the chemical

potential of the defect d:

$$\mu_{\mathrm{d}} = \left.\frac{\partial G_{\mathrm{d}}(N_{\mathrm{d}})}{\partial N_{\mathrm{d}}}\right|_{T,p,N_1,N_2,\cdots} = \mu_{\mathrm{d}}^0 + k_B T \ln \frac{x_{\mathrm{d}}}{1-x_{\mathrm{d}}}, \tag{3.53}$$

where $\mu_{\mathrm{d}}^0 \equiv \Delta_{\mathrm{f}} g_{\mathrm{d}}$ and $x_{\mathrm{d}} \equiv \frac{N_{\mathrm{d}}}{N}$. For low defect concentrations, $x_{\mathrm{d}} \to 0$, μ_{d} can be written in a simpler form:

$$\mu_{\mathrm{d}} = \mu_{\mathrm{d}}^0 + k_B T \ln x_{\mathrm{d}}. \tag{3.54}$$

The definition of the defect chemical potential, allows one to rewrite equation (3.52) in a very convenient way:

$$G_{\mathrm{d}}(N_{\mathrm{d}}) = N_{\mathrm{prist}}\mu_{\mathrm{prist}} + N_{\mathrm{d}}\mu_{\mathrm{d}}, \tag{3.55}$$

where $\mu_{\mathrm{prist}} = G_{\mathrm{prist}}/N_{\mathrm{prist}}$ is the chemical potential of the solid formula unit. At the thermodynamic equilibrium equation (3.54) has to be equal to zero. These conditions easily allow to find the equilibrium concentration of the defect d, x_{d}^{eq}:

$$x_{\mathrm{d}}^{eq} = e^{-\frac{\mu_{\mathrm{d}}^0}{k_B T}}, \tag{3.56}$$

which defines the mass action law of the reaction 3.50.

Let us consider the formation of an isolated oxygen vacancy in ABO_3 perovskites. One can imagine the formation of an isolated oxygen vacancy as the result of a Frenkel reaction in the oxygen sublattice (*anti-Frenkel* reaction: the anion leaves its lattice site and occupies a crystal interstitial position, $\mathrm{v_i}$) and a successive migration of the interstitial oxygen atom far from the vacancy or to the surface. The anti-Frenkel reaction can be written in the *structure element* or *Kröger-Vink* notation [52] as:

$$\mathrm{O_O} + \mathrm{v_i} \rightleftharpoons \mathrm{v_O} + \mathrm{O_i}, \tag{3.57}$$

or, more concisely in the *building element* notation:

$$\mathrm{Nil} \rightleftharpoons |\mathrm{O}| + \mathrm{O}. \tag{3.58}$$

This latter equation is obtained from equation (3.57) subtracting the pristine structure from both sides; i.e. $|\mathrm{O}| \equiv (\mathrm{v_O} - \mathrm{O_O})$ and $\mathrm{O} \equiv (\mathrm{O_i} - \mathrm{v_i})$. The building element notation is less illustrative than the Kröger-Vink one, but it is the correct one to use in the discussion of the thermodynamic properties. Indeed, from equations (3.51) and (3.52) it is clear that that when we consider the chemical potential

of the defect d, equation (3.54), we actually mean the chemical potential of the building element d. Thus, with chemical potential of an oxygen vacancy v_O, we mean the chemical potential of the building element |O|.

In equations (3.57) and 3.58, we assumed that the oxygen vacancy and interstitial are neutral. However, the formation of point defects is often associated with a charge transfer and the creation of charged defects. ABO_3 pervoskites are characterized by mixed ionic-covalent chemical bonds; therefore in this work we consider oxygen vacancies in three possible charge states: 0 (neutral vacancy, $v_O^{\times}$ or |O|), +1 (singly charged vacancy, $v_O^{\bullet}$ or $|O|^{\bullet}$) and +2 (doubly charged vacancy, $v_O^{\bullet\bullet}$ or $|O|^{\bullet\bullet}$). Conforming to the conventions commonly followed in the first-principles calculations of point defects studies, we use only the Kröger-Vink nomenclature in the rest of this Thesis.

3.2.1. The Supercell Approach

The ideal modeling of a single point defect in a solid would involve the treatment of an infinitely large crystal containing the defective site. Such a model is clearly practically inapplicable and it is also not always necessary, since, sufficiently far from the defect location, the host material is left unperturbed. Point defects in solids can thus be modeled including only a finite number of atoms, which should be, although, large enough to avoid the emergence of unphysical interactions in the system. Defective crystal models can be roughly divided into two categories: molecular-cluster models and model with periodic boundary conditions (PBC). The former considers the defective solid as a large molecule with a defect located in its center; the latter explicitly takes into account the characteristic periodicity of solids applying PBC on a fraction of the host crystal containing the point defect. PBC-based models are widely used nowadays since they avoid the termination problems encountered in molecular-cluster models; furthermore, the use of the translational symmetry, introduced through PBC, allows one to extensively exploit the crystal space group symmetry. The *supercell* approach is perhaps the most used model for describing point defects using PBC [61]. It consists to use a fraction of the host material, the *supercell*, as a new primitive unit cell. The cell parameters defining the supercell are obtained from a linear combination of the original primitive cell unit vectors:

$$\begin{bmatrix} \mathbf{a}' \\ \mathbf{b}' \\ \mathbf{c}' \end{bmatrix} = \begin{bmatrix} c_{11} & c_{12} & c_{13} \\ c_{21} & c_{22} & c_{23} \\ c_{31} & c_{32} & c_{33} \end{bmatrix} \begin{bmatrix} \mathbf{a} \\ \mathbf{b} \\ \mathbf{c} \end{bmatrix} \tag{3.59}$$

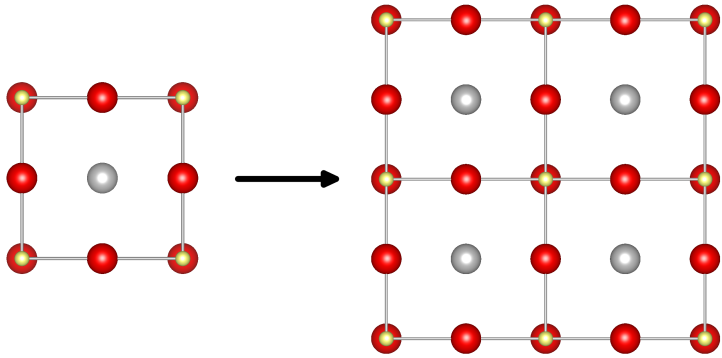

Figure 3.2.: The primitive unit cell of an ideal ABO_3 perovskite (left) is expanded to form a supercell with eight times its volume (right). This supercell is simply obtained setting $\mathbf{a}' = 2\mathbf{a}$, $\mathbf{b}' = 2\mathbf{b}$ and $\mathbf{c}' = 2\mathbf{c}$. The expansion matrix is thus diagonal with $c_{11} = c_{22} = c_{33} = 2$.

where $\mathbf{a}$, $\mathbf{b}$ and $\mathbf{c}$ are the primitive vectors of the original unit cell and $\mathbf{a}'$, $\mathbf{b}'$ and $\mathbf{c}'$ are those of the supercell. The coefficients c_{ij} are positive integers and form the supercell expansion matrix, which describes how the supercell is generated from the original primitive cell. A simple example of supercell expansion is illustrated in Figure 3.2. In this example, the expansion matrix is diagonal and all the coefficients have the same value, equal to two. The generated supercell is therefore obtained repeating the primitive cell twice along each dimension.

The point defect is inserted inside the supercell, which is periodically repeated along the directions of $\mathbf{a}'$, $\mathbf{b}'$ and $\mathbf{c}'$ through PBC. The result is an array of *periodically repeated point defects*. To avoid spurious defect-defect interactions (in this context, generally called *finite-size effects*), which appear between the defect inserted in the supercell and its spurious images in the neighboring supercells, the supercell size should be properly chosen. The defect-defect interactions can have quantum mechanical (overlap of the defect wave functions), elastic, magnetic and/or electrostatic origins. Among these, electrostatic interactions cannot be really canceled increasing the supercell size, due to the very long range nature of the Coulomb forces, and proper correction schemes must be introduced. The other kind of defect-defect interactions can be made sufficiently small just by increasing the supercell to a size which can be usually handled with moderate computational resources. The

correction schemes for the mentioned interactions can be found in reference [17]. Due to the importance given in this work to charged defects, correction schemes for electrostatic interactions between defects will be explicitly described in a later Subsection.

The calculations employing PBC face an old problem of condensed matter physics: the determination of the electrostatic potential of a periodically repeated system. Consider a crystal defined by a primitive unit cell (PUC) periodically repeated an infinite number of times. Let $\rho(\mathbf{r})$ be the charge density of the primitive unit cell; then the crystal electrostatic potential is given by:

$$\phi(\mathbf{r}) = \sum_{\mathbf{R_n}} \int_{PUC} \frac{\rho(\mathbf{r}')}{|\mathbf{r} - \mathbf{r}' + \mathbf{R_n}|}\, d\mathbf{r}', \tag{3.60}$$

where the sum runs over all the (infinite) possible lattice vectors $\mathbf{R_n}$. The direct evaluation of equation (3.60) is very problematic since the result depends on the order of the summation. This problem was solved at the beginning of the twentieth century by Ewald [99], who divided the terms in the sum of equation (3.60) into a short- and long-range parts. The former is quickly convergent in direct space; while the latter in reciprocal space. However, even if the electrostatic potential can be in principle calculated, some spurious terms can be included, depending on the system nature. Makov and Payne [100] summarized the spurious terms that can affect the total energy of a system calculated employing PBC and found the asymptotic behavior of its total energy with respect to the supercell size. Since the electrostatic energy of an infinite system is clearly infinite; much more useful is to consider the electrostatic energy per unit cell (UC), given by:

$$E = \frac{1}{2} \int_{UC} \rho(\mathbf{r})\phi(\mathbf{r})\, d\mathbf{r}, \tag{3.61}$$

where $\phi(\mathbf{r})$ is the system electrostatic potential defined by equation (3.60). In the supercell approach, the UC is the employed supercell, which size, following Makov-Payne treatment, can be characterized by the dimensional parameter L. Equation (3.61) must be compared with the energy of the infinitely aperiodic system, E_0 (which could be, for example, an isolated molecule or a crystal with a single point defect). In case of point defects, equation (3.61) gives the electrostatic energy per UC of a system composed of a periodically repeated array of defects; while E_0 is the electrostatic energy, per UC, of an infinite system with a single point defect.

Makov and Payne demonstrated the asymptotic (for $L \to \infty$) difference between E and E_0 as a function of the lowest non-zero multipole, n, present in the UC. Summarizing their results:

1. If the system is overall neutral and the lowest non-zero multipole term is the octupole ($n = 3$) or higher, then the potential in equation (3.60) easily converges and E is well defined and equal to E_0.

2. If the system is overall neutral and the lowest non-zero multipole term is the quadrupole ($n = 2$), then quadrupole interactions occur between a supercell and its images and therefore: $E(L) = E_0 + O(L^{-5})$.

3. If the system is overall neutral and a dipole is present ($n = 1$), then the energy E is not well defined and its value depends on the supercell shape. However, once the supercell shape is chosen, we have: $E(L) = E_0 + O(L^{-3})$.

4. If the system is not neutral ($n = 0$), the electrostatic energy E diverges and an homogeneous charge background, with density $n_0 = -q/V_{UC}$ (q is the net charge in the supercell and V_{UC} is the supercell volume) must be included in the system. As the supercell size increases, $n_0 \to 0$, and asymptotically: $E(L) = E_0 + O(L^{-1})$.

These considerations suggest that, when a supercell model is employed, the effect of the supercell energy dependence on its size L should be checked. Except for the case of charged systems, the spurious interactions between periodic images are quite short-range and the energy of the supercell converges quickly, even for rather small L.

3.2.2. First-principle Calculation of the Defect Formation Energy

The *defect formation energy* is a quantity which contains important information about the defect chemistry of a solid and can be readily calculated from first-principles. The relation for calculating it was first proposed by Zhang and Northrup [101] and is meant to express equation (3.50) through quantities which can be easily calculated by first-principles with the supercell approach. Considering a single defect d in the charge state q, its formation Gibbs energy, $\Delta_{\mathrm{f}}\mathrm{g}_{(\mathrm{d,q})}$, is given by:

$$\Delta_{\mathrm{f}}\mathrm{g}_{(\mathrm{d,q})} = G_{(\mathrm{d,q})} - G_{\mathrm{prist}} + \sum_i N_i\mu_i + q\mu_{e^-} + E_{\mathrm{corr}}, \tag{3.62}$$

where $G_{(\mathrm{d,q})}$ is the Gibbs free energy calculated for the supercell containing the defect d, and G_{prist} is the Gibbs free energy calculated for a pristine supercell of the same size. N_i is the number of atoms of type i added ($N_i < 0$) or removed ($N_i > 0$) in order to create the defect d and μ_i is the chemical potential of these atoms. Similarly, μ_{e^-} is the chemical potential of the electrons which were added or

removed from the system in order to create the charged defect. All these chemical potentials are not explicitly calculated; this reflects the fact that these species are simply not present in the supercell model describing the defective crystal. Their values can vary in a range estimated from physical insight on the particular system, as outlined in Section 3.1.1. For atomic species, the range is connected to the chemistry of the solid under study; whereas the electron chemical potential is usually simply let varied between the solid valence band maximum and conduction band minimum, even if the presence of the defect d automatically poses some constraints on the value μ_{e^-} can have. Therefore, μ_{e^-} is usually written as:

$$\mu_{e^-} = \epsilon_{VBM} + E_F, \tag{3.63}$$

where ϵ_{VBM} is the value of the valence band maximum and E_F, which ranges between 0 and the band gap, is the position of the Fermi level with respect to the valence band maximum. The value of ϵ_{VBM} can be taken from first-principles calculations as the single-particle eigenvalue of the last occupied electron level. An additional constant is usually added to expression 3.63 in order to align the reference of the defective system with that of the pristine host material. This alignment term arises from the fact that the average electrostatic potential value obtained through the Ewald summation method is conventionally set to zero. This procedure makes the system electrostatic energy (equation (3.61)) independent on the value of the Ewald parameter, but simultaneously causes a constant shift in the system electrostatic potential (equation (3.60)) [102]. This shift does not affect the total energy of a neutral systems but only shifts the eigenvalues; however, in the case of charged systems, *both* the eigenvalues and the total energy are affected [103]. Furthermore, since the constant shift depends on the system charge q, it is often incorporated in the value of ϵ_{VBM}. Equation (2.52) suggests a way to calculate this shift: the ionization energy I can be calculated as the energy difference between a system with $N-1$ electrons and the pristine system with N electrons. The obtained value comprises both the negative value of the valence band maximum energy and the constant shift (due to the fact that we are comparing the total energy of a charged system with that of the neutral system) and can be therefore used, with a change of sign, as ϵ_{VBM} of equation (3.63).

The last term, E_{corr}, takes into account corrections due to the presence of finite-size effects arising from the periodically repeated array of defects generated in the supercell approach. According to the results of Makov and Payne summarized in the last section, in the case of charged defects, the spurious interactions with the defect images are very long-ranged and therefore are always present for any

supercell size. Therefore, if we wish to study charged point defects in the dilute limit, correction terms must be *a posteriori* included in E_{corr}, in such a way that the spurious interactions, arising from the defective system supercell model, cancel out. Two of the most popular of such correction schemes are shortly considered below.

General Ideas Behind Correction Schemes for Charged Point Defects in Supercells

As previously stated, the aim of correction schemes is to cancel the spurious electrostatic interactions arising in the supercell approach. Consider a point defect, d, with charge q and charge density ρ_d; in the dilute limit, the defect interacts only with the host material. Let $\phi_{\mathrm{d,q}}(\mathbf{r})$ be the electrostatic potential of the system composed of the isolated defect d and the host crystal, and let E_{isolated} be its energy. Such a case cannot be realized within the supercell approach, due to the long-range Coulomb interaction; instead, a system composed of a periodic array of defects d in a neutralizing charge background, n_0, has to be used. If the electrostatic potential of such system is denoted as $\phi^{arr}_{\mathrm{d,q}}(\mathbf{r})$ and its energy as E_{periodic}, then the correction energy, E_{corr}, in equation (3.62) is defined as:

$$E_{\mathrm{corr}} \equiv E_{\mathrm{isolated}} - E_{\mathrm{periodic}} = \frac{1}{2}\int_V \left(\phi_{\mathrm{d,q}}(\mathbf{r}) - \phi^{arr}_{\mathrm{d,q}}(\mathbf{r})\right)\rho_d(\mathbf{r})\,d\mathbf{r}, \qquad (3.64)$$

where V is the supercell volume.

In the literature, different correction schemes consider different suitable models for approximate $\phi_{\mathrm{d,q}}(\mathbf{r})$ and $\rho_d(\mathbf{r})$.

Makov-Payne Correction Scheme

In the same paper (ref. [100]) where the multipole interaction between a supercell and its images are considered, Makov and Payne also discussed the spurious interactions, due to the electrostatic interactions between point defects, which arise from the supercell approach. In the most simple case, one can consider a point defect d with a charge q as a point charge in a host crystal which is characterized by a relative dielectric constant ϵ_r. When a supercell is employed, we have a periodic array of such point charges, and a homogeneous charged background is added to ensure the convergence of the electrostatic potential, equation (3.60). The electrostatic energy, of this periodic array of point charges embedded in a host crystal with a compensating charge background, is given by:

$$E_{LG} = -\frac{q^2\alpha}{2\epsilon_r L}, \tag{3.65}$$

where α is the Madelung's constant of the crystalline structure and L represent the defect-defect distance (for simplicity a cubic supercell is considered). The LG subscript was used to indicate that this correction term was already found by Leslie and Gillan in a previous work [104].

Makov and Payne further developed the model of Leslie and Gillan considering, instead of point charges, a more extended, but still very localized, charge distribution. The interaction of such charge distribution with its periodic images give rise to an additional interaction term [100]:

$$E_{MP} = -\frac{2\pi qQ}{3\epsilon_r L^3} + O(L^{-5}), \tag{3.66}$$

where Q is the quadrupole moment of the charge distribution. Therefore, according to Makov and Payne, the energy per UC, for the supercell model of a point defect, differs from the energy of the ideal aperiodic system by $E_{LG} + E_{MP}$:

$$E_{\text{periodic}} = E_{\text{isolated}} - \frac{q^2\alpha}{2\epsilon_r L} - \frac{2\pi qQ}{3\epsilon_r L^3} + O(L^{-5}), \tag{3.67}$$

and the correction term, E_{corr}, of equation (3.62) is thus given by:

$$E_{\text{corr},MP} = \frac{q^2\alpha}{2\epsilon_r L} + \frac{2\pi qQ}{3\epsilon_r L^3} + O(L^{-5}). \tag{3.68}$$

Albeit very intuitive, the Makov-Payne correction scheme not always improve, for realistic point defects, the convergence of the defect formation energy with respect to the supercell size. Therefore, the prefactors of the leading asymptotic terms (L^{-1}, L^{-3}) are often considered as parameters. Their value can be estimated, for example, by calculating the defect formation energy employing supercells of increasing size, and interpolating the obtained points using a function in the form of $AL^{-1} + BL^{-3}$. This procedure also allows one to extrapolate the limiting value ($L \to \infty$) of the defect formation energy. This technique permits to find the defect formation energy at the dilute limit, but is computationally expensive, since requires calculations on many different supercell for the same defect. A better correction scheme would ensure that, already for not a too large L, the obtained value of the defect formation energy converges to the dilute limit. For point defects, which charge density is well localized inside the employed supercell, the correction scheme proposed by Freysoldt, Neugebauer and Van de Walle [105, 106] offers very satisfactory performances [107].

Freysoldt-Neugebauer-Van de Walle Correction Scheme

The Freysoldt-Neugebauer-Van de Walle (FNV) correction scheme relies on a single supercell calculations and no fitted parameters are needed. It considers an ideal system composed of a single point defect d, with charge q and charge density ρ_d, contained in a host crystal with relative dielectric constant ϵ_r. The defective level arising from this point defect is assumed to give rise to a charge density, ρ_d, in general, more delocalized than a point charge, but still fully localized inside a finite fraction of the host material (denoted as UC): $q = \int_{UC} \rho_d(\mathbf{r})\, d\mathbf{r}$. The electrostatic potential of this system in denoted as $\phi_{\mathrm{d,q}}(\mathbf{r})$. If the defect d were neutral, the electrostatic potential would differ, from a charge defect, due to the lack of the strong screening performed by the host crystal electrons. The difference in the electrostatic potentials, for the cases in which the defect d has charge q or has no charge, gives the defect-induced potential:

$$\phi_{\mathrm{q}/0}(\mathbf{r}) = \phi_{\mathrm{d,q}}(\mathbf{r}) - \phi_{\mathrm{d},0}(\mathbf{r}). \tag{3.69}$$

Next, the defect d is considered within the supercell approach. It is advisable to choose a supercell larger than UC, so that the defect charge density does not overlap with that of neighboring supercells. When d is charged, an uniform charge background, $n_0 = -q/V_{UC}$, must be introduced for compensation. Similarly as in equation (3.69), we can consider the difference in the electrostatic potential between an array of defects d with charge q and the same array with non-charged defects. Such quantity is denoted as $\phi^{arr}_{\mathrm{q}/0}(\mathbf{r})$. From the periodic nature of the supercell approach, we can see that $\phi^{arr}_{\mathrm{q}/0}(\mathbf{r})$ is given by the sum:

$$\phi^{arr}_{\mathrm{q}/0}(\mathbf{r}) = \sum_{\mathbf{R_n}} \phi_{\mathrm{q}/0}(\mathbf{r} + \mathbf{R_n}), \tag{3.70}$$

where the sum runs over all the possible supercell lattice vectors $\mathbf{R_n}$.

The artificial electrostatic potential arising from the spurious repetition of the defect d in the supercell approach is then given by $\left(\phi^{arr}_{\mathrm{q}/0}(\mathbf{r}) - \phi_{\mathrm{q}/0}(\mathbf{r})\right)$, and the associated spurious interaction energy per supercell is:

$$E^{inter} = \frac{1}{2} \int_{UC} \left(\rho_d(\mathbf{r}) + n_0\right) \left(\phi^{arr}_{\mathrm{q}/0}(\mathbf{r}) - \phi_{\mathrm{q}/0}(\mathbf{r})\right)\, d\mathbf{r}, \tag{3.71}$$

where the integration is carried over the supercell volume. The last spurious interaction to be taken into account is the interaction of the charge background with the rest of the supercell, which is given by:

$$E^{intra} = \int_{UC} n_0 \phi_{\mathrm{q}/0}(\mathbf{r})\, d\mathbf{r}. \tag{3.72}$$

The quantity $\phi^{arr}_{\mathrm{q}/0}(\mathbf{r})$ can be readily obtained from supercell calculations; on the other hand, the evaluation of $\phi_{\mathrm{q}/0}(\mathbf{r})$ relies on some approximations, since the ideal system with a single point defect cannot be explicitly modeled. $\phi_{\mathrm{q}/0}(\mathbf{r})$ is thus split into a short-range and a long-range contribution:

$$\phi_{\mathrm{q}/0}(\mathbf{r}) = \phi^{sr}_{\mathrm{q}/0}(\mathbf{r}) + \phi^{lr}_{\mathrm{q}/0}(\mathbf{r}). \tag{3.73}$$

For $\mathbf{r} \in UC$, $\phi^{sr}_{\mathrm{q}/0}(\mathbf{r})$ is essentialy equal to $\phi^{arr,sr}_{\mathrm{q}/0}(\mathbf{r})$ plus a constat C, since the dominant part of the defect-defect interaction is given by the long-range part of the electrostatic potential. The constant appears due to the presence of the charge background in the system with a periodical array of defects [104]. The long range part of $\phi_{\mathrm{q}/0}(\mathbf{r})$ is simply taken into account by its limiting value for $|\mathbf{r}| \to \infty$, and $\phi^{lr}_{\mathrm{q}/0}(\mathbf{r})$ is essentially equal to $\phi^{lr}_{\mathrm{d,q}}(\mathbf{r})$ because the neutral defect does not have any appreciable long-range electrostatic potential:

$$\phi^{lr}_{\mathrm{d,q}}(\mathbf{r}) = \int_V \frac{\rho_d(\mathbf{r}')}{\epsilon_r |\mathbf{r} - \mathbf{r}'|}\, d\mathbf{r}', \tag{3.74}$$

where the integration is carried over the volume V which contains the defect charge density ρ_d. Similarly, also for the periodic system $\phi^{arr,lr}_{\mathrm{q}/0}(\mathbf{r}) = \phi^{arr,lr}_{\mathrm{d,q}}(\mathbf{r})$ holds, and the difference $\phi^{arr}_{\mathrm{q}/0}(\mathbf{r}) - \phi_{\mathrm{q}/0}(\mathbf{r})$ in equation (3.71) can be simplified to:

$$\phi^{arr}_{\mathrm{q}/0}(\mathbf{r}) - \phi_{\mathrm{q}/0}(\mathbf{r}) = \phi^{arr,lr}_{\mathrm{d,q}}(\mathbf{r}) - \phi^{lr}_{\mathrm{d,q}}(\mathbf{r}) + C. \tag{3.75}$$

We can then rearrange equations (3.71) and (3.72):

$$E_{\mathrm{corr},FNV} = -\left(E^{inter} + E^{intra}\right) = -E^{lat}_{\mathrm{q}} + q\Delta_{\mathrm{q}/0}, \tag{3.76}$$

where:

$$E^{lat}_{\mathrm{q}} = \int_{UC} \left[\frac{1}{2}\left(\rho_d(\mathbf{r}) + n_0\right)\left(\phi^{arr,lr}_{\mathrm{d,q}}(\mathbf{r}) - \phi^{lr}_{\mathrm{d,q}}(\mathbf{r})\right) + n_0 \phi^{lr}_{\mathrm{d,q}}(\mathbf{r})\right] d\mathbf{r}, \tag{3.77}$$

$$\Delta_{\mathrm{q}/0} = \frac{1}{V_{UC}} \int_{UC} \phi^{sr}_{\mathrm{q}/0}(\mathbf{r})\, d\mathbf{r} = \frac{1}{V_{UC}} \int_{UC} \left(\phi^{arr}_{\mathrm{d,q}}(\mathbf{r}) - \phi^{arr,lr}_{\mathrm{d,q}}(\mathbf{r}) - C\right) d\mathbf{r}. \tag{3.78}$$

All the terms in equations (3.77) and (3.78) can be explicitly calculated:

- The material dielectric constant ϵ_r and the potential $\phi^{arr}_{\mathrm{q}/0}(\mathbf{r})$ can be calculated directly from first-principles.

- The charge density associated with the defect, ρ_d, can be modeled by proper functions. It has been shown that a Gaussian proves to be adequate for those defects with a well localized ρ_d [105].

- Equation (3.70) suggests that the periodic potential $\phi^{arr,lr}_{\mathrm{q}}(\mathbf{r})$ can be calculated as a Fourier series:

$$\phi^{arr,lr}_{\mathrm{q}}(\mathbf{r}) = \frac{1}{V_{UC}} \sum_{\mathbf{G}\neq 0} \tilde{\phi}^{lr}_{\mathrm{d,q}}(\mathbf{G}) e^{i\mathbf{G}\mathbf{r}}, \tag{3.79}$$

  where $\tilde{\phi}^{lr}_{\mathrm{d,q}}(\mathbf{G})$ is the Fourier transformation of the long-range potential of equation (3.74).

- The value of the constant C is obtained assuming that far from the defect, the quantity $\left(\phi^{arr}_{\mathrm{q}/0}(\mathbf{r}) - \phi^{arr,lr}_{\mathrm{q}}(\mathbf{r}) - C\right)$ converges to zero. Therefore, $\phi^{arr}_{\mathrm{q}/0}(\mathbf{r})$ and $\phi^{arr,lr}_{\mathrm{d,q}}(\mathbf{r})$ can be calculated for a set of planes along and perpendicular to the defect-defect direction. In a region around half the defect-defect distance, the value of their difference should converge to a constant C [105].

The pristine bulk can be chosen as the reference system instead of the neutral defect. This has been shown to offer a more reliable approach, since it automatically takes into account the possible shift in the average potentials for defect in different charge states [106]. Using the pristine bulk as the reference and considering a spherical model charge density, ρ_d, the FNV finite-size correction energy can be calculated as [106]:

$$E_{\mathrm{corr},FNV} = -\frac{2\pi}{\epsilon_r V_{UC}} \sum_{\mathbf{G}\neq 0} \frac{\tilde{\rho_d}(\mathbf{G})^2}{|\mathbf{G}|^2} + \frac{1}{\pi\epsilon_r} \int \tilde{\rho_d}(G)^2 \, dG - q\tilde{\phi}^{arr,lr}_{\mathrm{d,q}}(0) - q\Delta_{\mathrm{q/b}}, \tag{3.80}$$

where $\tilde{\phi}^{arr,lr}_{\mathrm{d,q}}(0)$ is the Fourier coefficient of $\phi^{arr,lr}_{\mathrm{d,q}}(\mathbf{r})$ for $\mathbf{G} = 0$, excluded in the first sum of the equation (3.80), and which value is given by:

$$\tilde{\phi}^{arr,lr}_{\mathrm{d,q}}(0) = \frac{2\pi}{V_{UC}\epsilon_r} \frac{\partial^2 \tilde{\rho_d}(G)}{\partial G^2}\bigg|_{G=0}. \tag{3.81}$$

$\Delta_{\mathrm{q/b}}$ is defined similarly to $\Delta_{\mathrm{q}/0}$ in equation (3.78), but with the pristine system, instead of the neutral defect, chosen as reference:

$$\Delta_{\mathrm{q/b}} = \frac{1}{V_{UC}} \int_{UC} \left(\phi^{arr}_{\mathrm{d,q}}(\mathbf{r}) - \phi_{\mathrm{prist}}(\mathbf{r}) - \phi^{arr,lr}_{\mathrm{d,q}}(\mathbf{r}) - C \right) d\mathbf{r}. \tag{3.82}$$

Within this correction scheme, the valence band maximum eigenvalue, in equation (3.63), can be simply taken as the single-particle eigenvalue of the last occupied electron level of the pristine bulk system, as the electrostatic potential alignment term has already been taken into account by $\tilde{\phi}^{arr,lr}_{\mathrm{d,q}}(0)$ and $\Delta_{\mathrm{q/b}}$.

In this work, we model the charge distribution of the defect d in the charge state q, through a 3-dimensional Gaussian function, centered at the origin of the host crystal and normalized to q:

$$\rho_d(\mathbf{r}) = \frac{q}{(\sqrt{2\pi}\sigma)^3} e^{-\frac{r^2}{2\sigma^2}}, \tag{3.83}$$

where σ is the Gaussian standard deviation. The Fourier transform of the charge density is:

$$\tilde{\rho_d}(\mathbf{G}) = q e^{-\frac{G^2\sigma^2}{2}}, \tag{3.84}$$

and the alignment term $\tilde{\phi}^{arr,lr}_{\mathrm{d,q}}(0)$ turns out to be a constant:

$$q\tilde{\phi}^{arr,lr}_{\mathrm{d,q}}(0) = -\frac{2\pi\sigma^2}{V_{UC}\epsilon_r} q. \tag{3.85}$$

The FNV correction scheme has recently been extended to 2D [108] and 1D systems [109]. New difficulties arise in the study of charge defects in low-dimensional systems, with respect to that 3D crystals, due to the presence of two different media (the system and the surrounding vacuum). The introduction of the neutralizing charge background, commonly used in 3D systems, is unclear when a vacuum region is present. The extension of the FNV correction scheme to 2D and 1D systems requires a mapping of the material dielectric constant throughout the system, which makes the correction procedure much more demanding. For this reason, we calculate the formation energy of oxygen vacancy only in bulk $BaZrO_3$; while for surfaces and thin films, we consider only the vibrational contribution to the defect Gibbs energy of formation and we calculate the defect segregation energy without applying any correction scheme.

Part II.

Results

4. Pristine bulk $BaZrO_3$

This Chapter reports the atomic, electronic and vibrational properties of the perfect $BaZrO_3$ crystal and compares the results of our calculations with the values found in the literature. Details about the setup used in the calculations can be found in Appendix A and Appendix B.

4.1. Atomic Structure

$BaZrO_3$ possesses the ideal cubic perovskite structure (Figure 1.1) with space group $Pm\bar{3}m$ (O_h^1, space group number: 221). The cubic primitive cell contains one $BaZrO_3$ formula unit with five atoms and is specified by a single lattice parameter, a, with an approximate length of 4.19 Å (experimental values range between 4.189 Å [110] and 4.192 Å [111]). The 3 primitive lattice vectors **a**, **b** and **c** are orthogonal and we can express them with respect to the cell parameter a and the cartesian unit vectors $\mathbf{e_x}$, $\mathbf{e_y}$, $\mathbf{e_z}$ as:

$$\mathbf{a} = a\mathbf{e_x}, \quad \mathbf{b} = a\mathbf{e_y}, \quad \mathbf{c} = a\mathbf{e_z} \tag{4.1}$$

If not otherwise specified, coordinates will be always given in units of the lattice primitive vectors expressed above.

The crystal structure can be defined by the Wyckoff positions occupied by the atoms in the primitive cell. In $BaZrO_3$, Zr occupies the Wyckoff position a with coordinates $(0, 0, 0)$, Ba occupies position b with coordinates $(1/2, 1/2, 1/2)$ (the cube center) and the three oxygen atoms occupy positions d with coordinates $(1/2, 0, 0)$, $(0, 1/2, 0)$ and $(0, 0, 1/2)$ (Figure 4.1). All the information needed to specify the crystal structure of this compound are summarized in Table 4.1. A comprehensive list of the possible Wyckoff positions for the crystallographic space groups can be found in reference [112].

Our computational setup predicts the cell parameter a with a value of 4.195 Å, a very good agreement with the experimental data [110, 111]. Calculations employing hybrid functionals usually predict well the cell parameter of $BaZrO_3$; compared with the literature, we find that the PBE0 functional, employed in this study, offers the best results [113]. The hybrid functional B3LYP, used in a recent LCAO study,

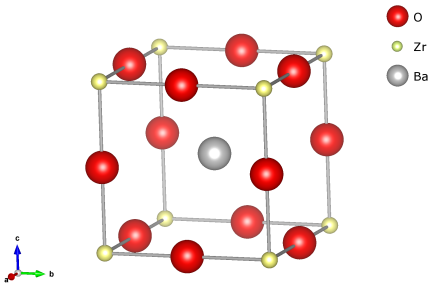

Figure 4.1.: Simple cubic cell of $BaZrO_3$. The unit cell contains Ba in the cube center, Zr in the coordinate origin and 3 O in the middle of the cube edges.

Formula	Space Group	Cell Parameters	Wyckoff Positions
$BaZrO_3$	$Pm\bar{3}m$, O_h^1 (221)	$a = 4.19\,\text{Å}$	Zr(1a), Ba(1b), O(3d)

Table 4.1.: Crystallographic structure of $BaZrO_3$.

slightly overestimates the cell parameter, predicting a value of 4.234 Å [114]. A slight overestimation is also commonly found with the standard DFT-GGA functionals, such as PBE, RPBE and PW91 which also overestimate the bond distances between the cations and oxygens, see Table 4.2.

	LCAO				PW			
	PBE0[a]	PBE[115]	PBE0[113]	B3LYP[114]	PBE[116]	RPBE[116]	PW91[115]	Expt.
a (Å)	4.195	4.242	4.198	4.234	4.235	4.269	4.207	4.189[110], 4.192[111]
d(Zr-O) (Å)	2.098				2.118	2.135		
d(Ba-O) (Å)	2.966				2.995	3.019		
d(O-O) (Å)	2.966				2.995	3.019		
q(Ba)(e)	1.66		1.87	1.81				
q(Zr)(e)	2.35		2.21	2.15				
q(O)(e)	−1.33		−1.36	−1.32				
Z^*(Ba)(e)	2.63	2.58	2.56		2.72	2.73	2.75	
Z^*(Zr)(e)	5.89	6.44	5.88		6.13	6.15	6.05	
$Z^*(O_{\parallel})(e)$	−4.61	−4.99	−4.58		−4.86	−4.91	−4.84	
$Z^*(O_{\perp})(e)$	−1.95	−2.02	−1.94		−1.99	−1.99	−2.05	
ϵ_∞	3.98						4.8	4[117]
ϵ_0	37.70							38.4[118]
E_g(eV)	5.36		5.4	4.79	3.12	3.11		5.33[117]

[a] Present study

Table 4.2.: Selected gound-state properties of $BaZrO_3$ calculated in this work and compared with experiments and other computational studies. The table is divided into two categories according to the type of basis set: localized Gaussian-like functions (LCAO) or plane-waves (PW). Reported properties: cell parameter a; length of the $Zr-O$, $Ba-O$ and $O-O$ bonds, d(-); net Mulliken charges and Born effective charges of Ba, Zr and O, q($elem.$) and Z^*(elem), respectively; electronic, ϵ_∞, and static, ϵ_0, dielectric constants; fundamental band gap, E_g.

4.2. Electronic Structure

$BaZrO_3$ is an insulating material with a wide indirect band gap of 5.33 eV [117]. Ba is an alkaline earth metal with the electronic configuration $[Xe]6s^2$ and Zr is a transition metal with the electronic configuration $[Kr]4d^25s^2$. While forming $BaZrO_3$, both metals formally give their 8 outer electrons to the 3 O atoms, obtaining an oxidation number of +2 (Ba^{2+}) and +4 (Zr^{4+}), respectively. However, the calculated *Mulliken atomic charges* suggests that $BaZrO_3$ is not a purely ionic solid, but is rather characterized by mixed ionic-covalent chemical bonds. The net Mulliken charges are found to be: $1.66\,e$ on Ba, $2.35\,e$ on Zr and $-1.33\,e$ on O; indicating a considerable covalency. In particular, the *Mulliken overlap charge* of 68 me between Zr and O shows that the $Zr-O$ bond possesses a larger covalent character than the $Ba-O$ bond, which has basically no overlap population at all. This fact is confirmed by the electronic density maps plotted in Figure 4.2. These plots were obtained calculating the system electronic density and subtracting from its value the electronic density arising from an analogous system in which each atom maintains its ground-state neutral electronic configuration. The electronic density maps emphasize the charge transfer between atoms upon the crystal formation and give a graphical representation of the chemical bond nature. The maps were plotted

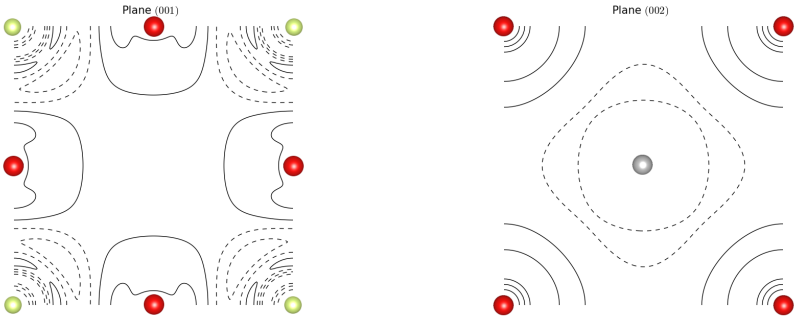

Figure 4.2.: Difference between the calculated electronic density and that arising from corresponding neutral atoms. The full lines indicate values greater than zero, while the dashed lines negative values. The maps were calculated for the (001) plane (left) and (002) plane and the isodensity curves are drawn from -0.05 to $0.05\, e\, {a_0}^{-3}$. An accumulation of the electronic density can be noticed between the Zr and O atoms, indicating the formation of covalent bonds.

for the (001) and (002) atomic planes, containing Zr-O and Ba-O bonds, respectively. In the (001) plane, we note an accumulation of electrons between the O and Zr atoms, indicating the formation of a covalent bond. On the other hand, in the (002) plane, the electron redistribution suggests a strong ionicity and no electron accumulation along the Ba-O direction.

Our computational scheme predicts a fundamental band gap of 5.36 eV, in a very close agreement with the experimental value. Not all the hybrid functionals perform so well; the hybrid functional B3LYP underestimates the band gap by around 0.5 eV [114]. As expected, the DFT-GGA severely underestimate this quantity by more than 2 eV (see Table 4.2). Figure 4.3 shows the calculated band structure and the density of states (DOS). The band structure is plotted along chosen directions joining the high-symmetry points in the first Brillouin Zone, which is reported in Figure 4.4. The valence band maximum is formed predominantly by the O2p orbitals. As predicted by group theory, three O2p orbitals form three electronic bands, which are degenerate at the Γ-point and belong to the small representation Γ_{15}. Similarly, the remaining six O2p orbitals, of the other two oxygen atoms, form two analogous sets, each composed of three electronic bands which are three-fold degenerate at the Γ-point. These three sets, of three electronic bands each, have an overall band width of ≈ 5 eV.

The degeneracy of the Γ_{15} bands is broken if we move from the Γ-point, but

is attained again at the R-point which possesses the same wave vector group as the Γ-point [61, 119]. According to our calculations, the top of the valence band lies at the R-point; while the minimum of the conduction band at the Γ-point. In particular, at the Γ-point, the Γ_{15} bands have an energy $\approx 0.3\,\text{eV}$ lower than at the R-point. The finding of an indirect band gap agrees with experimental observations [118] and is commonly found in electronic structure calculations of related perovskite oxides; such as, $SrTiO_3$ [120], $BaTiO_3$ and $PbTiO_3$ [121]. The bottom of the conduction band is formed mainly by Zr4d orbitals. As known from group theory, the five degenerate d functions are split by the octahedral crystal field into 3-fold degenerate t_{2g} and 2-fold degenerate e_g states. These maintain their characteristic degeneracy at the Γ-point, where they form the Γ'_{25} and Γ_{12} bands, respectively. These bands are quite wide in the reciprocal space ($\approx 7\,\text{eV}$) and overlap with those originated by the Ba5d and O2p atomic orbitals, which form the rest of the conduction bands illustrated in the bottom window in Figure 4.3.

The electronic contribution to the dielectric function, ϵ_∞, was calculated through the Coupled Perturbed Kohn-Sham (CPKS) method, which allows one to solve the Schrödinger equation in the presence of an electric field perturbation [122, 123]. The calculated value of 3.8 is in very good agreement with the experimental value of 4 [117]. The largest contribution to the material dielectric constant, ϵ_0, is, however given by lattice vibrations. This part can be evaluated calculating the Born effective charge tensor,Z^*, which relates the change of the system macroscopic polarization with the displacement of atoms, and the phonon frequencies [124]. In Table 4.2 we compile the Z^* values. Due to the cubic symmetry of the ideal ABO_3 perovskite structure, the local environment of A and B sites has a cubical site symmetry; while for the O ions the site symmetry is tetragonal. Therefore, for the A and B species, Z^* is isotropic and is describe by a single number. For O, Z^* is still a diagonal tensor but with two different values, indicating the change of the polarization induced by a displacement of O atoms either parallel ($Z^*(O_\parallel)$) or perpendicular ($Z^*(O_\perp)$) to the B-O direction. A comparison with the literature shows that the results of the calculations depend both on the choice of functional and, in a minor way, the computational set-up (LCAO or PW, basis set completeness, etc.). The DFT-GGA gives larger dynamic charges for Ba and Zr and lower for O than the PBE0 functional. The large variations of the Born effective charges of Zr and O, with respect to their nominal ionic charges, are commonly found in ABO_3 perovskites and originate from the covalent character of the B-O bond [125].

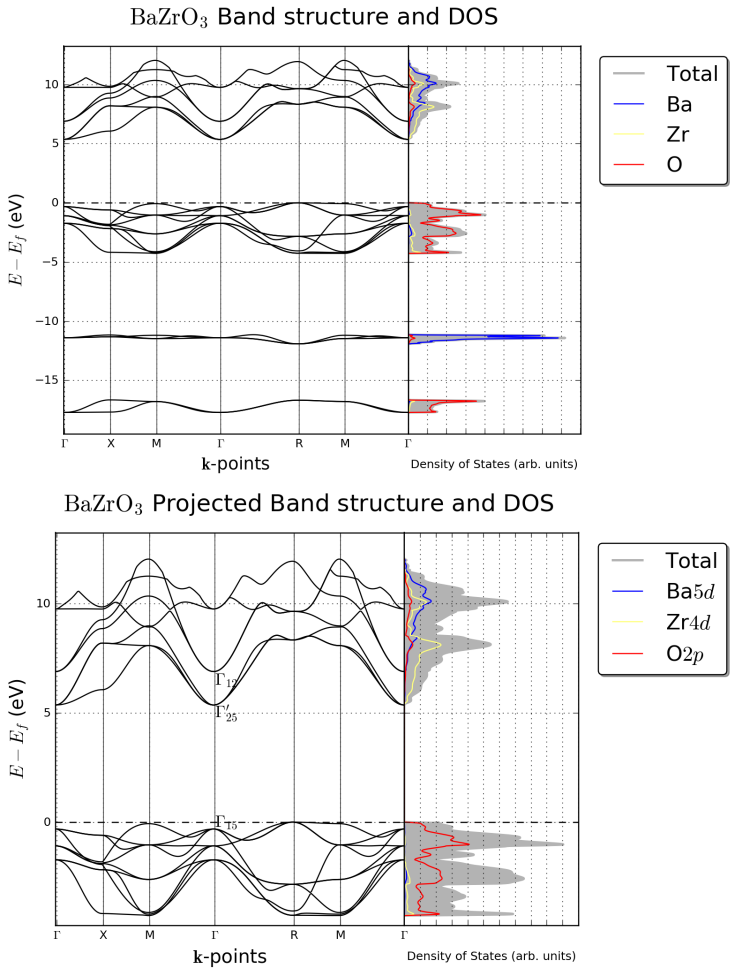

Figure 4.3.: The band structure and density of states of $BaZrO_3$. In the top window, the electronic bands close to the Fermi energy are plotted and the contribution of atoms to the DOS is shown. In the bottom window, only the electronic bands around the valence band maximum and conduction band minimum are plotted. The DOS was projected into a set of atomic orbitals to show their contribution to the bands edges.

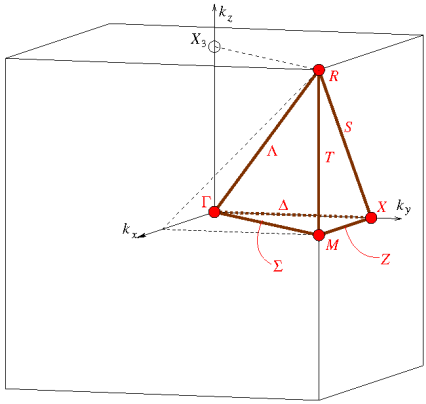

Figure 4.4.: First Brillouin Zone of the $Pm\bar{3}m$ space group. The first Brillouin Zone is simple cubic like the corresponding Bravais Lattice. The picture is taken from the Bilbao Crystallographic Server website [112].

4.3. Vibrational Properties

Table 4.3 reports the phonon frequencies calculated at the Γ-point and a comparison with the experimental values. Cubic ABO_3 perovskites have 5 atoms in the primitive cell from which 15 vibrational branches arise: 3 acoustic and 12 optical. The wave vector group at the Γ-point coincides with the crystal point group, O_h, and the lattice modes representation, $\Gamma_{lat.mod.}$, can be expressed as the direct sum of the irreducible representations of O_h [61]:

$$\Gamma_{lat.mod.} = 4T_{1u} \oplus T_{2u}. \tag{4.2}$$

This result shows that, at the Γ-point, the 15 branches are divided into five 3-fold degenerate groups. The acoustic modes have zero frequencies at the Γ-point and, therefore, only four frequencies, relative to the 12 optical modes, are reported in Table 4.3. Due to the long-range nature of the Coulomb interaction between the vibrating ions, the modes degeneracy is partially lifted and the frequencies of the transverse optical (T. O.) modes differ from those of the longitudinal optical (L. O.) modes [124]. In particular, each of the four groups, in which the optical branches can be subdivided, is characterized by two degenerate T.O. and one L.O. modes. The calculated T.O.-L.O. splitting, reported in Table 4.3, is very large for the O-Zr- O stretch and Zr-O stretch modes. Due to symmetry, no L.O. mode is neither

	Calculated		Exp. [127]
Mode (cm^{-1})	T.O.	L.O.	T.O.
Ba-ZrO_3 stretch	125	145	115
O-Zr- O stretch	219	406	210
Zr-O_3 torsion	220	-	Inactive
Zr-O stretch	511	718	505

Table 4.3.: $BaZrO_3$ phonon frequencies calculated at the Γ-point and comparison with the experimental values. The Zr-O_3 torsion mode is silent due to its T_{2u} symmetry. The longitudinal optical modes (L. O.) cannot be measured experimentally since, due to symmetry, they are not Raman active.

IR nor Raman active and therefore cannot be measured experimentally. However, a very large T.O.-L.O. is typical of ABO_3 perovskites and has been observed in $BaTiO_3$, $SrTiO_3$, $KNbO_3$ and other compounds [126]. Regarding the T.O. modes, the calculated frequencies are in very good agreement with the experimental values. The Zr-O_3 torsion mode has symmetry T_{2u} which is both IR and Raman inactive and, therefore, not measurable.

More information on the material vibrational properties and structural stability can be obtained considering phonons at additional points in the reciprocal space. Figure 4.5 shows the phonon dispersion relations calculated for $BaZrO_3$ along reciprocal space directions connecting the high-symmetry point of the first Brillouin Zone (Figure 4.4). Due to technical reasons, the T.O.-L.O. split could not be calculated in the dispersion relations and a high degeneracy is preserved at the Γ-point. The O-Zr-O stretch and Zr-O_3 torsion modes have very close frequencies, differing only by $1\,cm^{-1}$, resulting in six branches which stick together at the Γ-point around $220\,cm^{-1}$.

ABO_3 perovskites usually have a cubic structure only at relatively high temperatures, but are characterized by a lower symmetry at lower temperatures. $BaZrO_3$ is an exception since it remains cubic, at least down to 2 K [35]. However, some recent first-principles calculations have found imaginary vibrational modes at the R-point, suggesting the possibility of a structural instability [35, 128, 115]. This imaginary mode would cause a tilting of the ZrO_6 octahedra with a reduction of symmetry from cubic to tetragonal. It has been argued that the disagreement between experimental observations and the calculations is due to the stabilization of the soft mode by anharmonic effects [129] or zero-point vibrations [35]. However, further careful calculations have shown that the appearance of the imaginary modes

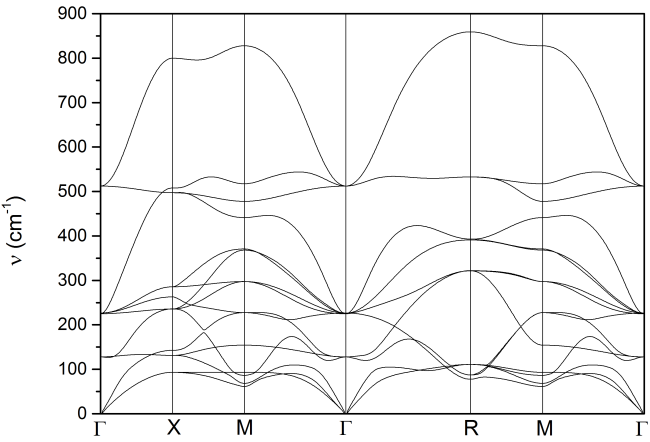

Figure 4.5.: Calculated $BaZrO_3$ phonon dispersion relations. Due to technical reasons, the T.O.-L.O. split was not calculated.

could be related to the functional and pseudo-potentials choice. In particular, LDA calculations predicts imaginary modes at the R- and/or M-point [35, 128]. With the GGA-PW91 functional, the imaginary modes appear when the semicore $5s^2$ electrons are removed from the pseudo-potential [115]; while the PBE and RPBE functionals predict no imaginary mode at all, even considering Ba $5s^2$ electrons in the valence configuration, but, nevertheless, produce a rather soft mode (around $40\,\mathrm{cm}^{-1}$) at the R-point [116]. In our study, the lowest frequency at the R-point is at around $63\,\mathrm{cm}^{-1}$; $\approx 30\,\mathrm{cm}^{-1}$ lower than that found in another PBE0 study [113]. In general, the LDA and GGA overestimate the lattice constant and, therefore, lower vibrational frequencies than those found with hybrid functionals, which well reproduce the geometrical structure, are expected.

Figure 4.6 illustrates the calculated vibrational contributions to some thermodynamic quantities of interest. The left hand side shows the molar vibrational internal energy, u^{vib}, and the molar vibrational entropy, s^{vib}, as a function of the temperature. We can see that the largest part of the vibrational Helmholtz free energy, equation (3.16), is given by the vibrational entropy, since the Ts^{vib} term grows much more rapidly than u^{vib}. At around 350 K, u^{vib} and Ts^{vib} contribute about equally to the free energy, but already at 600 K, the contribution of Ts^{vib} is twice as large than that of u^{vib}.

The right hand side of Figure 4.6 shows a comparison between the calculated

molar constant volume heat capacity, c_v^{vib}, and the measured molar constant pressure heat capacity, c_p. The values of the latter were taken from two different studies. In study [*a*] [130] the authors measured the heat capacity, in the temperature range from room temperature to 1400 K, using a differential scanning calorimeter. By fitting the obtained data, the authors obtained an empirical equation for c_p which we plotted in Figure 4.6. In study [*b*] [131] the authors measured c_p only in a low temperature range between 2 and 300 K. The relation between heat capacities at constant pressure and volume is known from standard thermodynamics books (for example, ref. [132]) and is:

$$c_p = c_v + vT\frac{\alpha^2}{\beta_T}, \tag{4.3}$$

where, v is the system molar volume, α is the volumetric thermal expansion coefficient and β_T is the isothermal compressibility. In solids, the difference between c_p and c_v is usually very small and these quantities can approximately be considered as equal. The paper in reference [36] reports the measured linear expansion coefficient, α_l, and isothermal compressibility for $BaZrO_3$. α_l was calculated by measuring with a dilatometer the material thermal expansion in the temperature range between room temperature and 1000 K; a value of $7.13 \times 10^{-6}\,\mathrm{K}^{-1}$ was found. The β_T was calculated measuring the sound velocities, through an ultrasonic pulse-echo method, at room temperature, and a value of $7.86 \times 10^{-3}\,\mathrm{GPa}^{-1}$ was found. Indeed, the ratio $\frac{\alpha^2}{\beta_T}$ is extremely small for $BaZrO_3$; however, we can notice from Figure 4.6 that $c_p \propto T$ at high temperature. This may be explained from the fact that β_T might decrease with temperature, to the point where the coefficient $\frac{\alpha^2}{\beta_T}v$ differs from zero and anharmonic effects may not be negligible.

We have calculated c_v by computing the phonon frequencies at the Γ-point and using the relation:

$$c_v^{vib} = \left.\frac{\partial u^{vib}}{\partial T}\right|_V. \tag{4.4}$$

As is clear from the right hand side of Figure 4.6, neglect of the rest of the first Brillouin Zone in the calculations, lead to an underestimate of c_v. In paricular, at high temperatures, the calculated c_v is by around $25\,\mathrm{J\,mol^{-1}\,K^{-1}}$ smaller than the classical Dulong-Petit limit of $\approx 125\,\mathrm{J\,mol^{-1}\,K^{-1}}$. At low temperature, the zoomed inset shows that the experimental measured c_p correctly approaches the $\propto T^3$ limit expected in a wide gap insulator, where the only low temperature contributions to c_v and c_p are given by the lattice vibrations.

To better understand how much the calculated thermodynamic properties are af-

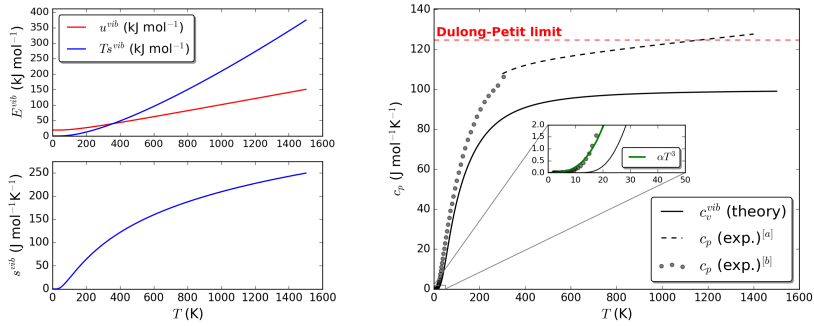

Figure 4.6.: Calculated vibrational contributions to selected thermodynamic quantities of $BaZrO_3$. The calculations took into account only the vibrational frequencies computed at the Γ-point of the first Brillouin Zone. On the upper-left graph, the molar vibrational internal energy, u^{vib}, and the molar vibrational entropy times the absolute temperature, Ts^{vib}, are compared. It is clear that, at high temperatures, the largest part of the vibrational molar Helmholtz free energy, $f^{vib} = u^{vib} - Ts^{vib}$, is given by the entropy term. In the lower-left graph, the molar vibrational entropy is plotted as a function of the temperature. On the right hand side, we report the calculated constant volume molar heat capacity, c_v^{vib}, compared with the measured constant pressure heat capacity, c_p. The experimental data were taken from [*a*]: ref. [130] and [*b*]: ref. [131]. The Dulong-Petit limit, of $3R$ per mole of atom, is also shown. Not surprisingly, the consideration of the phonon frequencies at the Γ-point only, leads to an underestimate of the heat capacity.

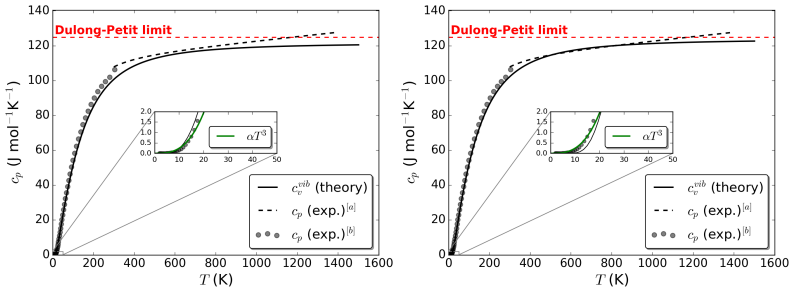

Figure 4.7.: Improvement, over the results shown in Figure 4.6, for the heat capacity of $BaZrO_3$, obtained by including more phonon wave vectors in the calculation. On the left hand side, 8 phonon wave vectors were included in the calculation and on the right hand side the number was increased to 27. Already with 8 wave vectors, the agreement with the experiments is very good and c_v^{vib} correctly approaches the Dulong-Petit limit at high temperatures.

fected by the limited number of sampled phonon wave vectors, we re-calculated c_v^{vib} considering a total of 8 and 27 phonon wave vectors. The results are shown in Figure 4.7. We can see that, already with 8 reciprocal lattice points, the description of c_v is highly improved, both at low temperature, where the computed values agree well with the experimental ones, and at high temperature, where the computed values differ from the expected Dulong-Petit limit only by about $5\,\mathrm{J\,mol^{-1}\,K^{-1}}$. Increasing the total number of reciprocal lattice points to 27 further improves the agreement. These results clearly show the importance of non-Γ-points for the correct description of the thermodynamical properties of crystals. A total number of 8 points in the first Brillouin Zone is probably sufficient for $BaZrO_3$, and the improvement obtained by adding more points may not justify the much larger amount of required computational resources.

In summary, this Chapter shows that our computational set up predicts the main ground-state properties of bulk $BaZrO_3$ with a very good accuracy, which poses a solid basis for the determination of the properties of defective system. The last part of this Chapter has also shown that a correct representation of the thermodynamic properties requires calculations of phonons at more than a single reciprocal lattice point. This, however, may be challenging due to the high computational costs the determination of lattice vibrations require.

5. Oxygen vacancies in bulk $BaZrO_3$

This Chapter deals with the properties of oxygen vacancies in bulk $BaZrO_3$. This defect, one of the most common in oxides, is considered in three different charge states: 0 (neutral oxygen vacancy, $v_O^{\times}$), +1 (singly-charged oxygen vacancy, $v_O^{\bullet}$) and +2 (doubly-charged oxygen vacancy, $v_O^{\bullet\bullet}$). For each of these defect states, we analyze the electronic and atomic structure, and the vibrational properties. In the last Section, the relevant defect formation Gibbs energies are calculated as a function of temperature, with a particular emphasis on the phonon contributions. The vacancy is obtained removing from the simulation cell an oxygen atom and a number of electrons equal to the defect charge state. To have more variational freedom inside the vacant site, the basis set of the removed oxygen atom is kept after the vacancy is formed (a *ghost atom* represent the oxygen vacancy). This allows us to employ orbital population analysis techniques on the vacancy site itself; furthermore, the additional variational freedom leads to a lower total energy. Details on the setup employed in the calculations can be found in Appendix A.

All the calculations employ a supercell model (Section 3.2) and two expansions of the unit cell, denoted as the $2 \times 2 \times 2$ and the $3 \times 3 \times 3$ supercell expansion, are considered. Both expansions are described by a diagonal expansion matrix, in which all the three diagonal elements assume the same value. Such a diagonal expansion is desirable to maintain the symmetry of the original primitive cell. In the $2 \times 2 \times 2$ expansion this value is equal to 2 and this corresponds to supercell cell vectors twice as large as those of the primitive unit cell. The supercell volume is eight times larger than that of the primitive cell and thus contains a total of 40 atoms. Similarly, in the $3 \times 3 \times 3$ expansion, each supercell cell vector is three times larger than the corresponding primitive cell vector. This supercell has twenty-seven times the volume of the primitive cell and contains 135 atoms. To simulate the dilute defect limit, the cell parameter is held fixed in the calculations to the pristine crystal value, but the atoms inside the cell are free to relax to the configuration with the lowest total energy.

We will see that the 40-atom supercell is not large enough to describe correctly the dilute defect limit, even in the absence of charged defects; therefore most of the calculations are performed employing the 135-atom supercell.

5.1. Electronic Structure

The formation of the oxygen vacancy perturbs the host material and affects its atomic and electronic structure. Figure 5.1 shows the electronic density of states (DOS) calculated for the oxygen vacancies in all three possible charge states. One can notice that the defect introduction leads to the creation of a *defective band* within the material band gap, as it is commonly observed for F color centers in ABO_3 perovskites [133, 134]. This new band originates mainly from the overlap between the dangling Zr*d* orbitals of the two Zr ions nearest to the oxygen vacancy (Figure 5.2). The DOS, calculated employing the $2 \times 2 \times 2$ supercell expansion, shows that the defective band has a considerable width of $\approx 0.8\,\text{eV}$, as reported in Table 5.1. This is a clear indication that the employed supercell is not large enough to avoid some spurious overlap between the wave functions of the periodically repeated defects. With a $3 \times 3 \times 3$ supercell expansion, the defective band width is noticeably smaller, $\approx 0.15\,\text{eV}$, indicating a much smaller overlap. However, the width is still not completely zero and a defect-defect interaction, albeit very small, is still present. This stems from the fact that the defective band arises not only from the *d* orbitals of the Zr atoms nearest to the defect, but it also involves, to a lesser extent, also the O 2*p* orbitals, as illustrated in Figure 5.2. As is known, for some defects, even supercells with several hundred atoms are not sufficiently large to avoid these finite-size effects [135]. This may depend both on the defect localization and the particular electronic structure of the host material (e.g. degree of covalency).

Table 5.1 reports also the Mulliken population analysis performed for the vacancy. In particular, it shows that, due to the overlap between the Zr atoms dangling bonds, some fraction of the electron density remains localized within the vacancy in all the charge states. For $v_O^{\times}$ and $v_O^{\bullet}$, the Mulliken charge, $q(v_O)$, is quite considerable: $\approx -1\,e$ and $-0.7\,e$, respectively. For the doubly-charged vacancy, the Mulliken charge within the vacancy is just $-0.2\,e$. In general, the introduction of the defect induces a slight accumulation of electronic density around the two nearest Zr atoms, as can be seen from Figure 5.3. In Figure 5.1, one can see that the defective level is empty for the vacancy in the charge state of +2; while is fully occupied in the other two charge states. This fact may explain why the defective level induced by $v_O^{\bullet\bullet}$ is much more shallow (around 0.2 eV from the conduction band minimum, Table 5.1) than those induced by $v_O^{\times}$ and $v_O^{\bullet}$. Recall that the defective level arises mainly from the overlap between the *d* orbitals of the two Zr atoms siding the vacancy. As a simple model, we can consider these two Zr*d* orbitals to form a hydrogen molecule-like system. In the ground-state configuration, the energy of the molecular orbital (i.e.

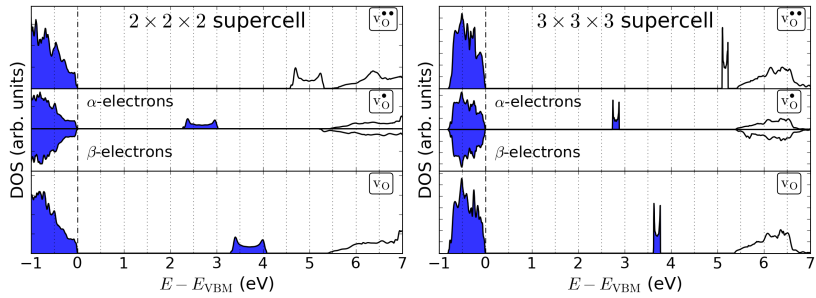

Figure 5.1.: Calculated electronic density of states (DOS) for oxygen vacancies in all the three charge states. The defect induces a defective level (magnified 3 times in the plot) inside the fundamental band gap. The left window shows the DOS calculated employing a $2 \times 2 \times 2$ supercell expansion. The large width of the defective band ($\approx 0.8\,\text{eV}$) is a sign of a strong defect-defect interaction, arising from the supercell method. The width noticeably decreases for a $3 \times 3 \times 3$ expansion (right window). For each system, the DOS is plotted using the valence band maximum (VBM) eigenvalue as the zero energy reference. The blue filling indicates the occupied states.

defective level in our case) is inversely proportional to the Zrd orbitals overlap, S (see, for example, reference [136]). Therefore, as the defective level is fully occupied, a maximization of the overlap S would keep the system (defective site plus host material) total energy as low as possible. In contrast, in the case of $v_O^{\bullet\bullet}$, where the defective level is empty, there is no such effect and the Zr atoms situated next to the vacancy can be brought widely outwards without increasing the system total energy.

Supercell expansion	$2 \times 2 \times 2$			$3 \times 3 \times 3$		
	$v_O^{\times}$	$v_O^{\bullet}$	$v_O^{\bullet\bullet}$	$v_O^{\times}$	$v_O^{\bullet}$	$v_O^{\bullet\bullet}$
$q(v_O)$ (e)	-1.02	-0.71	-0.21	-1.03	-0.71	-0.20
$\Delta\epsilon$ (eV)	1.32	2.40	0.20	1.74	2.50	0.18
$\delta\epsilon$ (eV)	0.77	0.77	0.72	0.15	0.14	0.13

Table 5.1.: Mulliken electronic charge localized within the oxygen vacancy, $q(v_O)$, position of the defective level with respect to the conduction band minimum, $\Delta\epsilon$, and its width, $\delta\epsilon$, calculated for both the $2\times2\times2$ and $3\times3\times3$ supercells. For comparison, the net Mulliken charge calculated for the O ion amounts to $-1.33\,e$.

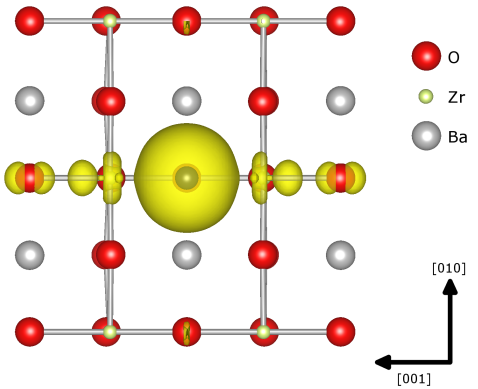

Figure 5.2.: Electronic density projected on the defective level induced by a neutral oxygen vacancy, $v_O^{\times}$, in bulk $BaZrO_3$. One can see that the defective band arises mainly from the overlap between the dangling d orbitals of the two Zr atoms situated at the sides of the oxygen vacancy. To a lesser extension, some of the O p and Ba d orbitals also contribute to the band. The isosurface threshold level is set to -0.005 $e\,{a_0}^{-3}$.

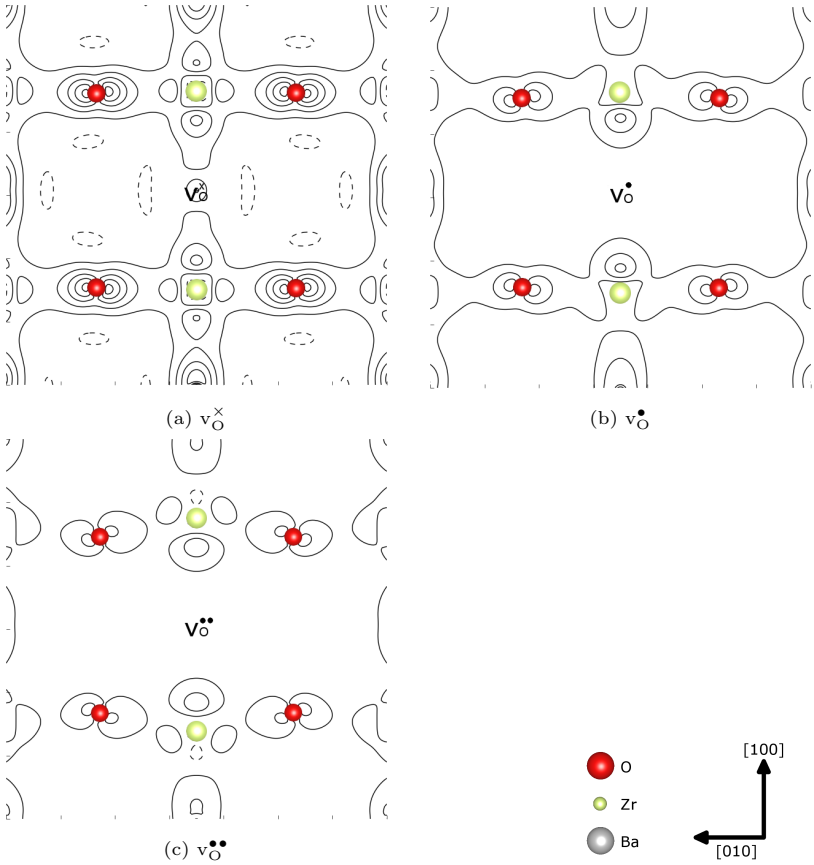

(a) $v_O^{\times}$ (b) $v_O^{\bullet}$

(c) $v_O^{\bullet\bullet}$

Figure 5.3.: Calculated electronic density redistribution induced by oxygen vacancies. The calculations were done for all the three charge states ($v_O^{\times}$, $v_O^{\bullet}$, $v_O^{\bullet\bullet}$) employing the 135-atom supercell. Continuous lines represent an increase in the electronic charge density with respect to the formal ionic electronic configuration; dashed lines represent a depletion thereof. The electronic density localized inside the vacancy is considerable for $v_O^{\times}$, but monotonically decreases as the defect charge state increases.

5.2. Atomic Structure

The lattice distortions around the oxygen vacancy and its neighbors are summarized in Table 5.2. As the Table reports for $v_O^{\times}$, the neighboring atoms tend to slightly relax toward the vacant site; however this displacement is practically negligible. The situation changes when the defect possesses a positive charge. Electrostatic forces cause the positive cations, Zr and Ba, to move outward, while the negative O anions are attracted toward the defect. The displacement magnitude is twice as large for the doubly-charged $v_O^{\bullet\bullet}$ than for the singly-charged $v_O^{\bullet}$. The reason is related to both the larger net charge of $v_O^{\bullet\bullet}$, and, in a minor way, to the occupation of the defective level and the related quantum-mechanical constraints on the lattice relaxation, explained in the previous Section. Clearly, the electrostatic forces have the largest role and for $v_O^{\bullet}$, even if the defective level is fully occupied, its two nearest Zr atoms are still noticeably outward displaced; albeit the displacement magnitude is about half that noticed for $v_O^{\bullet\bullet}$.

The lattice distortion mostly involves only the atoms in the proximity of the defect. As illustrated in Figure 5.4, the rest of the crystalline structure is only slightly affected by this perturbation. In general, the atomic displacements are larger in the 135-atom supercell. This fact confirms the idea that the relatively small 40-atom supercell does not allow a complete atomic relaxation and is, therefore, not large enough to describe the defective system properly.

Table 5.2 shows a monotonic increase in the lattice distortions, as a function of the defect charge state. The ions most affected by the introduction of oxygen vacancies are the two Zr atoms closest to it. These positively charge ions are strongly repulsed by the defect in the charge state +1 or +2. As mentioned above, the displacement is larger, ≈ 0.15 Å, for $v_O^{\bullet\bullet}$, compared with the 0.7 Å for $v_O^{\bullet}$. The situation changes for

Supercell expansion	$2 \times 2 \times 2$			$3 \times 3 \times 3$		
	$v_O^{\times}$	$v_O^{\bullet}$	$v_O^{\bullet\bullet}$	$v_O^{\times}$	$v_O^{\bullet}$	$v_O^{\bullet\bullet}$
Δd(Zr-v_O)/d_0(Zr-O) (%)	-0.24	2.11	4.44	-0.28	3.62	7.46
Δd(Ba-v_O)/d_0(Ba-O) (%)	-0.01	0.61	1.34	-0.01	1.35	3.63
Δd(O-v_O)/d_0(O-O) (%)	-0.92	-3.36	-6.86	-1.13	-3.30	-6.20

Table 5.2.: Calculated structural distortions induced by the oxygen vacancy in three different charge states. Δd(X-v_O)/d_0(X-O) indicates the relative displacement of atom X with respect to the original X-O distance in the pristine system (d_0(X-O)). The displacements are reported only for the nearest neighbors. A negative value indicates an inward relaxation, a positive one an outward relaxation from the oxygen vacancy.

the neutral vacancy $v_O^{\times}$; in this case there are no electrostatic interactions and the two Zr atoms slightly move toward the vacant site. Similarly, the charged defects attract the oxygen ions in the surroundings and, again, the distortion is larger as the charge state increases. The least affected ions are the surrounding Ba, which are unaffected by the presence of the neutral oxygen vacancy but are slightly repelled by the charged defect.

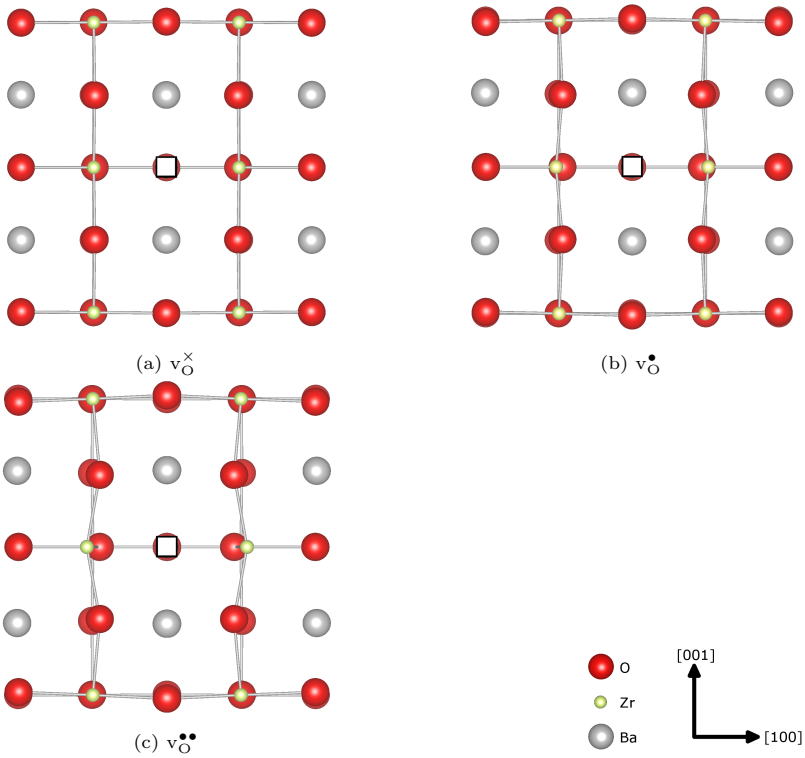

Figure 5.4.: Lattice distortions induced by the oxygen vacancy (represented as a white square). The neutral vacancy brings only minor perturbations. As the charge increases, lattice distortions are more pronounced. The distortions affect mostly the defect nearest neighbors only, and become larger as the defect charge increases.

5.3. Vibrational Properties

Figure 5.5a shows the vibrational density of states (VDOS) calculated for bulk $BaZrO_3$ with three types of oxygen vacancies, $v_O^{\times}$, $v_O^{\bullet}$ and $v_O^{\bullet\bullet}$. The first thing we can notice is that the defect introduces a characteristic new peak in the vibrational frequencies gap situated between 550 and 750 cm^{-1}. The position of the peak is affected by the defect charge state. In particular, for $v_O^{\times}$ the peak appears at 676 cm^{-1}, for $v_O^{\bullet}$ the peak is split into two components at 571 and 707 cm^{-1} and for $v_O^{\bullet\bullet}$ the two peaks appear at 612 and 634 cm^{-1}, respectively. In all these cases, the new vibrational modes arise from the stretching of the Zr-O bonds involving the two Zr atoms surrounding the vacancy and their nearest oxygen atoms. The symmetry of these new vibrational modes belongs to the A_1 irreducible representation of the crystal point group and, therefore, the new peak is, in principle, detectable by IR spectroscopy. These results agree with those found in a related study on $SrTiO_3$, which shown the appearance of a new peak at around 630 cm^{-1}, originated by the Ti-O bond stretching around $v_O^{\times}$ [137].

The oxygen vacancy, produces not only new vibrational modes; the induced structural distortions, illustrated in Section 5.2, affect the whole VDOS. Qualitatively, we expect that, if the vacancy brings some strain on the host crystal, the resulting stiffening of the atomic bonds should lead to an increase in the force constants and thus in the vibrational frequencies. This can be seen in Figure 5.5a for $v_O^{\bullet}$ and $v_O^{\bullet\bullet}$, which, according to our previous discussion, introduce the largest distortions in the host material (see also Figure 5.4). In particular, the effect is larger for $v_O^{\bullet\bullet}$ than $v_O^{\bullet}$, in agreement with the fact that the former defect perturbs the crystal structure much stronger than the latter. This *blue-shift* of the phonon frequencies is particularly important for the calculation of the Gibbs free energy of the defective system, and it especially relevant when the lowest frequencies are affected. Let us consider the crystal vibrational entropy, S^{vib}, expressed by equation (3.15). S^{vib} is plotted in Figure 5.6 as a function of the vibrational frequency of a single mode, ω, for different temperatures T. It can be seen that the contribution of ω to S^{vib} becomes larger and larger as ω decreases. Therefore, this phenomenon affects the whole Gibbs free energy since, as shown in Figure 4.6, the TS^{vib} term is dominant over the internal vibrational energy U^{vib} for temperatures above room temperature.

From Figure 5.5b we see that the vibrational frequencies in the low-frequency range are shifted toward higher values in the presence of the singly-charged, $v_O^{\bullet}$, and especially the doubly-charged, $v_O^{\bullet\bullet}$, oxygen vacancies. This shift causes S^{vib} of these defective systems to decrease with respect to S^{vib} of the pristine material. The calculated value of the lattice vibrational entropy difference between defective and

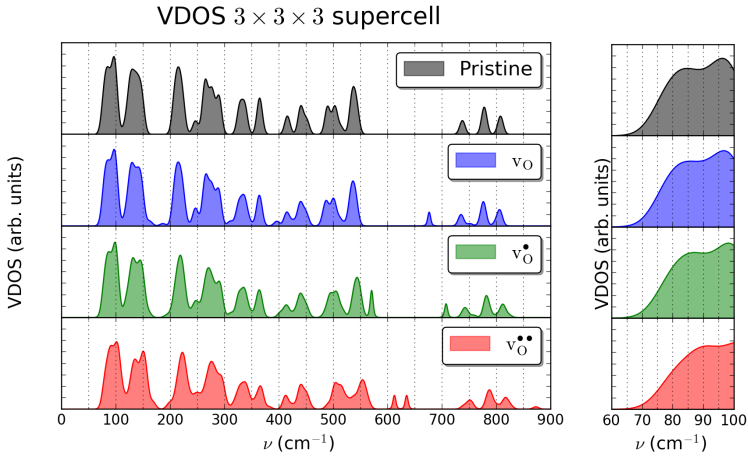

(a) (b)

Figure 5.5.: (a) Vibrational density of states (VDOS) calculated for bulk $BaZrO_3$ with oxygen vacancies in three charge states. The calculations were done employing the 135-atom supercell, which takes into account phonon frequencies at 27 points in the first Brillouin Zone. (b) The VDOS is zoomed in the low-frequency region to emphasize the shift toward higher frequencies introduced by the presence of charged defects. The defect-induced peak has been magnified 5 times.

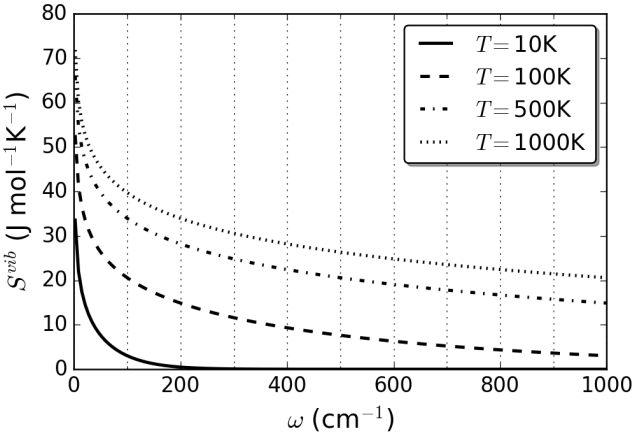

Figure 5.6.: Vibrational entropy, S^{vib} as a function of the vibrational frequency of a single mode, ω, at different temperatures T.

perfect system, $\Delta_\mathrm{f} S^{vib} = S^{vib}_{(\mathrm{v_O},\mathrm{q})} - S^{vib}_{\mathrm{prist}}$ is shown in Figure 5.7 as a function of the temperature. Indeed, we see that $\Delta_\mathrm{f} S^{vib}$ turns out to be negative for each charge state of the oxygen vacancy and becomes even more negative as the charge state, q, increases. On the other hand, the difference in the lattice vibrational enthalpy, $\Delta_\mathrm{f} H^{vib} = H^{vib}_{(\mathrm{v_O},\mathrm{q})} - H^{vib}_{\mathrm{prist}}$, is less affected by the defect charge state and overall contributes only to a few hundreds of meV to the lattice vibrational contribution to the defect Helmholtz free energy, defined as:

$$\Delta_\mathrm{f} F^{vib} = F^{vib}_{(\mathrm{v_O},\mathrm{q})} - F^{vib}_{\mathrm{prist}} = \Delta_\mathrm{f} U^{vib} - T\Delta_\mathrm{f} S^{vib}. \tag{5.1}$$

ΔH^{vib} is indeed equal to the difference in the internal energy, ΔU^{vib}, since we kept in the calculations the volume constant and, thus, differences in enthalpy are equivalent to differences in internal energies. Therefore, at 0 K, ΔH^{vib} gives the difference in the zero-point energy between the defective and pristine system. This value is negative for $\mathrm{v}_\mathrm{O}^{\times}$ and $\mathrm{v}_\mathrm{O}^{\bullet}$, in agreement with the fact that the loss of one oxygen atom decreases the number of vibrational modes in the system by three. On the other hand, the value is positive for $\mathrm{v}_\mathrm{O}^{\bullet\bullet}$ due to the blue shift of the phonon frequencies, which compensates the loss of vibrational modes. The net contribution of $\Delta_\mathrm{f} H^{vib}$ and $\Delta_\mathrm{f} S^{vib}$ to $\Delta_\mathrm{f} F^{vib}$ is shown in Figure 5.7. In the bottom window, the (negative of) oxygen standard chemical potential difference $\Delta\mu_O(T) \equiv$

$1/2\left(\mu^0_{O_2}(T) - E_{0,O_2}\right)$, where E_{0,O_2} represents the oxygen molecule ground-state electronic energy, is plotted for a comparison with $\Delta_\mathrm{f}F^{vib}$. $\Delta\mu_O(T)$ quantifies the molecular thermal energy, given by the vibrational, rotational and translational contributions to the gas phase chemical potential. This quantity corresponds, in general, to the largest contributor in the temperature dependence in the defect Gibbs energy of formation; while, on the other hand, the contribution given by lattice vibration is usually negligible in comparison. In our case, this is true for $\mathrm{v}_\mathrm{O}^\times$, where $\Delta_\mathrm{f}F^{vib}$ is not very large, being around 0.1 eV even at temperatures as high as 1000 K. This was expected since both ΔH^{vib} and $T\Delta S^{vib}$ are not very large and tend to cancel each other out. However, the situation changes when the defect is charged. In agreement with our previous discussion, $\Delta_\mathrm{f}F^{vib}$ increases monotonically with the charge state q, as $\Delta_\mathrm{f}S^{vib}$ monotonically decreases with q. Keeping the temperature of 1000 K as reference, we see that, for $\mathrm{v}_\mathrm{O}^\bullet$, $\Delta_\mathrm{f}F^{vib}$ becomes almost 0.4 eV and for $\mathrm{v}_\mathrm{O}^{\bullet\bullet}$ almost 1 eV. Therefore, for $\mathrm{v}_\mathrm{O}^{\bullet\bullet}$, the contribution of lattice vibrations to the defect formation energy is no longer negligible at high temperatures and has the same magnitude of $\Delta\mu_O(T)$.

Our results differ from those reported in a previous DFT study on oxygen vacancies in bulk $BaZrO_3$, performed by Sundell *et al.* [138]. In this paper, the authors calculated the vibrational contribution to the formation energy of $\mathrm{v}_\mathrm{O}^{\bullet\bullet}$ employing a simple Einstein model, in which the system is described by just one vibrational frequency. The only frequencies explicitly calculated were those relative to the oxygen atoms in proximity of the defect; all the other vibrational frequencies were considered to remain constant upon the insertion of the defect and, therefore, to not contribute at all to $\Delta_\mathrm{f}F^{vib}$. With this simplified model, the authors found a value of $\Delta_\mathrm{f}F^{vib}$ of just around 0.2 eV at 1000 K. The value is much lower than that reported above and negligible in comparison with $\Delta\mu_O(T)$. The disagreement arises from the simplified model employed by Sundell *et al.* which ignores the important contributions to $\Delta_\mathrm{f}F^{vib}$ given by the rest of the phonon spectrum.

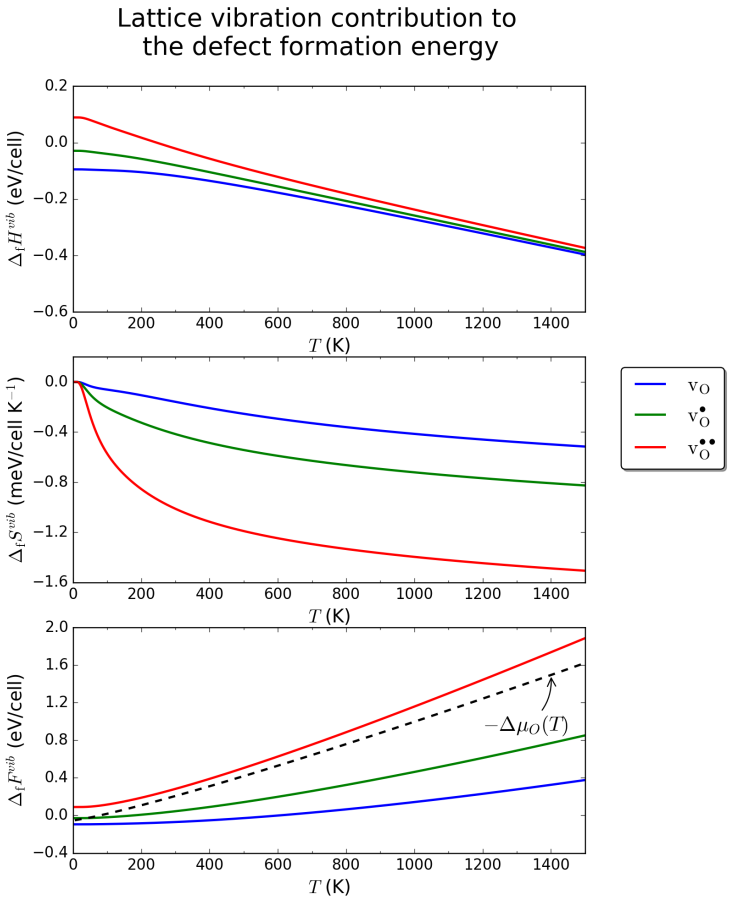

Figure 5.7.: Contribution to the defect formation energy due to lattice vibrations, $\Delta_f F^{vib}$, and its components, $\Delta_f H^{vib} (\equiv \Delta U^{vib})$ and $\Delta_f S^{vib}$, as a function of the temperature T, calculated for oxygen vacancies in three charge states. For comparison, the thermal (non-electronic) part of the oxygen atom chemical potential, $\Delta\mu_O(T)$, is reported. The major contribution to $\Delta_f F^{vib}$ is given by $\Delta_f S^{vib}$, which absolute value increases monotonically, as the charge state increases, due to the blue-shift of low phonon frequencies caused by the defect and described in the main text. Note that, for $v_O^{\bullet\bullet}$, $\Delta_f F^{vib}$ is larger than $|\Delta\mu_O(T)|$.

5.4. Defect Formation Energy

In this Section we report the formation energy calculated for oxygen vacancies in different charge states in bulk $BaZrO_3$. The formation energy is given by equation 3.62 of Section 3.2.2 and, in particular, the valence band maximum has been calculated as explained in Appendix C. Firstly, we consider the formation energy taking into account only the system electronic and zero-point energy. Next, we include the thermal contributions given by lattice vibrations and the gas phase internal degrees of freedom, which allow us to estimate the defect Gibbs free energy of formation at a given temperature. All the calculations were done employing the large 135-atoms supercell in order to reduce as much as possible any type of finite-size error.

The zero-temperature chemical potential of the oxygen atom, μ_O, is evaluated as half the electronic energy of the free O_2 molecule plus half of the zero-point energy. This corresponds to considering an oxygen rich atmosphere as the gas phase reservoir. The ability of the PBE0 functional to correctly describe ground-state properties of the gas-phase O_2 molecule was assessed in previous first-principles studies, *e.g.* ref. [139] and we confirm it in the present work. In particular, the calculated equilibrium distance, d_0, rotational and vibrational temperature, Θ_r and Θ_v, respectively, are in good agreement with the experimental values, as reported in Table 5.3.

The correction energy arising from the presence of finite-size effects in supercells containing charged defects, E_{corr}, was calculated employing the Makov-Payne (MP) and the Freysoldt-Neugebauer-Van de Walle (FNV) correction schemes, discussed in Section 3.2.2. The computed values are reported in Table 5.4. For the MP scheme, we calculated only the Leslie-Gillan term reported in equation (3.65). For the FNV correction scheme, we use a Gaussian function with a standard deviation equal to half the lattice parameter of the $BaZrO_3$ primitive unit cell, which roughly

	PBE0	expt.[140]
d_0 (Å)	1.20	1.21
Θ_r (K)	2.11	2.07
Θ_v (K)	2421	2230

Table 5.3.: Comparison of calculated and measured ground-state properties of the free O_2 molecule. The equilibrium distance, d_0, and the rotational temperature, Θ_r, are in very good agreement with the experimental values. On the other hand the vibrational temperature is overestimated by approximately 8 %. Θ_r and Θ_v indicate the temperatures at which rotational and vibrational excitation, respectively, are not negligible.

	$E_{\mathrm{corr,LG}}$		$E_{\mathrm{corr,FNV}}$	
q/ Supercell Size	+1	+2	+1	+2
$2 \times 2 \times 2$ (eV)	0.064	0.258	0.065	0.225
$3 \times 3 \times 3$ (eV)	0.043	0.172	0.043	0.162
$4 \times 4 \times 4$ (eV)	0.032	0.129	0.032	0.125

Table 5.4.: Energy correction for the finite-size effects due to the introduction of charged defects within a supercell. The correction energy was calculated considering the Leslie-Gillian term of the Makov-Payne correction scheme, $E_{\mathrm{corr,LG}}$, and considering the Freysoldt-Neugebauer-Van de Walle scheme, $E_{\mathrm{corr,FNV}}$. The values are computed for two relevant charge states, q, and for different supercell sizes.

corresponds to the v_O-Zr distance. The employed value for ϵ_r was estimated by first principles as explained in Section 4.2. From Table 5.4 we can notice that both schemes give very similar results. These findings agree with those reported by Komsa *et al.* for $v_O^{\bullet}$ in MgO [107], where the authors found that for this defect the MP and FNV correction schemes give very similar results. This fact suggests that, in bulk $BaZrO_3$ and other oxides, charged oxygen vacancies are characterized by a defective charge density that is mostly localized within the vacancy itself, and therefore a simple point-charge model is good enough for correcting electrostatic finite-size effects. Overall, the correction energy itself is in the range of few tenth of eV, but decreases very slowly with the supercell size, as expected for the long-range electrostatic forces.

We have now all the ingredients to compute the defect formation energy of oxygen vacancies in $BaZrO_3$ in the dilute limit of very low defect concentrations. The results are summarized in Figure 5.8a, which represent the formation energy, calculated at 0 K, as a function of the Fermi level, E_F, defined in equation 3.63. For comparison, Figure 5.8b shows the same quantity calculated at 1000 K. Equation (3.62) indicates that the defect formation energy, $\Delta_{\mathrm{f}}g_{(\mathrm{d,q})}$, depends linearly on the defect charge state, q. Hence, Figures 5.8a and 5.8b show different straight lines with characteristic slopes given by q. The points at which the lines intersect determine the defect *thermodynamic charge transition levels*, $\varepsilon(q/q')$, i.e. the value of E_F for which the defect in the charge state q has the same formation energy as in the charge state q': $\Delta_{\mathrm{f}}g_{(\mathrm{d,q})} = \Delta_{\mathrm{f}}g_{(\mathrm{d,q'})}$. At 0 K, the defect stable over the largest E_F range is $v_O^{\bullet\bullet}$. The charge transition level between $v_O^{\bullet\bullet}$ and $v_O^{\bullet}$, $\varepsilon(+2/+1)$, is situated at $E_F = 3.05$ eV. $v_O^{\bullet}$ is the most stable defect only over a narrow range of E_F, approximately 1 eV, and from $E_F = 4.08$ eV on, the neutral vacancy $v_O^{\times}$ has the lowest formation energy.

The effect of phonons as high temperatures is captured by Figure 5.8b, which shows the same quantities calculated at 1000 K. All the defect formation energies are raised by the positive $\Delta_{\mathrm{f}}F^{vib}$, shown in Figure 5.7, and are lowered by $\Delta\mu_O$, also plotted in Figure 5.7. The effect of $\Delta\mu_O$ is the same for all the charge states and, hence, is enough to consider $\Delta_{\mathrm{f}}F^{vib}$ for describing the differences in the Gibbs free energy of formation of the various oxygen vacancies. $\Delta_{\mathrm{f}}F^{vib}$ attains the largest value for $\mathrm{v}_{\mathrm{O}}^{\bullet\bullet}$ and therefore $\varepsilon(+2/+1)$ decreases to $E_F = 2.36$ eV. Similarly, the larger $\Delta_{\mathrm{f}}F^{vib}$ of $\mathrm{v}_{\mathrm{O}}^{\bullet}$, compared to $\mathrm{v}_{\mathrm{O}}^{\times}$, makes also $\varepsilon(+1/0)$ to decrease to $E_F = 3.76$ eV. The effect of phonons consists hence in stabilizing vacancies in low charge states. Please note that, albeit Figure 5.8a and 5.8b give an immediate qualitative picture of the stability of charged defects, they offer only an approximated view of the defect chemistry of a real solid. In fact, a real material contains different type of defects which influence each other; in particular, the defect concentrations, and thus their chemical potentials, cannot vary independently since they are related by, for example, the relevant mass action laws. Therefore, according to the defect types inside the solid, the electrons chemical potential cannot freely vary between the valence band maximum and conduction band minimum as shown in Figure 5.8a and 5.8b.

The values of the formation energy, calculated at selected temperatures, and the corresponding charge transition levels are reported in Table 5.5. At 0 K, the formation energies of $\mathrm{v}_{\mathrm{O}}^{\times}$, $\mathrm{v}_{\mathrm{O}}^{\bullet}$ and $\mathrm{v}_{\mathrm{O}}^{\bullet\bullet}$ are 7.35, 3.28 and 0.23 eV, respectively. The values are calculated for the Fermi level coinciding with the valence band maximum and in the limit of high oxygen partial pressure. The zero-point energy of the solids and oxygen molecules are included in the value. Compared with the results found by Sundell *et al.* [138] in analogous conditions, the values disagree by around 1 eV. In particular, for $\mathrm{v}_{\mathrm{O}}^{\times}$, Sundell *et al.* report a formation energy of 6.55 eV and of 1.21 eV for $\mathrm{v}_{\mathrm{O}}^{\bullet\bullet}$. The discrepancy could arise from several factors. In particular, from the fact that the calculations employed the GGA functional of Perdew and Wang which is known to underestimate the material bang gap (the authors found indeed a value of only 3 eV). The incorrect description of this gap can lead to a shift of the band edges and, therefore, of the electron chemical potential, which, in turn, determines the formation energy of charged defects.

Table 5.5 quantifies also the effect of the temperature on the defect Gibbs free energy and the charge transition levels. It is important to underline the fact that our calculations assume a temperature-independent bang gap, which is generally not true for perovskite materials, where the band gap can change by tenth of eV as the temperature is increased by few hundreds of K [141].

In conclusion, we have shown how oxygen vacancies affect bulk $BaZrO_3$ prop-

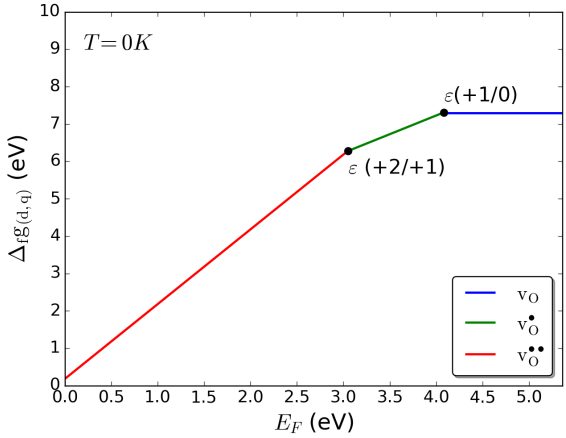

(a)

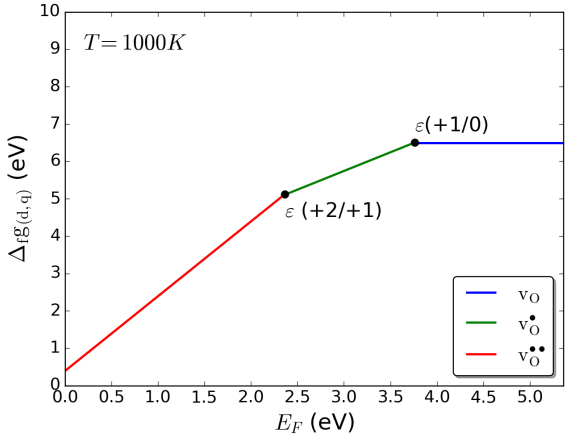

(b)

Figure 5.8.: (a) Defect Gibbs free energy of formation, $\Delta_{fg_{(d,q)}}$, calculated at 0 K for oxygen vacancies in bulk $BaZrO_3$ as a function of the Fermi level, E_F. (b) Same quantity calculated at 1000 K. Lattice vibrations increase the formation energy of the oxygen vacancies in all charge states and shift the thermodynamic charge transition levels toward lower E_F, thus decreasing the electron chemical potential range in which $v_O^{\bullet\bullet}$ is the most stable.

	$\Delta_{\mathrm{f}}g_{(\mathrm{d,q})}$ (eV)			$\varepsilon(q/q')$ (eV)	
T (K)	$v_O^{\times}$	$v_O^{\bullet}$	$v_O^{\bullet\bullet}$	$\varepsilon(+2/+1)$	$\varepsilon(+1/0)$
0	7.35	3.28	0.23	3.05	4.08
300	7.07	3.11	0.30	2.82	3.96
600	6.87	3.00	0.38	2.62	3.88
1000	6.49	2.74	0.39	2.36	3.76

Table 5.5.: Calculated Gibbs free energy of formation, $\Delta_{\mathrm{f}}g_{(\mathrm{d,q})}$, and thermodynamic charge transition levels, $\varepsilon(q/q')$, for oxygen vacancies in bulk $BaZrO_3$. The values were calculated at the high oxygen partial pressure limit and for an electron chemical potential value equal to the valence band maximum. The temperature-dependence is obtained including the contributions of lattice vibrations and molecular translation, rotations and vibrations.

erties. In particular, vacancies induce a distinguishable electronic level inside the fundamental band gap and IR-active new vibrations. The defective is quite well localized inside a $3 \times 3 \times 3$ supercell and electrostatic finite-size effects can be corrected equally well with either the Makov-Payne or the Freysoldt-Neugebaur-Van de Walle scheme. At 0 K, the oxygen vacancy formation energy decreases with the charge state; in particular, the charge transition level $\varepsilon(+2/+1)$ is located at 3.05 eV and $\varepsilon(+1/+0)$ at 4.08 eV. Furthermore, an oxygen vacancy produces a structural stress on the surrounding lattice, which strongly depends on the defect charge state. In particular, as the stress is caused mainly by electrostatic forces, the crystal distortion increases with the defect charge. As a consequence of the defect-induced stress field, the phonon frequencies increase. This blue-shift affects, in particular, the lattice vibrational entropy difference,$\Delta_{\mathrm{f}}S^{vib}$, which becomes negative. The effect is that the vibrational contribution to the defect formation energy, $\Delta_{\mathrm{f}}F^{vib}$, rapidly increases with the temperature. For charged oxygen vacancies and, especially for $v_O^{\bullet\bullet}$, $\Delta_{\mathrm{f}}F^{vib}$ is not negligible and its value is comparable with the temperature-dependent term in the oxygen chemical potential. The general effect of lattice vibrations on the vacancy Gibbs energy of formation is to lower the thermodynamic charge transition levels as the temperature is raised, increasing, therefore, the stability range of vacancies with a low charge.

6. Two Dimensional Defects in ABO_3 Perovskites: The $BaZrO_3$ (001) Surface

ABO_3 perovskite surfaces are important for many technological applications such as the growth of high-T_C superconductors, catalysis and electrochemistry. In particular, the promising applications of $BaZrO_3$, as electrolyte material in protonic ceramic fuel cells, makes the study of its surfaces a first important step in understanding the structure and behavior of interfaces with other phases and materials. Several first-principles and experimental studies have been carried out on $BaZrO_3$ surfaces, especially on the (001) which is supposed to be the most stable. Indeed, the (001) surface was directly observed on $BaZrO_3$ nanoparticles through transmission electron microscopy and X-ray diffraction measurements [142, 143]. Furthermore, the first-principles studies in reference [144] and reference [145], have shown that the (001) surface is more stable than other low-index surfaces.

The (001) surface of ABO_3 perovskites has two possible termination planes: the chemical composition of the outer monolayer can either be AO or BO_2. Experimentally, it is not easy to discern which chemical composition of the surface termination is actually present, but with the method outlined in Section 3.1.1 it is possible to estimate that through the use of first-principles calculations. The author of the paper in reference [146] employed this method at $T = 0\,\mathrm{K}$ and predicted that the BaO termination of $BaZrO_3$ (001) surfaces is the most stable. In this Chapter, we calculate the atomic and electronic properties of the $BaZrO_3$ (001) surface. Surfaces are modeled employing the symmetrical non-stoichiometric slabs introduced in Section 3.1.1. These slabs contain fifteen atomic planes, which can be considered thick enough for modeling the material surface, since we found that a further increment of the number of atomic plane in the slab changes the system energy by less than 0.001 eV per formula unit. The slabs with the two possible terminations are illustrated in Figure 6.1. The cell parameter is fixed to the bulk value but all the ions are free to relax to reach a potential energy surface local minimum.

In addition, we extend the study [146] to finite temperatures, as described in Section 3.1, and show how the termination stability is affected by the temperature. Finally, we consider the electronic properties of the oxygen vacancies $\mathrm{v}_{\mathrm{O}}^{\times}$ and $\mathrm{v}_{\mathrm{O}}^{\bullet\bullet}$

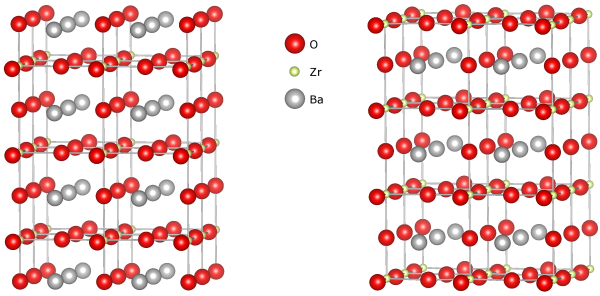

Figure 6.1.: Slab models employed for modeling the (001) surface of $BaZrO_3$. Both the BaO (left) and ZrO_2 (right) terminations are represented.

on the ZrO_2-terminated surface and we calculate the defect *segregation energy*. For $v_O^{\bullet\bullet}$, which plays the most significant role in electrochemical applications of $BaZrO_3$, we also consider the lattice vibration contributions to the defect segregation energy. Due to the large computational costs involved in the study of defective systems, the oxygen vacancies are considered employing thinner slabs containing seven atomic planes.

6.1. The Clean (001) Surface

As a planar crystalline surface is created, the loss of coordination number affecting the surface atoms leads to a rearrangement of the electron-charge density and the ions. The structural relaxation affects mostly the ions on the outer planes. In ABO_3 perovskites, a surface *rumpling*, s, is commonly observed, which is measured by the relative displacement of the surface oxygen atoms with respect to their nearest surface metal plane. Other parameters which can describe the system relaxation are the *interplanar distances* between the metal ions in the i-th and j-th planes, Δd_{ij}, where the index counting starts from the surface (1 = surface metal plane, 2 = subsurface metal plane, and so on).

Table 6.1 reports the surface rumpling and interplanar distances calculated for the two possible terminations of the $BaZrO_3$ (001) surface. The interplanar distances are reported only for the outermost metal planes, since their value rapidly decrease as we go deeper inside the slab. Indeed, from the Table 6.1 we can see that, while Δd_{12} equals 10 % of the original Ba-Zr length, Δd_{23} is already half that value. As mentioned above, the breaking of atomic bonds, that follows the

BaO termination			ZrO_2 termination		
s (%)	Δd_{12} (Å)	Δd_{23} (Å)	s	Δd_{12} (Å)	Δd_{23} (Å)
3.62	1.88(-10.4)	2.19(4.26)	1.31	1.88(-10.4)	2.22(5.74)

Table 6.1.: Surface rumpling, s and the interplanar distances between the uppermost metal layers, Δd_{12}, Δd_{23} . The rumpling is reported as relative percentile with respect to the calculated bulk lattice constant of 4.195 (Å). The interplanar distances are reported in Å; while the values in brackets refer to the relative percentile value with respect the Zr-Ba distance along the [001]-direction in bulk $BaZrO_3$. A positive value indicates an expansion, while a negative one a contraction of the distance.

surface creation, generates an electron-density redistribution between the two outermost layers, which is illustrated in Figure 6.2. In particular, the electron-density redistribution increases the degree of covalency of the Zr-O surface bonds. As a consequence, the bonds are strengthened also between the surface and subsurface planes; the Ba-Zr distances are reduced and the relative interplanar distances Δd_{12} assume a negative value. The attraction of the metal subsurface toward the surface increases, as a consequence, the interplanar distance Δd_{23}. These results qualitatively agree with the other first-principles studies of the $BaZrO_3$ (001) surface found in the literature [144, 145, 146, 147].

Table 6.1 also shows that the surface rumpling, s, is noticeably smaller in ZrO_2-terminated surfaces than in BaO-terminated ones. This could be explained by two phenomena. Firstly, the electron-density redistribution at the surface, shown in Figure 6.2, strengthen the covalent Zr-O bonds more than the ionic Ba-O ones, leading to a smaller rumpling in ZrO_2-terminated surfaces. The increase in the bond covalency can be quantified by the Mulliken overlap charges, which assume a value of 92 me for the Zr-O surface bond (68 me in the bulk) and a value of 12 me for the Ba-O surface bonds (approximately 0 in the bulk). The second explanation is related to the electronic structure of bulk $BaZrO_3$ reported in Section 4.2. $BaZrO_3$ valence band maximum originates mainly from the overlap between oxygen 2p orbitals, but there is some mixing with Zr4d and 4p orbitals, especially for the bands just below the valence band maximum. In comparison, the mixing with Ba5d orbitals is practically negligible (Figure 4.3). The surface rumpling causes the metal-oxygen bond length to increase, reducing the overlap between the atomic orbitals which compose the valence band maximum. Therefore, a large rumpling on the ZrO_2-terminated surface would increase the system total energy considerably more strongly than on the BaO surface.

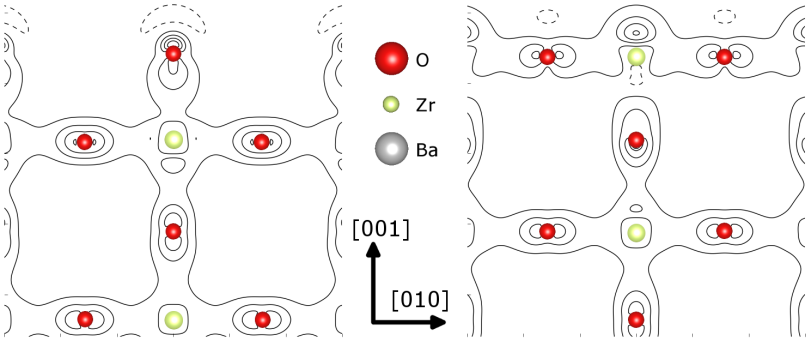

Figure 6.2.: Electronic density redistribution affecting the (001) surfaces of $BaZrO_3$. Both the BaO (left) and ZrO_2 (right) terminations are considered. The plot represents the electron-charge density difference between the slab model and the ideal ionic configuration of bulk $BaZrO_3$. Full lines indicate an accumulation of charge density and dashed lines a depletion thereof. It is clear that electron redistribute from the surface toward the subsurface.

A consequence of the phenomena originating from the surface rumpling is the increase of the valence band maximum energy for ZrO_2-terminated surfaces with respect to the bulk material. The surface electronic DOS is illustrated in Figure 6.3 for both possible terminations. In Figure 6.3, the DOS is also projected on the atoms forming the surface, subsurface and other inner planes of the slab (in the picture, with the designation 'bulk' we indicate the slab central plane). For ZrO_2-terminated surfaces, the DOS projected over the surface plane shows an increase of the oxygen orbitals energy which raise the valence band maximum. The effect stems from the mixing between O2*p* and Zr4*d* orbitals outlined above and is not present in inner planes or for BaO-terminated surfaces. It is a typical *surface state* observed in ABO_3 perovskites, which decreases the band gap of the BO_2-terminated (001) surfaces [147, 148]. In the case of $BaZrO_3$, the calculated band gap for ZrO_2-terminated (001) surfaces is 4.54 eV, considerably lower than that calculated for BaO-terminated surfaces (5.33 eV) and for the bulk material (5.36 eV).

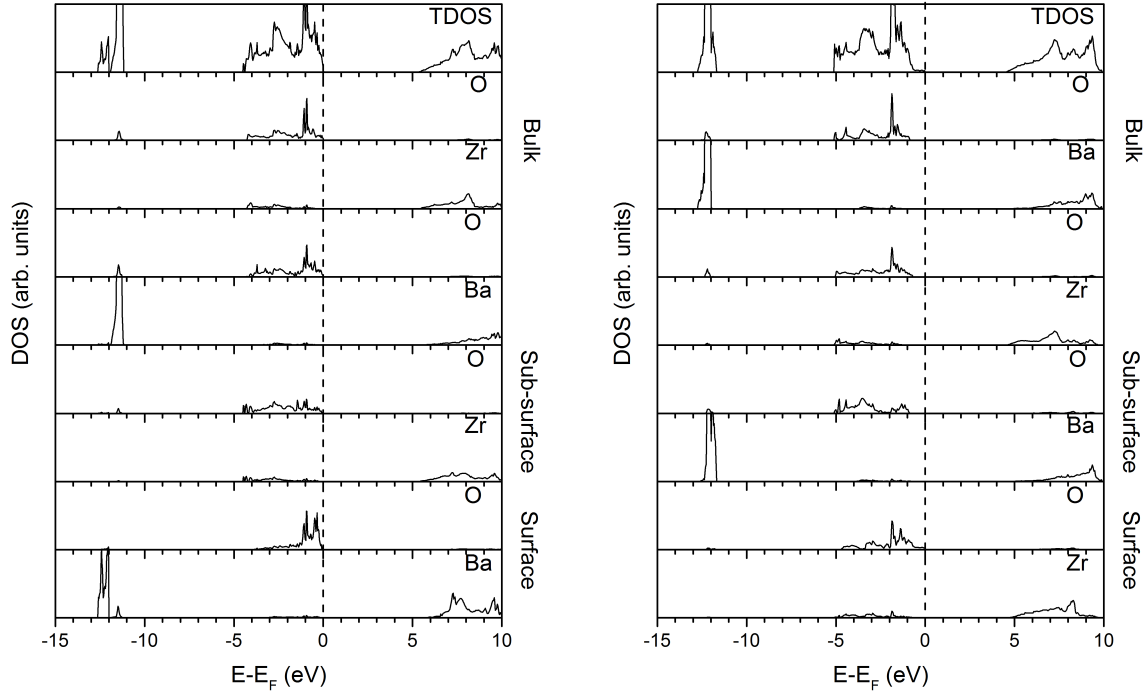

(a) BaO termination

(b) ZrO_2 termination

Figure 6.3.: Total electronic DOS calculated for the $BaZrO_3$ (001) surface with BaO termination (left) and ZrO_2 termination (right) and its projection over the different planes in the slabs. Each plane can have either BaO or ZrO_2 composition. For the ZrO_2-terminated surface, surface states increase the valence band maximum and decrease the material band gap. For having the same scale in every diagram, the DOS projections are magnified by 5 times.

6.2. Surface Energy and Thermal Stability of its Terminations

The cleavage, relaxation and surface electronic energies (quantities described in Section 3.1.1) are reported in Table 6.2. We find that the BaO-terminated surface has a slighter higher surface energy than the ZrO_2-terminated one; however, the difference is extremely small (0.02 eV) and both termination can be considered energetically equally favorable. A comparison with the literature shows that such a small energy difference between the two terminations is common for the $BaZrO_3$ (001) surface [146, 144].

The electronic surface energy gives only a rough approximation to the surface stability, a more accurate approach relies on the evaluation of the surface energy (per unit area), ω, expressed in equation (3.25) of Section 3.1.1, which explicitly takes into consideration the temperature dependence of the atomic chemical potentials. In Section 3.1.1 we mentioned that, for ABO_3 perovskites, only two chemical potentials are needed to evaluate ω. We have chosen them to be μ_O and μ_{Zr}. Their values can differ from the standard state chemical potential only over restricted ranges, which are defined by equations analogous to equations (3.40) to (3.44).

Due to the known inability of hybrid functionals to correctly describe the electronic structure of metals, Ba and Zr molar Gibbs free energies (μ^0_{Ba} and μ^0_{Zr}, respectively) were evaluated from the experimental formation Gibbs energy of the relative binary oxides at room temperature (T_{RT}) and standard pressure (p°), according to:

$$\mu^0_{Ba}(T,p^\circ) \approx g^{bulk}_{BaO}(T_{RT},p^\circ) - \frac{1}{2}\mu^0_{O_2}(T_{RT},p^\circ) - \Delta_{f,exp}g^0_{BaO}(T_{RT},p^\circ); \quad (6.1)$$

$$\mu^0_{Zr}(T,p^\circ) \approx g^{bulk}_{ZrO_2}(T_{RT},p^\circ) - \mu^0_{O_2}(T_{RT},p^\circ) - \Delta_{f,exp}g^0_{ZrO_2}(T_{RT},p^\circ). \quad (6.2)$$

Quantity	BaO termination	ZrO_2 termination
Cleavage Energy (eV/cell)	1.45	
Relaxation Energy (eV/cell)	-0.14	-0.16
Surface Energy (eV/cell)	1.31	1.29

Table 6.2.: Cleavage energy of the $BaZrO_3$ (001) surface, relaxation and surface energy calculated for the two different terminations. The surface energy is calculated including only the electronic contribution to the system total energy.

T K	$\Delta_f g^0_{BaZrO_3}$ eV/ f. unit	$\Delta_f g^0_{BaO}$ eV/ f. unit	$\Delta_f g^0_{ZrO_2}$ eV/ f. unit
298.15	-17.48	-5.39	-10.80
500	-16.49	-5.09	-10.12
900	-15.84	-4.90	-9.58

Table 6.3.: Formation Gibbs energy of $BaZrO_3$(s), BaO(s) and ZrO_2(s) calculated at different temperatures per formula unit (f. unit).

The experimental values of the formation energy of BaO (cubic phase, $Fm\bar{3}m$) and ZrO_2 (monoclinic phase, $P2_1/c$) were taken from references [149] and [150], respectively. All other quantities are calculated from first-principles, as explained in Section 3.1. For simplicity, the atomic chemical potential of the metal species are considered to be temperature independent.

From the chemical potentials of metal atoms, one can calculate from first-principles the molar Gibbs formation energy of BaO(s) ($\Delta_f g^0_{BaO_2}$), ZrO_2(s) ($\Delta_f g^0_{ZrO_2}$) and $BaZrO_3$(s) ($\Delta_f g^0_{BaZrO_3}$), which are reported in Table 6.3 for three selected temperatures: room temperature (298.15 K), SOFCs intermediate- (500 K) and high- (900 K) temperature working conditions. At this point, we have all the ingredients needed to evaluate equations (3.40)-(3.44) and to draw the phase diagram in the $(\Delta\mu_{Zr}, \Delta\mu_O)$-plane. The results are shown in Figure 6.5a for three different temperatures. Equations (3.40) and (3.41) just impose the upper bound of the two variables $\Delta\mu_O$ and $\Delta\mu_{Zr}$, respectively. Equations (3.47) to (3.49) define the following three straight lines in the $(\Delta\mu_{Zr}, \Delta\mu_O)$-plane:

$$\Delta\mu_{Zr}(T,p) + 3\Delta\mu_O(T,p) = \Delta_f g^0_{BaZrO_3}(T,p); \tag{6.3}$$

$$\Delta\mu_{Zr}(T,p) + 2\Delta\mu_O(T,p) = \Delta_f g^0_{BaZrO_3}(T,p) - \Delta_f g^0_{BaO}(T,p); \tag{6.4}$$

$$\Delta\mu_{Zr}(T,p) + 2\Delta\mu_O(T,p) = \Delta_f g^0_{ZrO_2}(T,p). \tag{6.5}$$

These straight lines are illustrated by bold black lines in Figure 6.5a and represent the points in the $(\Delta\mu_{Zr}, \Delta\mu_O)$-plane where $BaZrO_3$ is in equilibrium with other compounds. In particular, equation (6.3) establishes the condition in which $BaZrO_3$ is in equilibrium with Ba; equation (6.4) the equilibrium between $BaZrO_3$ and BaO and equation (6.5) between $BaZrO_3$ and ZrO_2. The inequality symbols in equations (3.42) to (3.44) define the region of the $(\Delta\mu_{Zr}, \Delta\mu_O)$-plane in which a compound is more stable than the other. Figure 6.5 shows that $BaZrO_3$, and thus its (001) surface, is stable only on the narrow chemical potential region represented by the white color. The dashed line represents the points in the $(\Delta\mu_{Zr}, \Delta\mu_O)$-plane where

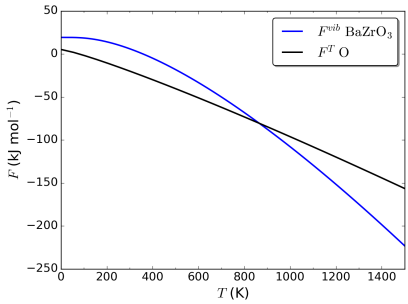

Figure 6.4.: Thermal contributions to the Gibbs free energy of $BaZrO_3$ and O. For $BaZrO_3$, the contributions arise from the vibrational Helmholtz free energy, F^{vib}; for the oxygen atoms, the contributions arises from the translational, rotational and vibrational Helmholtz free energy, F^T.

the two termination have the same surface energy: $\omega_{\mathrm{BaO}} = \omega_{\mathrm{ZrO_2}}$. Below this dashed line, $\omega_{\mathrm{BaO}} < \omega_{\mathrm{ZrO_2}}$ and above it, $\omega_{\mathrm{BaO}} > \omega_{\mathrm{ZrO_2}}$. At 298.15 K, Figure 6.5a shows that the (001) surface can have only the BaO termination, since the ZrO_2 one assumes a lower surface energy for values of $\Delta\mu_{\mathrm{Zr}}$ and $\Delta\mu_{\mathrm{O}}$ such that ZrO_2 would segregate from $BaZrO_3$. Increasing the temperature stabilizes the ZrO_2 termination over the BaO one: at 500 K, the (001) surface could show both kind of terminations, while at 900 K the region in which the BaO termination is stable turns out to be rather negligible. We want to stress the fact that the temperature effects arise from the inclusion of the contributions given by lattice vibrations (through F^{vib}) and the thermal contribution to the free oxygen atom chemical potential (which includes the translational, rotational and vibrational degrees of freedom, F^T) in the Gibbs free energy. These quantities affect both the values of the compounds formation energies ($\Delta_f g^0_{\mathrm{BaZrO_3}}$, $\Delta_f g^0_{\mathrm{BaO}}$ and $\Delta_f g^0_{\mathrm{ZrO_2}}$), which leads to the shift of the bold straight lines in Figure 6.5a with the temperature, and the values of the surface energies (ω_{BaO} and $\omega_{\mathrm{ZrO_2}}$), which leads to the shift of the dashed lines. Both F^{vib} and F^T play an important role since the value they assume are comparable, as illustrated in Figure 6.4.

As already stated above, the choice of $\Delta\mu_{\mathrm{O}}$ and $\Delta\mu_{\mathrm{Zr}}$ as independent variables was purely arbitrary. Whereas the chemical potential difference of the gas phase, $\Delta\mu_{\mathrm{O}}$, can be easily tuned in experiments, e.g. through the gas partial pressure, differences in the chemical potential of metal species are extremely difficult to control. From the experimental point of view, it can be easier to modify the chemical potentials of the oxides through their equilibrium vapor pressure. In practice, such

pressures are extremely low ($\approx 10^{-3}$ Pa at $\approx 1000\,\mathrm{K}$) and very difficult to control. On the other hand, from a computational point of view, is extremely simple to replot Figure 6.5a in the $(\Delta\mu_{\mathrm{BaO}}, \Delta\mu_{\mathrm{O}})$-plane. The procedure is analogous to that which led to equations (3.40)-(3.44) and results in the following equations:

$$\Delta\mu_{\mathrm{O}}(T,p) \leq 0; \tag{6.6}$$

$$\Delta\mu_{\mathrm{BaO}}(T,p) - \Delta\mu_{\mathrm{O}}(T,p) \leq -\Delta_f g^0_{\mathrm{BaO}}(T,p); \tag{6.7}$$

$$\Delta\mu_{\mathrm{BaO}}(T,p) + 2\Delta\mu_{\mathrm{O}}(T,p) \geq \Delta_f g^0_{\mathrm{BaZrO_3}}(T,p) - \Delta_f g^0_{\mathrm{BaO}}(T,p); \tag{6.8}$$

$$\Delta\mu_{\mathrm{BaO}}(T,p) \leq 0; \tag{6.9}$$

$$\Delta\mu_{\mathrm{BaO}}(T,p) \geq \Delta_f g^0_{\mathrm{BaZrO_3}}(T,p) - \Delta_f g^0_{\mathrm{ZrO_2}}(T,p) - \Delta_f g^0_{\mathrm{BaO}}(T,p). \tag{6.10}$$

The results are shown in Figure 6.5b and are analogous to those shown in Figure 6.5a. In particular, it is clear that the BaO termination is the most stable at low temperatures while the ZrO_2 termination is stabilized at higher temperatures.

In conclusion, due to the several approximations involved, diagrams like those of Figure 6.5 might not give precise quantitative predictions; however they can be used to gain a qualitative insight on the system.

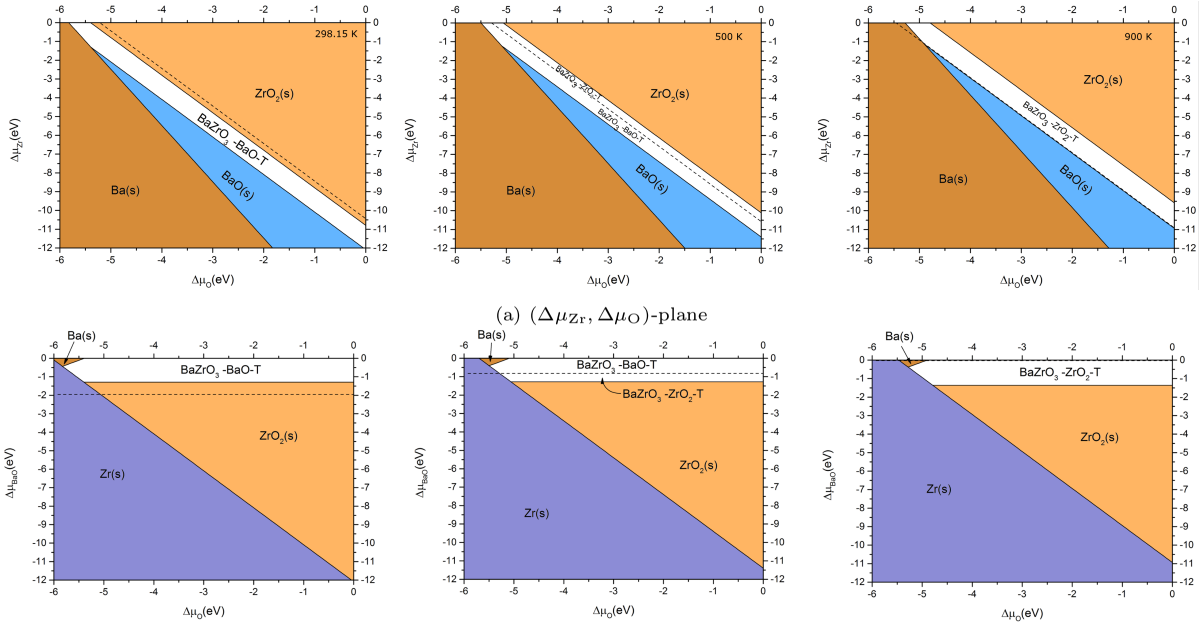

(a) $(\Delta\mu_{\mathrm{Zr}}, \Delta\mu_{\mathrm{O}})$-plane

(b) $(\Delta\mu_{\mathrm{BaO}}, \Delta\mu_{\mathrm{O}})$-plane

Figure 6.5.: Stability diagrams for the $BaZrO_3$ (001) surface at different temperatures (from left to right: 298.15 K, 500 K and 900 K). Top window: The colored areas show the most stable systems for those value of $\Delta\mu_{\mathrm{O}}$ and $\Delta\mu_{\mathrm{Zr}}$. The dashed line indicates the value of $\Delta\mu_{\mathrm{O}}$ and $\Delta\mu_{\mathrm{Zr}}$ for which both the BaO and ZrO_2 terminations have the same surface energy. The diagrams are reported for a pressure of 1 atm and three different temperatures. Bottom window: Previous plot represented choosing $\Delta\mu_{\mathrm{BaO}}$ instead of $\Delta\mu_{\mathrm{Zr}}$.

6.3. Oxygen Vacancies on the (001) Surface

The behavior of point defects at surfaces and interfaces is of fundamental importance for all electrochemical applications. In this Section we report the results for the atomic and electronic properties of the neutral, $v_O^{\times}$, and doubly-charged, $v_O^{\bullet\bullet}$, oxygen vacancies located on the ZrO_2-terminated (001) surface of $BaZrO_3$. We calculate the defect (electronic) segregation energy and for $v_O^{\bullet\bullet}$, which is the most relevant oxygen vacancy involved in practical applications of $BaZrO_3$, also the segregation enthalpy and entropy at non-zero temperatures.

Our computational model employed a symmetric non-stoichiometric slab consisting of 7 atomic planes. To reduce the spurious defect-defect interactions, we employed a 3×3 expansion of the primitive $BaZrO_3$ surface unit cell. Such slabs contain a total of 162 atoms. To keep the symmetry system as high as possible in order to reduce the computational costs, oxygen vacancies were placed on both slab surfaces.

The lattice distortions brought by the defects in the host material are illustrated in Figure 6.6 and quantified in Table 6.4. As already noticed for oxygen vacancies in bulk $BaZrO_3$, the doubly-charged vacancy $v_O^{\bullet\bullet}$ distorts the host lattice much more than the neutral defect $v_O^{\times}$. A comparison between Table 6.4 and Table 5.2 shows also that oxygen vacancies distort the local structure more on the surface than inside the bulk. This can be readily explained considering the lower coordination of the surface atoms, which have more degrees of freedom to rearrange themselves after the introduction of a point defect.

The electronic density of states (DOS) of surface oxygen vacancy is compared in Figure 6.7 with that of the clean ZrO_2-terminated (001) surface. As in the bulk, $v_O^{\times}$ induces a defective level inside the band gap which is fully occupied by two

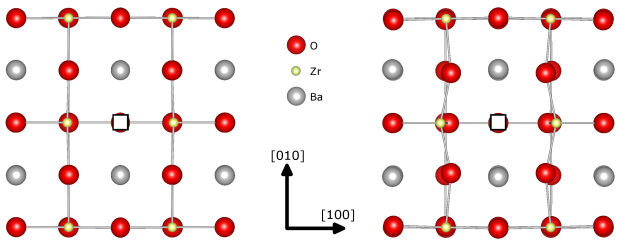

Figure 6.6.: Lattice relaxations around neutral and charged oxygen vacancies ($v_O^{\times}$ and $v_O^{\bullet\bullet}$, respectively) on the ZrO_2-terminated (001) surface of $BaZrO_3$.

Distortions	$v_O^{\times}$	$v_O^{\bullet\bullet}$
Δd(Zr-v_O)/d_0(Zr-O) (%)	4.87	10.44
Δd(Ba-v_O)/d_0(Ba-O) (%)	10.15	-7.63
Δd(O-v_O)/d_0(O-O) (%)	1.70	-17.79

Table 6.4.: Calculated structural distortions induced by oxygen vacancies in two different charge states on the ZrO_2-terminated (001) surface of $BaZrO_3$. Δd(X-v_O)/d_0(X-O) indicates the relative displacement of atom X with respect to the original X-O distance in the pristine surface system (d_0(X-O)). The displacements are reported for the vacancy nearest neighbors only. A negative sign indicates an inward relaxation, a positive one an outward relaxation.

electrons. Due to the band gap reduction observed for the ZrO_2-terminated surface and explained in Section 6.1, the empty defective band induced by $v_O^{\bullet\bullet}$ merges with the conduction band. The Mulliken charges in the oxygen vacancies are $0.88\,e$ and $0.19\,e$ for $v_O^{\times}$ and $v_O^{\bullet\bullet}$, respectively. These values are slightly lower than in the bulk, in agreement with the charge redistribution illustrated in Figure 6.2 which shows a depletion of the ionic charges in order to strengthen the Zr-O covalent bonds.

The defect *segregation energy* is defined as the difference between the defect formation energy on the surface and in the bulk:

$$\Delta_{seg}E = \Delta_f E_{surf} - \Delta_f E_{bulk}; \tag{6.11}$$

where $\Delta_f E_{surf}$ and $\Delta_f E_{bulk}$ are the formation energies of the surface and bulk defect, respectively. In order to avoid the complicated issues involved in the calculation of the electronic energies of charged 2-dimensional systems, the segregation energy of $v_O^{\bullet\bullet}$ was calculated employing charge-compensating defects. In particular, since our slab model contains two $v_O^{\bullet\bullet}$, a Zr vacancy, $v_{Zr}^{''''}$, was inserted in the slab central plane, as far as possible from the oxygen vacancies, in order to maximally reduce the defect-defect interactions. Segregation enthalpies, $\Delta_{seg}H$, and entropies, $\Delta_{seg}S$, are define analogously as the segregation energy in equation (6.11); in particular, since the introduction of the charged background affects only the system electronic energy, the vibrational contributions to $\Delta_{seg}H$ and $\Delta_{seg}S$ can be calculated without introducing any charge-compensating defect.

The calculated (lectronic) segregation energies for $v_O^{\times}$ and $v_O^{\bullet\bullet}$ amount to 0.46 eV and -0.73 eV, respectively. This indicates that the migration of $v_O^{\times}$ from the bulk toward the surface is energetically unfavorable; whereas, on the other hand, $v_O^{\bullet\bullet}$ tends to segregate on the surface. The latter finding agrees with the observation that acceptor-doped $BaZrO_3$ displays a very high grain boundary resistance, which is

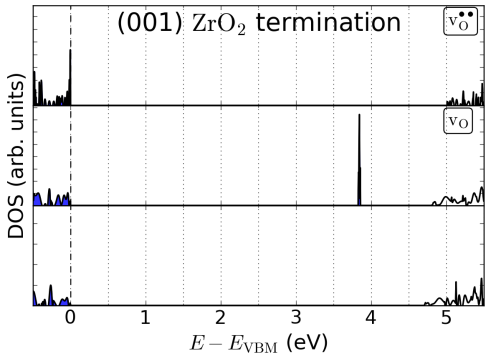

Figure 6.7.: Comparison between the DOS calculated for oxygen vacancies ($v_O^{\times}$ and $v_O^{\bullet\bullet}$) on the ZrO_2-terminated (001) surface of $BaZrO_3$ and for the clean surface. The dashed line emphasizes the valence band maximum while the blue filling indicates occupied states. In particular, the defective level induced by $v_O^{\times}$ is fully occupied, while that induced by $v_O^{\bullet\bullet}$ is empty and mixed with the conduction band states.

attributed to positively charged grain boundary cores and the subsequent depletion of mobile protons in the surrounding space charge region [151, 152, 153, 154].

Figure 6.8 illustrate the thermal contributions to the formation and segregation enthalpy and entropy of $v_O^{\bullet\bullet}$ arising from lattice vibrations. The oxygen chemical potential is not included in this plot since its contribution results canceled out as follow from the definition of the segregation enthalpy or entropy (cf. with equation (6.11)). From Figure 6.8a, it can be seen that the vibrational contributions to the defect formation enthalpy, $\Delta_f H^{vib}$, are very similar for $v_O^{\bullet\bullet}$ situated in the bulk on on the surface. As a consequence, the segregation enthalpy of $v_O^{\bullet\bullet}$ assumes a small constant value around 5 meV. On the other hand, the vibrational contributions to the formation energy of the surface $v_O^{\bullet\bullet}$ are noticeably smaller than in the bulk. Despite the fact that surface oxygen vacancies cause larger local lattice distortions than in the bulk, the host material structure is overall more distorted when $v_O^{\bullet\bullet}$ is located in the bulk rather than on the surface, due to the lower coordination number of surface species and the fact that the structural distortions affect mostly the neighboring atoms and quickly subside far from the surface. As a consequence, $v_O^{\bullet\bullet}$ shows a positive segregation entropy, which reaches, above 200 K, a constant value of around 0.45 meV/K. The segregation Helmholtz free energy is therefore dominated by the entropy term, which encourages the migration of $v_O^{\bullet\bullet}$ toward the surface at high temperatures.

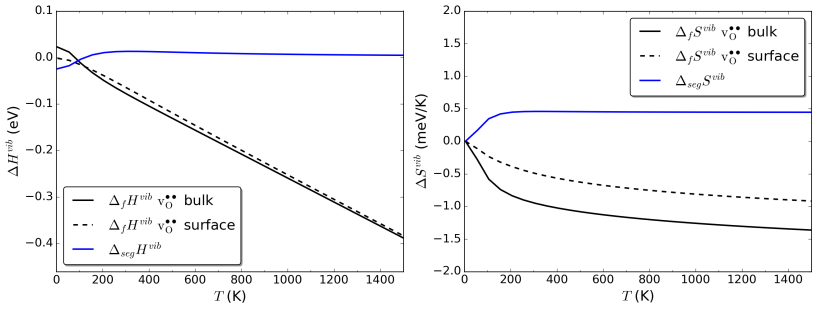

(a) (b)

Figure 6.8.: Left: Vibrational contributions to the formation (black lines) and segregation (blue line) enthalpy of $v_O^{\bullet\bullet}$. Right: Vibrational contributions to the formation (black lines) and segregation (blue line) entropy of $v_O^{\bullet\bullet}$. All the quantities are calculated employing ZrO_2-terminated $BaZrO_3$ slabs consisting of 7 atomic planes.

In conclusion, in this Chapter, we have studied the two terminations of $BaZrO_3$ (001) surfaces. We have shown how the electronic charge density is redistributed in different ways according to the surface termination plane and how this affects the electronic and atomic properties of the surfaces. In particular, for ZrO_2-terminated surfaces, the surface electrons are redistributed between the ions, strengthening the Zr-O bonds. As the result, the surface rumpling is smaller here than in BaO-terminated surfaces and a surface state appears just above the valence band maximum, reducing the material band gap by ≈ 0.8 eV. On the other hand, the character of the surface Ba-O bond remains mostly ionic and the surface rumpling does not lead to relevant surface states around the bands edges of BaO-terminated surfaces.

We have calculated the surface energy for both terminations and applied a simple thermodynamic model to take into account realistic environmental conditions. Lattice vibrations play a major role in defining the surface stability as a function of the temperature. In particular, we found that at low temperatures the BaO termination turns out to be the most stable but, as the temperature increases, the ZrO_2 tends to become the most stable. However, our thermodynamic model is quite simple and gives only a qualitative description of the system; among the major limitations of this model we want to point out the inability to predict phases which have not been already taken into account introducing the proper chemical potentials (e.g. as in equations (6.6) - (6.10)), the inability to predict metastable phases and all the limitations arising from the approximations of the metal chemical potentials,

viz. their assumed temperature-independence.. Finally, we have studied the neutral and doubly-charged surface oxygen vacancies. We found that the surface defects induced larger local lattice distortions than in the bulk; however, due to the reduced coordination of surface oxygen atoms, the surface structure is overall less affected than the bulk one. This leads to a formation entropy for the surface $v_O^{\bullet\bullet}$ larger than in the bulk case. As a consequence, the segregation entropy of $v_O^{\bullet\bullet}$ is positive and thus this defect is stabilized on the surface at high temperature. The segregation enthalpy of $v_O^{\bullet\bullet}$ was found to be $\approx -0.7\,\mathrm{eV}$, which coupled with the positive segregation entropy, suggests the defect strong tendency to segregate toward the surface. This finding is in agreement with experimental data [151, 152, 153, 154] suggesting that the segregation of $v_O^{\bullet\bullet}$ toward the grain boundary cores is the responsible for the positively charged grain boundaries observed in acceptor-doped $BaZrO_3$.

7. Ultra-thin Films and Oxygen Vacancies Therein

In this last Chapter we consider free-standing ultra-thin films of $BaZrO_3$ terminated by the (001) surface. Such thin films offer a simple model for investigating the material behavior in confined regions, such as in the proximity of an interface with another material or in the grain section close to a boundary.

The thin films are modeled employing symmetrical slabs, analogous to those described in Chapter 6. Both the AO and BO_2 (001) surface terminations are considered and slabs with a number of atomic planes ranging from 3 to 7 (film thickness $\approx$ 0.4 to 1.2 nm) are studied in order to assess how the dimensional confinement affects the system properties.

In the last Section we consider oxygen vacancies ($v_O^{\times}$ and $v_O^{\bullet\bullet}$) inside the thin films in order to study the 1-dimensional spatial confinement effects on the defect properties, with particular focus on the role of lattice vibrations and the vibrational contributions to the defect formation energy.

In the following discussion, we will use the term *film unit cell* to denote the volume of the system enclosed between the two film surfaces and spanned by the two crystal primitive vectors along the film periodic dimensions.

7.1. Defective-free $BaZrO_3$ Ultra-thin Films

Figure 7.1 illustrates the slab model used to model $BaZrO_3$ ultra-thin films; in particular, it shows films with a thickness of 5 atomic planes. The Zr-O-Zr complex, which includes an oxygen atom in the slab central plane, is emphasized. The orientation of this complex with respect to the film surface is important when an oxygen vacancy is introduced in place of the oxygen atom. To stress this fact, we denote, hereafter, as *type-I* and *type-II* the films in which the $Zr - v_O(O) - Zr$ complex lies perpendicular or parallel to the (001) surface, respectively.

Table 7.1 reports the surface rumpling s, and interplanar distances, Δd_{12} and Δd_{23}, between the uppermost metal layers (these quantities are defined in Section 6.1) as a function of the number of atomic planes in the film. The values are

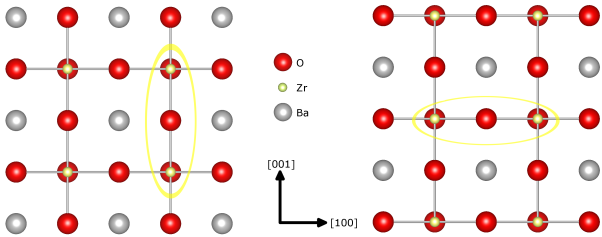

Figure 7.1.: Slab models employed for modeling $BaZrO_3$ ultra-thin films. Both the BaO (left) and ZrO_2 (right) terminations are considered. The Zr-O-Zr complex is highlighted. Its orientation can be either perpendicular (left, *type-I*) or parallel (right, *type-II*) to the film surface.

compared with those obtained for the 15-plane slabs employed for the study of the (001) surface (Chapter 6). For the thinnest films made of just 3 atomic planes, Δd_{23} is omitted since it is equivalent to Δd_{12}. BaO-terminated 3-plane films show a surface rumpling noticeably smaller than in thicker films, phenomenon probably related to the reduced degrees of freedom of surface atoms in such extremely thin films. For all other films, the surface relaxation parameters are not noticeably affected by the slab thickness and quickly converge to the value found in much thicker slabs.

Figure 7.2 shows the electronic DOS calculated for the thin films and that calculated previously for the 15-plane slab. The total DOS is projected over the states of the atoms forming the different slab planes. Each plane can have either BaO or ZrO_2 composition and thus contains two different type of atoms. The "bulk" designation employed for 7-plane slabs indicates the atomic plane located at the slab center. We can notice that the DOS is not noticeably affected by the film thickness but more by the termination layer type which, on ZrO_2-terminated slabs, induces the surface states at the top of the valence band maximum already discussed in Section 6.1.

Figure 7.3 illustrates the charge redistribution occurring in *type-II* ultra-thin films as a function of the slab thickness. As already pointed out for surfaces in Chapter 6, the electronic charge accumulates toward the surface, increasing the covalency of the Zr-O bonds. Considering the films inner planes, and, in particular, the slab central plane, it can be noticed that the electronic density redistribution quickly approaches the bulk value. When one of the Zr atoms in the Zr-O-Zr complex lies on the film surface, some electronic charge shifts from the O atom toward this surface Zr atom, as it may be seen in the panel of Figure 7.3 relative to the 5-plane slab.

	BaO termination			ZrO_2 termination		
Planes	s	Δd_{12} (Å)	Δd_{23} (Å)	s	Δd_{12} (Å)	Δd_{23} (Å)
3	2.17	2.01(-3.95)	-	1.37	2.02(-3.74)	-
5	3.14	1.92(-8.57)	2.15(2.59)	1.42	1.92(-8.57)	2.19(4.31)
7	3.39	1.90(-9.55)	2.18(4.04)	1.41	1.90(-9.55)	2.21(5.74)
15	3.62	1.88(-10.4)	2.19(4.26)	1.31	1.88(-10.4)	2.22(5.74)

Table 7.1.: Surface rumpling, s and the interplanar distances between the uppermost metal layers, Δd_{12}, Δd_{23} as a function of the number of atomic planes in the film. The rumpling is reported as relative percentile with respect to the calculated bulk lattice constant of 4.195 Å. The interplanar distances are reported in Å; while the values in brackets refer to the relative percentile value with respect the Zr-Ba distance along the [001]-direction in bulk $BaZrO_3$. A positive value indicates an expansion of relative distances, while a negative value a contraction thereof. Δd_{23} is omitted for films made of three atomic planes since it is equivalent to Δd_{12}.

As the Zr-O-Zr complex lies in the film inner planes and parallel to the surface, the electronic density redistribution is almost independent on the film thickness and rapidly assumes the bulk configuration.

Finally, we analyzed the vibrational density of states (VDOS) calculated for the ultra-thin films. Figure 7.4 reports the VDOS calculated for ZrO_2-terminated ultra-thin films composed of 3, 5 and 7 atomic planes; the bulk VDOS is also shown for a comparison. Apart from the different intensities, arising from the different number of atoms in the various systems, the most striking difference between thin films and the bulk is the appearance of low-frequency modes in the $50\,cm^{-1}$ region which are absent in bulk $BaZrO_3$. The analysis of the eigenvectors shows that these modes originate from the vibrations of surface oxygen atoms and their surface rumpling. Noteworthy, the VDOS in the 50-100 cm^{-1} region is almost identical for 5- and 7-plane films and only slightly differs for 3-plane films. Thin films also show vibrational modes at $\approx 200\,cm^{-1}$ which do not appear in the bulk and are related to the vibration of atoms in the subsurface and other outer planes. Overall, 3-plane films show a blue shift of all the phonon frequencies; whereas for thicker films, the situation is analogous as in the bulk. This fact can be explained by the already mentioned fact that 3-plane films are too thin to allow for a complete lattice relaxation; therefore, some elastic strain affects the structure and leads to an increase of the vibrational frequencies.

In conclusion, except for surface effects, ultra-thin films of $BaZrO_3$ are remarkably similar to the bulk, with only 3-plane films showing noticeably different properties.

This indicates that the dimensional confinement has only short-range effects on these systems.

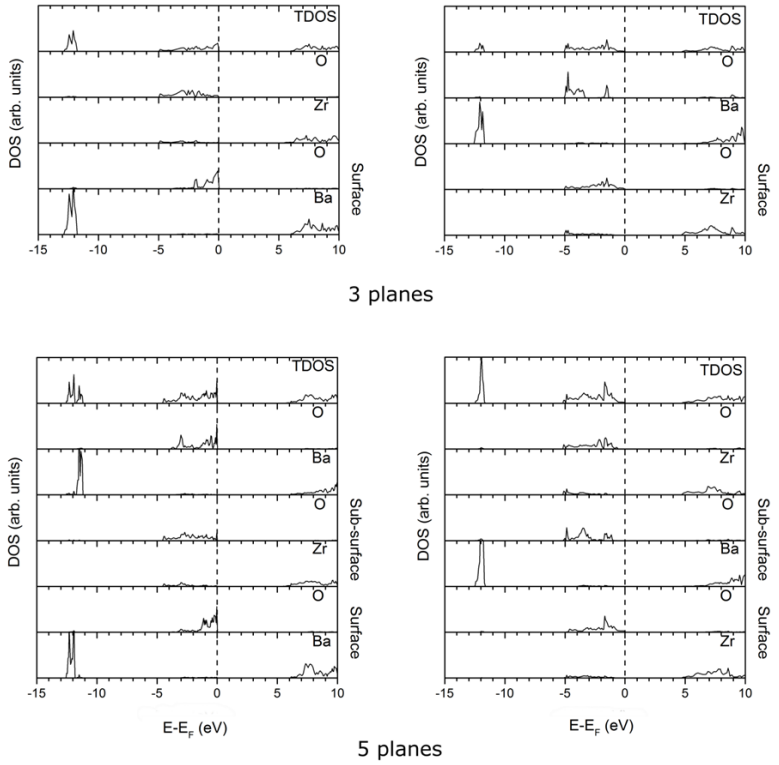

Figure 7.2.: Total electronic DOS calculated for the $BaZrO_3$ ultra-thin films with BaO termination (left) and ZrO_2 termination (right) and its projection over the states of the atoms in the different slab planes. Each plane has either BaO or ZrO_2 composition. For having the same scale in every diagram, the DOS projections are magnified by 5 times.

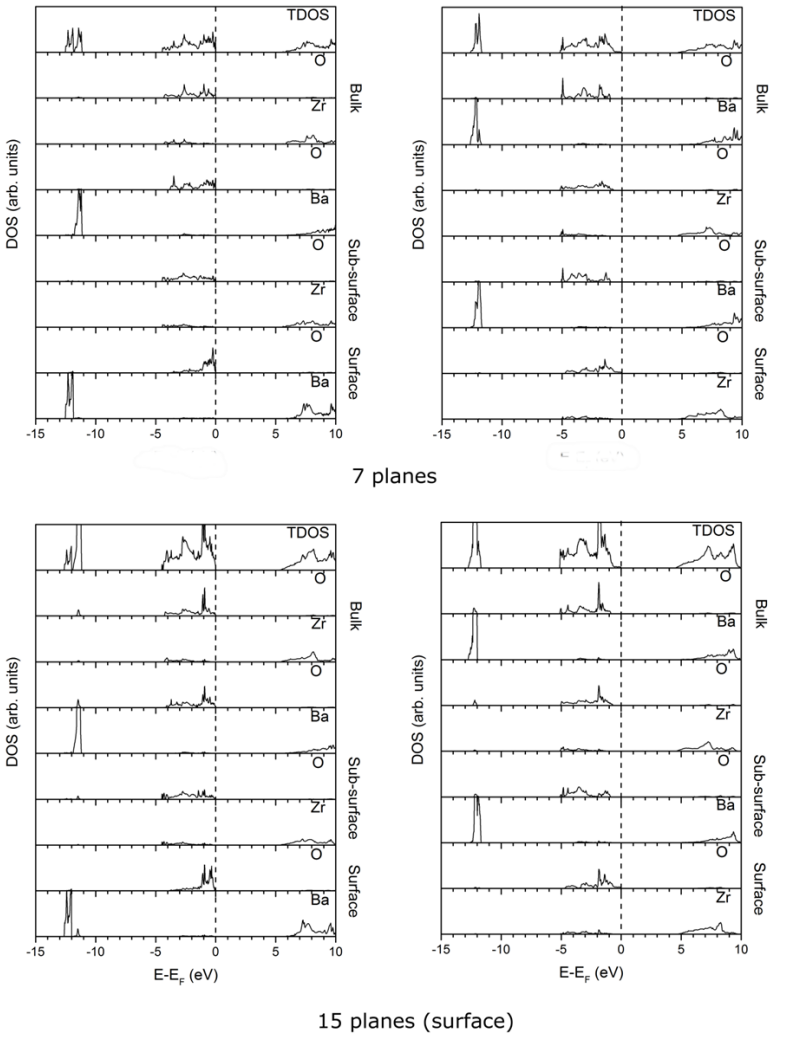

Figure 7.2.: (Continued) Total electronic DOS calculated for the $BaZrO_3$ ultra-thin films with BaO termination (left) and ZrO_2 termination (right) and its projection over the states of the atoms in the different slab planes. Each plane has either BaO or ZrO_2 composition. For having the same scale in every diagram, the DOS projections are magnified by 5 times.

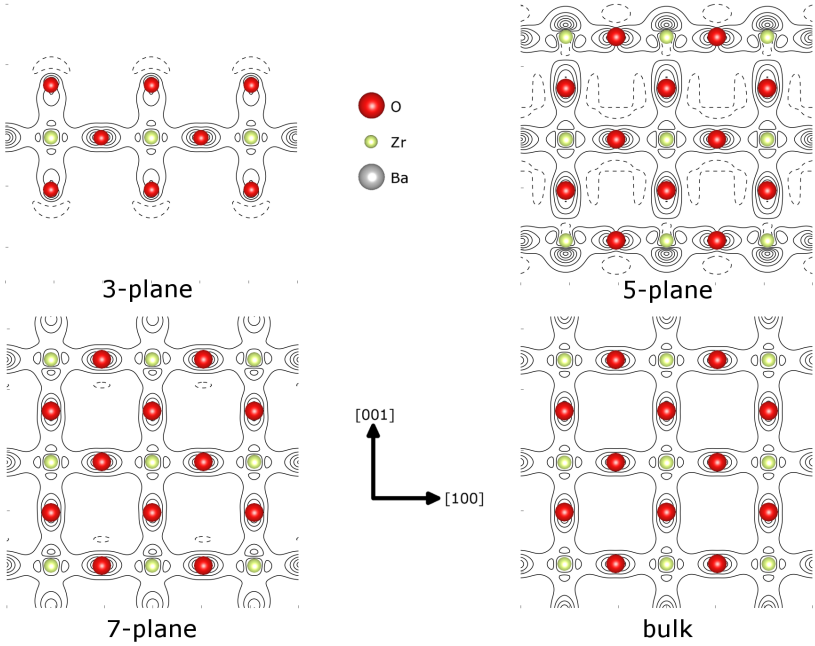

Figure 7.3.: Electronic density redistribution for *type-II* $BaZrO_3$ ultra-thin films and comparison with the bulk. The plot represents the electron-charge density difference between the slab model and the ideal ionic configuration of bulk $BaZrO_3$. Full lines indicate an accumulation of charge density and dashed lines a depletion thereof.

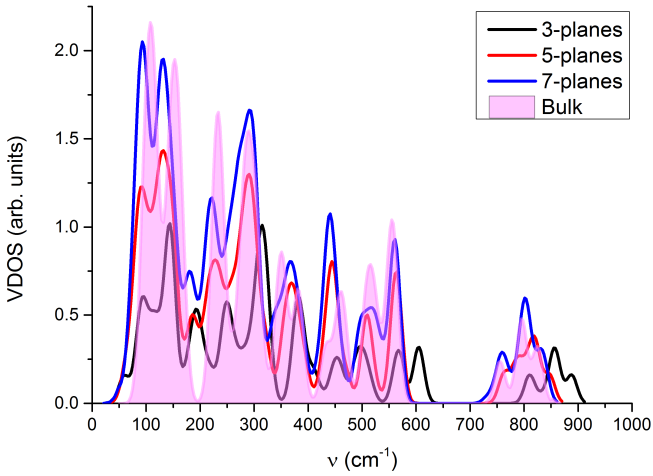

Figure 7.4.: Vibrational density of states of ZrO_2-terminated $BaZrO_3$ ultra-thin films and comparison with the bulk. For the thin films, the vibrational frequencies were calculated at 9 points of the first Brillouin Zone; for bulk, at 27 points.

7.2. Oxygen Vacancies in $BaZrO_3$ Ultra-thin Films

Oxygen vacancies were placed in the slab central plane, we expanded the surface unit cell 3×3 times in order to decrease the spurious defect-defect interactions arising from the periodic boundary conditions. As before, we consider the vacancy in two charge states: neutral, $v_O^{\times}$, and doubly-charged, $v_O^{\bullet\bullet}$. As in the previous Section, the basis set of the removed oxygen ion is kept on the vacant site in order to obtain a more accurate and flexible description of the electronic charge density distribution. The distortions brought by the defects on the host structure are summarized in Table 7.2 as a function of the film thickness. As pointed out in the previous Sections, the electrostatic interactions between the charged oxygen vacancy and its neighbors are the main reason for the largest structure relaxation reported for $v_O^{\bullet\bullet}$ as compared to $v_O^{\times}$. For 3-plane films, the lattice distortion affects the film structure so much that the slab becomes unstable. In particular, we found that 3-plane films containing $v_O^{\bullet\bullet}$ produce negative vibrational frequencies; a clear indication that the obtained structure is metastable and a real system would rather reconstruct to a different morphology. In contrast, considering films containing $v_O^{\times}$, Table 7.2 shows that difference in the structural relaxation, with respect to the bulk, are relevant only for 3-plane film and *type-I* 5-plane films. In both cases, this may be related to the system thickness which poses different constraints on the structural relaxation.

The film type (*type-I* or *type-II*) also plays a role, as can be seen considering 5- and 7-plane films containing $v_O^{\bullet\bullet}$. In *type-I* films, the Zr-v_O-Zr complex lies perpendicularly with respect to the film surface; therefore, the outward displacements of the two Zr atoms are larger than for the *type-II* films, since, for the formers, only a few atomic layers damp the electrostatic repulsion affecting the two Zr cations. Overall, Table 7.2 shows that the thinner the film, the larger the stress induced by the defect on the local atomic structure.

Regarding the electronic structure, as already shown for bulk $BaZrO_3$, the oxygen vacancies induce an additional band in the energy gap. In particular, for $v_O^{\times}$ this band is fully occupied while remains completely empty for $v_O^{\bullet\bullet}$. Table 7.3 presents the position of the defective band with respect to the conduction band minimum, $\Delta\epsilon$, its width, $\delta\epsilon$, and the Mulliken atomic charges, $q(v_O)$, calculated for $v_O^{\times}$ and $v_O^{\bullet\bullet}$ as a function of the film thickness. The position of the defective band is only slightly affected by the termination and film type and oscillates around the bulk value. The defective level lies deeper than for the bulk for all film thicknesses, but in general, except for 3-plane films, the band position is not particularly affected by film thickness. On the other hand, the defective band width is widely affected by

	BaO termination				ZrO_2 termination			
No. planes	type	Δd(Zr-v_O)/d_0 (%)	Δd(Ba-v_O)/d_0 (%)	Δd(O-v_O)/d_0 (%)	type	Δd(Zr-v_O)/d_0 (%)	Δd(Ba-v_O)/d_0 (%)	Δd(O-v_O)/d_0 (%)
				$v_O^{\times}$				
3	II	-7.2	1.6	-5.9	I	-6.7	1.1	-4.2
5	I	2.8	-0.6	-0.5	II	-1.1	0	-1.4
7	II	-1.2	-0.1	-1.4	I	-0.8	0.1	-1.5
Bulk		-0.3	0.0	-1.1				
				$v_O^{\bullet\bullet}$				
5	I	9.3	2.7	-7.3	II	6.9	3.2	-8.3
7	II	5.2	4.3	-7.8	I	10.4	2.7	-7.0
Bulk		7.5	3.6	-6.2				

Table 7.2.: Calculated structural distortions induced by oxygen vacancies in $BaZrO_3$ ultra-thin films as a function of the thickness. Both ZrO_2 and BaO termination are considered and the corresponding film type is specified. Δd(X-v_O)/d_0 indicates the relative displacement of atom X with respect to the original X-O distance in the pristine surface system (d_0). The displacements are reported for the nearest neighbors only. A negative value indicates an inward relaxation, a positive one an outward relaxation. 3-plane films results unstable if a $v_O^{\bullet\bullet}$ is present; therefore only 5- and 7-plane thickness are considered for $v_O^{\bullet\bullet}$.

	BaO termination				ZrO_2 termination			
No. planes	type	$q(v_O)$ (e)	$\Delta\epsilon$ (eV)	$\delta\epsilon$ (eV)	type	$q(v_O)$ (e)	$\Delta\epsilon$ (eV)	$\delta\epsilon$ (eV)
				$v_O^{\times}$				
3	II	1.16	2.48	0.13	I	1.09	3.10	0.01
5	I	0.93	1.42	0.01	II	1.04	1.65	0.15
7	II	1.06	1.83	0.11	I	1.03	1.96	0.01
Bulk		1.03	1.74	0.15				
				$v_O^{\bullet\bullet}$				
5	I	0.18	0.37	0.09	II	0.20	0.37	0.09
7	II	0.21	0.30	0.13	I	0.19	0.31	0.01
Bulk		0.20	0.18	0.13				

Table 7.3.: Mulliken electronic charge localized within the oxygen vacancy, $q(v_O)$, position of the defective level with respect to the conduction band minimum, $\Delta\epsilon$, and its width, $\delta\epsilon$, calculated for$BaZrO_3$ ultra-thin films as a function of the film thickness.

the film type; however, the results are almost independent on the film termination or thickness. In particular, it is considerably smaller for *type-I* films than for *type-II* ones. The reason is related to the nature of the defective band, which, as observed in the previous Sections, arises mainly from the overlap between the dangling Zrd orbitals and, in a minor way, from the surrounding O2p orbitals. In *type-I* films, the Zr-v_O-Zr complex is oriented along the system aperiodic direction and thus the overlap between the defective wave function is much smaller than in *type-II* films, where the orientation of this complex matches with the system periodicity. The Mulliken atomic charges of the oxygen vacancies are almost independent from the film thickness and termination type, being close to those calculated for the bulk.

In Figure 7.5 we report the vibrational density of states (VDOS) calculated for $BaZrO_3$ ZrO_2-terminated ultra-thin films containing neutral and doubly-charged oxygen vacancies. As already observed in Section 5.3, both $v_O^{\times}$ and $v_O^{\bullet\bullet}$ induce new vibrational modes at $\approx$ 600-700 cm^{-1} which originate from the O-Zr bond stretch involving the Zr atoms in the Zr-v_O-Zr complex and their nearest O ions. Given the small number of atoms in 3-plane films, the whole VDOS of these systems is noticeably affected by the introduction of an oxygen vacancy; whereas for thicker films, differences from the pristine system VDOS are not so apparent. Due to the larger structural distortions brought by $v_O^{\bullet\bullet}$, the blue shift of the vibrational frequencies, discussed in Section 5.3, can be also observed in thin films.

As already mentioned for oxygen vacancies in bulk $BaZrO_3$ (Section 5.3), the local strain field induced by oxygen vacancies on the host structure increases the phonon frequencies and thus decreases the vibrational entropy. This results in a positive vibrational Helmholtz free energy, $\Delta_f F^{vib}$, defined by equation (5.1). In

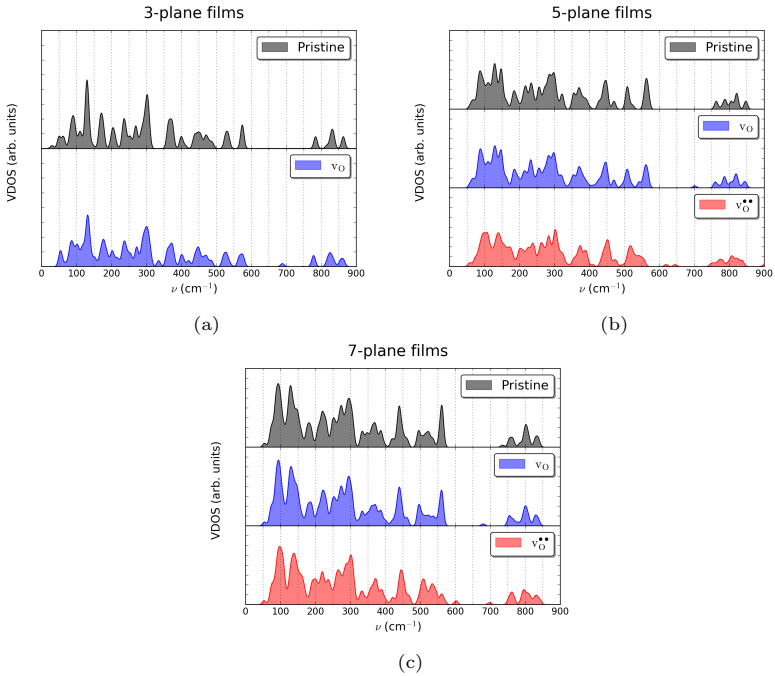

Figure 7.5.: VDOS calculated for $BaZrO_3$ ZrO_2-terminated ultra-thin films consisting of 3-, 5- and 7-atomic planes. The VDOS were calculated expanding the surface unit cell 3×3 times and, therefore, a total of 9 phonon wave vectors are included.

Figure 7.6, we show $\Delta_f F^{vib}$ as a function of temperature for bulk $BaZrO_3$ and the ZrO_2-terminated 3-, 5- and 7-plane ultra-thin films containing $v_O^{\times}$ and $v_O^{\bullet\bullet}$. As already observed for bulk $BaZrO_3$, $\Delta_f F^{vib}$ is much larger for $v_O^{\bullet\bullet}$ than $v_O^{\times}$, due to the larger structural distortions induced by charged defects. Remarkably, except for 3-plane films, $\Delta_f F^{vib}$ is not particularly affected by the film thickness and assumes a value very close to that calculated for oxygen vacancies in bulk $BaZrO_3$. Given the few number of atomic layers in 3-plane films, even a neutral oxygen vacancy can lead to a noticeable film structural distortion, which is reflected in a value of $\Delta_f F^{vib}$ much larger than that observed in thicker films ($\approx 0.4\,\text{eV}$ vs $\approx 0.1\,\text{eV}$ for $v_O^{\times}$ in bulk $BaZrO_3$).

As a last point, we plotted in Figure 7.7 the formation energy of $v_O^{\times}$ calculated

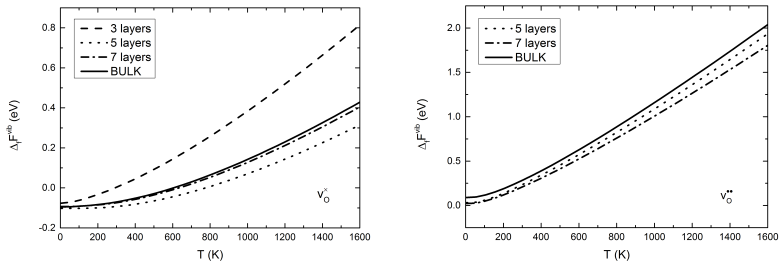

(a) (b)

Figure 7.6.: Phonons contribution to the formation free energy of $v_O^{\times}$ and $v_O^{\bullet\bullet}$ as a function of the temperature for bulk $BaZrO_3$ and ZrO_2-terminated ultra-thin films made of 3, 5 and 7 atomic planes.

at 0 K (electronic part only, the zero-point energy is not taken into account), $\Delta_f E$, as a function of the film thickness for both type of film terminations. It can be observed that $\Delta_f E$ shows a step-like behavior: it is close to the value calculated for bulk $BaZrO_3$ for film consisting of 5 or more atomic planes, and drops by ≈ 0.5 eV in the thinnest 3-plane films. Thus, the electronic structure of systems containing neutral defects is not significantly affected by the dimensional confinement, which can also be explained by the consideration that the electronic density associated to the defect is mostly located on the vacancy nearest neighbors, as illustrated in Figure 5.2. As the temperature is increased, contributions to the defect formation energy due to lattice vibrations and the oxygen chemical potential gain importance. For $v_O^{\times}$, only the last term is relevant but its contribution does not depend on the film thickness. However, for 3-plane films, $\Delta_f F^{vib}$ is not negligible around 1000 K. Here the phonons contributions to the defect formation Gibbs energy becomes almost as large as the reduction in the electronic defect formation energy observed for 3-plane films. Therefore, our findings suggest that, at high temperature, lattice vibrations cause the formation energy of $v_O^{\times}$ to be almost completely independent on the film thickness.

In conclusion, in this Chapter we studied the atomic, electronic and vibrational properties of $BaZrO_3$ ultra-thin films and oxygen vacancies therein. For defective-free films, we found these properties to be only slightly affected by the thin thickness, with considerable deviations observed only for 3-plane films. The effects induced by the introduction of oxygen vacancies are affected only slightly by the film thickness. The largest differences are found, once again, in the thinnest 3-plane films. In particular, charged oxygen vacancies distort such films to the point that the employed

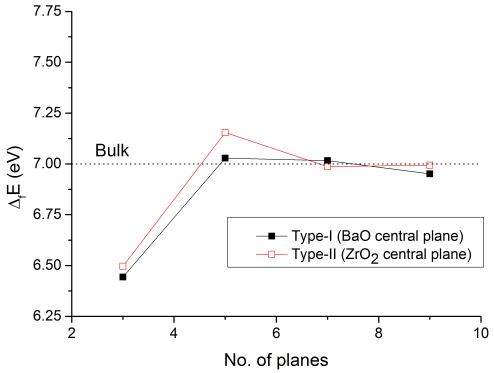

Figure 7.7.: Formation (electronic) energy of $v_O^\times$ in $BaZrO_3$ ultra-thin films as a function of the film thickness for both possible surface terminations.

slab model cannot give a correct description anymore. For neutral oxygen vacancies, we calculated the defect formation energy as a function of the film thickness. Considering only the electronic contributions, we found that the formation energy is almost independent on the film thickness for films consisting of 5-plane films or more; while it is reduced by $\approx 0.5\,\text{eV}$ in 3-plane films. On the other hand, this reduction in the defect formation energy is partly compensated at high temperature, where the phonon contributions to the defect formation energy are much larger for 3-plane films than for thicker ones. This makes the free energy of formation of $v_O^\times$ almost completely thickness-independent at high temperatures.

8. Conclusions

The main objective of this Thesis has been the investigation of oxygen vacancies in ABO_3-type perovskites by means of DFT first-principles calculations; particular emphasis is laid on the contribution of lattice vibrations to the material thermodynamic properties.

We have employed $BaZrO_3$ as a prototype for general cubic ABO_3 perovskites, due to its high chemical and thermal stability, absence of phase transitions at ordinary pressures and promising technological applications.

The calculations have been done employing a localized Gaussian-like basis set: for oxygen atoms an all-electron basis set has been used; while quasi-relativistic pseudo potentials have been employed for describing the core electrons of barium and zirconium atoms. The exchange-correlation functional has been approximated through the hybrid version of the Perdew-Burke-Ernzerhof functional proposed by Adamo and Barone (knwon as the PBE0 functional) which has proved to accurately describe many gound-state properties of perovskite materials. Phonon frequencies have been calculated in the harmonic approximation through the frozen-phonon method. Oxygen vacancies have been modeled through an expansion of the primitive unit cell and employing periodic boundary conditions (supercell method). The basis set of the removed oxygen atom has been kept in the vacancy (*ghost* absis set) in order to provide a more accurate and flexible description of the electronic charge density in the vacant site itself. All first-principles calculation have been performed employing the CRYSTAL computer code.

We have studied $BaZrO_3$ in different phases: bulk, surfaces and ultra-thin films and for each of such phases, oxygen vacancies, v_O, have been considered in different charge states. For bulk $BaZrO_3$, we have considered the neutral ($v_O^{\times}$), singly-charged ($v_O^{\bullet}$) and doubly-charged ($v_O^{\bullet\bullet}$) states and we have calculated their Gibbs energies of formation at different temperatures, employing proper schemes to correct electrostatic finite-size effects. For surfaces and thin films, oxygen vacancies have been considered in the neutral and doubly-charged states only. With the charge of oxygen vacancy, we mean, here, the net charge of the whole supercell. In any charge state, the system electron density is allowed to redistribute itself over the whole system self-consistently.

The main results obtained from this study can be summarized as follows:

Pristine $BaZrO_3$: A comparison with experimental studies shows that our theoretical framework is able to accurately describe many ground-state properties of pristine $BaZrO_3$ such as cell parameters, fundamental band gap, dielectric constants and vibrational frequencies. Additionally, we have been able to correctly estimate the material heat capacity as a function of the temperature, noticing that, to obtain a quantitative agreement with the experimental results, the inclusion of multiple phonon wave vectors in the calculation of the thermodynamic quantities is required. We have found that considering 27 of such wave vectors provides indeed a heat capacity value which differs by less than $5\,\mathrm{J\,mol^{-1}\,K^{-1}}$ from the experimental one.

Oxygen vacancies in bulk $BaZrO_3$: The introduction of an oxygen vacancy affects the host material in several ways. From the point of view of the electronic structure, the point defect induces a new defective band in the band gap. This defective level arises mainly from the overlap between the dangling bonds of the two Zr atoms next to the vacancy, with a smaller contribution given by the orbitals of the nearest O atoms. We have found that, with a $2\times2\times2$ supercell expansion of the primitive cell, finite-size effects related to the interactions between periodically repeated defects are relevant. On the other hand, the use of a $3\times3\times3$ expansion offers a much better description of the defect dilute limit. For all three oxygen vacancy charge states, we have found that some electronic density remains localized within the vacancy itself. The amount of this electronic charge is considerable for $\mathrm{v}_\mathrm{O}^{\times}$ ($\approx -1\,e$) and rapidly decreases for $\mathrm{v}_\mathrm{O}^{\bullet}$ and $\mathrm{v}_\mathrm{O}^{\bullet\bullet}$ ($\approx -0.7\,e$ and $-0.2\,e$, respectively).

The introduction of the oxygen vacancy distorts the local lattice inducing a mechanical stress on the nearest chemical bonds. As the lattice distortions mainly stem from electrostatic forces, the stress increases with the defect charge. As the chemical bonds are stiffened by these distortions, the phonon frequencies increase, leading to a decrease of the vibrational entropy of the defective system with respect to the perfect system. As a result, at high temperatures, where the entropy contribution dominated the free energy, the phonon contribution to the defect Gibbs energy of formation, $\Delta_\mathrm{f}F^{vib}$ is positive. This effect is particularly large for $\mathrm{v}_\mathrm{O}^{\bullet\bullet}$, where $\Delta_\mathrm{f}F^{vib}$ is $\approx 1\,\mathrm{eV}$ at $1000\,\mathrm{K}$, in agreement with the large lattice distortions induced by this defect. The contribution of $\Delta_\mathrm{f}F^{vib}$ therefore affects the relative stability of oxygen vacancies, making highly charged states to be less thermodynamically favorable that lower ones at high temperatures.

$BaZrO_3$ (001) surface and terminations stability: We have considered the two possible terminations of the $BaZrO_3$ (001) surface: BaO and ZrO_2, employing a slab model consisting of 15 atomic planes. Due to the lower coordination number of surface atoms, the atomic structure of the outer planes is rearranged in such a way that the oxygen ions are not coplanar to the metal cations anymore (oxygen surface rumpling). Furthermore, the electronic density redistributed between the surface and sub-surface layers. As a consequence, the covalency degree of the Ba-O and, especially, Zr-O bonds increases compared to the bulk bonds. In particular, the strengthening of the Zr-O bonds produces a smaller oxygen surface rumpling for ZrO_2-terminated surfaces than for BaO-terminated ones. The electronic structure of ZrO_2-terminated surfaces is also characterized by the presence of surface states which contribute to the system valence band maximum, leading to a reduction of the energy gap by $\approx 0.8\,\mathrm{eV}$.

We have also calculated the respective phonon frequencies in order to apply a simple thermodynamic model to study the relative stability between the BaO and ZrO_2 surface terminations. In our model, the surface is considered to be in equilibrium with the bulk and the surrounding atmosphere which acts as a temperature and particle reservoir. This system has only two degrees of freedom which can be chosen to be the chemical potentials of two species (we have considered the chemical potentials of O and Zr and of O and BaO). Through the calculation of phonon frequencies, we have been able to compute the surface energy of both terminations at different temperatures and plot the relative phase diagrams. We have found that at low temperatures the BaO termination is the most stable; whereas the ZrO_2 one becomes the energetically most stable at higher temperatures.

Segregation of oxygen vacancies toward the $BaZrO_3$ (001) surface: We have studied the properties of $v_O^{\times}$ and $v_O^{\bullet\bullet}$ on the (001) surface of $BaZrO_3$ and calculated their segregation energy. At 0 K, we have found a positive segregation energy for $v_O^{\times}$ ($\approx 0.5\,\mathrm{eV}$). The unfavorable segregation of $v_O^{\times}$ in $BaZrO_3$ is a feature not common to all pervoskite oxides, with the segregation being affected by the bond covalency. On the contrary, for $v_O^{\bullet\bullet}$, the segregation energy is negative ($\approx -0.7\,\mathrm{eV}$) in agreement with other perovskite oxides. Due to its role in technological applications, for $v_O^{\bullet\bullet}$ we calculated the segregation energy also at non-zero temperatures. To this point, we need to consider how the host structure is affected by the introduction of the defect. We have found that, on the one hand, $v_O^{\bullet\bullet}$ induces larger local lattice distortions than in the bulk; however, on the other hand, given the lower coordination number of surface atoms, the surface structure results overall less distorted than the bulk one. This leads the surface $v_O^{\bullet\bullet}$ to have a larger surface entropy than the bulk $v_O^{\bullet\bullet}$.

Therefore, the segregation entropy of $v_O^{\bullet\bullet}$ is overall positive and the segregation energy becomes negative. In other words, the segregation of $v_O^{\bullet\bullet}$ toward the surface turns out to be even more favorite at high temperatures.

$BaZrO_3$ ultra-thin films and oxygen vacancies therein: We have considered (001)-terminated ultra-thin films of $BaZrO_3$, consisting from 3 to 7 atomic planes and with $v_O^{\times}$ and $v_O^{\bullet\bullet}$ therein. We have found that the properties of defective-free films are modestly affected by the film thickness, with the most noticeable differences observed in 3-plane films only. Likewise, the properties of oxygen vacancies resemble those observed in bulk $BaZrO_3$, with, once again, only 3-plane films showing remarkably different properties. In particular, we have calculated the formation energy of $v_O^{\times}$ as a function of the film thickness and we have found that, for films consisting of 5 or more atomic planes, it assumes the bulk value; whereas, for 3-plane films the formation energy is lower by $\approx 0.5\,\text{eV}$. On the other hand, the phonon contribution to the defect formation energy, $\Delta_\text{f} F^{vib}$, is noticeably larger in 3-plane films than in thicker ones at high temperatures ($\approx 0.4\,\text{eV}$ in 3-plane films against $\approx 0.1\,\text{eV}$ in thicker films and bulk at 1000 K). This combination makes the Gibbs formation energy of $v_O^{\times}$ almost completely independent on the film thickness at sufficiently high temperatures. Similarly, for $v_O^{\bullet\bullet}$, we have found that for 5- and 7-plane films $\Delta_\text{f} F^{vib}$ assumes the bulk value; while 3-plane films resulted to be unstable after the introduction of $v_O^{\bullet\bullet}$. In conclusion, the one-dimensional spatial confinement effects, on the point defect properties considered here, are very sort-ranged for $BaZrO_3$.

Acknowledgements

Foremost, I would like to express my deep gratitude to Prof. Dr. Joachim Maier for giving me the opportunity to learn and work in his department. Being part of his group has been both a great professional occasion and a significant moment in my personal development.

I acknowledge Prof. Dr. Johannes Kästner and Prof. Dr. Anke Weidenkaff from Stuttgart University for investing their time in being part of my examination committee.

I am extremely indebted with Prof. Dr. Eugene Kotomin, who patiently guided me throughout my Ph.D. program and from whom I acquired most of the knowledge that allowed the completion of this project.

I wish to thank Prof. Dr. Robert Evarestov from St. Petersburg State University, Dr. Tor Bjørheim from Oslo University, Dr. Denis Gryaznov from the University of Latvia and Dr. Eugene Heifets for the helpful scientific discussions, from which I had the opportunity to greatly expand my knowledge.

I acknowledge Dr. Rotraut Merkle for her kind help to provide me with all necessary experimental information.

Many thanks to Uwe Traub and Armin Schuhmacher for organizing and maintaining the computer environment, a key asset for my work.

Special thanks to Sofia Weiglein for her great patience and for assisting me in numerous administrative and bureaucratic issues.

Many thanks also to all my colleagues in Prof. Maier's department for providing a pleasant and special working environment. A special thank goes to my friends Elisa, Federico, Matteo, Giuliano, Adam, Anton, Alessandro and Torben who helped me to feel at home and with whom I shared many nice moments. Many thanks also to my fellow football players for all the fun we had together.

I am grateful to all my friends at home who have always made me feel welcome any time I visited them, in particular to Gabriele and Stefano whose visits to Stuttgart have been greatly appreciated.

Thanks to my girlfriend Sibani, for her support and patience, in particular during the time I was writing this Thesis.

I would also like to thank Prof. Gianfranco Pacchioni from the University of

Milano-Bicocca, for always being supportive and for having helped me to get in contact with Prof. Maier's group.

Finally, I would like to thank my parents, my sister and my aunt Giampiera, who have always supported and encouraged me and to whom I wish to dedicate this work.

Appendices

A. Computational Details

The first-principles calculations performed in this work employed the CRYSTAL computer code [58] in the 09 and 14 version. We used the hybrid functional PBE0 (described in equation 2.57) and a basis set composed by Gaussian-type functions. For the oxygen atoms, we employed the all-electron split-valence triple-zeta basis set 8-411G; Ba and Zr core electrons were treated using quasi-relativistic pseudo potentials taken from the Stuttgart-Cologne pseudopotentials library [155]. The valence electrons were described using 311(1d)G and 311d31G basis sets, respectively. In order to avoid spurious interactions between the diffuse functions and the core functions of neighboring atoms, the basis set diffuse exponents smaller than 0.1 bohr^{-2} were removed, as well as f-electron virtual functions. The employed basis set is listed below:

```
  Ba:

  256 6
INPUT
10 1 2 2 2 1 0
    1.000000           0.000000    0
    9.526986         427.845816    0
    4.487510         204.417530    0
    8.315930         293.605864    0
    4.292217         294.193316    0
    5.916108         112.550402    0
    2.874842         181.782621    0
    3.589465         -33.473174    0
0 0 3 2.0 1.0
    2.3961900         -5.9288950
    2.2433050          6.6469340
    0.7174020         -0.5514370
0 0 1 0.0 1.0
    0.2784460          1.0000000
0 2 3 6.0 1.0
```

```
    2.9267420          0.7633590
    2.5207180         -1.0220140
    0.5240950          0.6498360
0 2 1 0.0 1.0
    0.2034280          1.0000000
0 3 3 2.0 1.0
    0.9663150         -0.9089380
    0.8938280          0.9472400
    0.2731950          0.3220570
0 3 1 0.0 1.0
    0.1038910          1.0000000
```

Zr:

```
240 9
INPUT
12 1 2 2 2 2 0
      1.0000000      0.0000000       0
      8.2000000    150.2675910       0
      4.0897280     18.9762160       0
      7.1100000     99.6221240       0
      3.5967980     14.1687330       0
      5.3500000     35.0451240       0
      2.4918210      6.1112590       0
      7.5400000    -21.0937760       0
      3.7700000     -3.0806940       0
0 0 3 2.0 1.0
      5.8737890             -0.9736630
      4.2872700              1.7091822
      1.4641370              0.2438310
0 0 1 2.0 1.0
      0.8312450              1.0000000
0 0 1 0.0 1.0
      0.3623350              1.0000000
0 2 2 6.0 1.0
      2.8742240             -4.2181013
      2.1199010              4.0479431
0 2 2 0.0 1.0
```

```
      0.8513640              0.5709451
      0.4372920              0.4621080
0 2 1 0.0 1.0
      0.2029040              1.0000000
0 3 3 2.0 1.0
      2.5801370             -0.16192069
      1.8553960              0.38451976
      0.6807540              0.81373290
0 3 1 0.0 1.0
      0.2566910              1.0000000
0 4 1 0.0 1.0
      0.485 1.0

O:

8 5
0 0 8 2.0 1.0
 8020.0       0.00108
 1338.0       0.00804
  255.4       0.05324
   69.22      0.1681
   23.90      0.3581
    9.264     0.3855
    3.851     0.1468
    1.212     0.0728
0 1 4 6.0 1.0
   49.43     -0.00883    0.00958
   10.47     -0.0915     0.0696
    3.235    -0.0402     0.2065
    1.217     0.379      0.347
0 1 1 0.0 1.0
    0.4520495     1.0        1.0
0 1 1 0.0 1.0
    0.1678880     1.0        1.0
0 3 1 0.0 1.0
    0.4509895     1.0
```

Oxygen vacancies were obtained removing one oxygen atom from the system. In general, the basis set of the former oxygen atom was kept in the vacant site (GHOST atom) for having a more complete set of functions also in the vacancy. To obtain the defect charge states +1 and +2, one and two electrons were, respectively, removed from the system. In the charge state +1, the calculations were performed at the unrestricted Kohn-sham level; in all the other cases, the closed-shell formalism was employed.

The bielectronic Coulomb and exchange integrals were truncated with the following truncation thresholds: 7, 7, 7, 7, 14 (see the CRYSTAL manual [58] for details about how this values affect the computation of the bielectronic integrals). The SCF convergence threshold was set to 10^{-8} E_h in all except lattice vibrations calculations, where it was set to 10^{-11} E_h. The reciprocal space integrals were calculated using a 8x8x8 Monkhorst-Pack net. In supercell calculations, the mesh was reduced to keep constant the number of point per unit of volume.

The equilibrium structure was obtained by allowing the system to relax toward a local minimum of the potential energy surface employing a gradient-based algorithm. The optimization process was considered complete once the forces acting on the nuclei had a value lower than $0.000\,45\,E_\mathrm{h}\,{a_0}^{-1}$.

Lattice vibrations were calculated in the harmonic approximation, through the frozen-phonons method (Section 2.3) displacing each atom along the Cartesian coordinates by 0.001 Å.

B. Choice of the Monkhorst-Pack mesh

First-principles calculations of periodic systems involve the calculation of integrals over the first Brillouin Zone (BZ). The integrals are approximated by finite sums evaluated only at a discrete number of reciprocal space points. Such points should be carefully selected in order to obtain a correct description of the system. Monkhorst and Pack discussed a method to generate an uniform mesh of equally-spaced points in the BZ [85] which became the standard in first-principles calculations of solids.

The generated mesh of points should be dense enough to obtain reliable results and it is therefore important to assess the quality of this grid by performing convergence tests. It is thus common practice to study the system total energy as a function on the number of reciprocal space points. The results of this test, obtained for $BaZrO_3$, are illustrated in Figure B.1.

To preserve the system cubic symmetry, we consider meshes defined by the same amount of points (*shrinking factor*, SF) along each of the three primitive reciprocal lattice vectors. The number of total point in the mesh is thus given by the SF to the power of three. Figure B.1 clearly shows that the electronic energy of $BaZrO_3$ rapidly converges with the number of points in the Monkhorst-Pack mesh. In addition, the 8^3-points mesh employed in this study can be considered dense enough, since the total energy obtained with such a grid differs only by around 0.005 meV with respect to the total energy calculated with the most dense grid comprising 32^3 points.

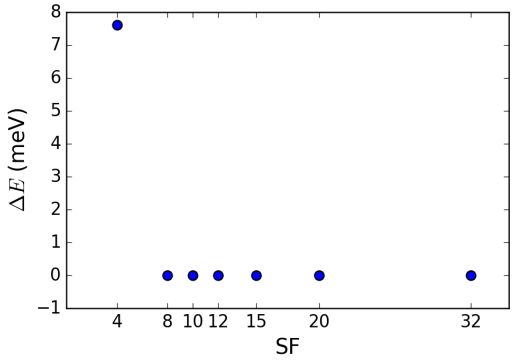

Figure B.1.: The plot shows how the system energy is affected by the number of points included in the Monkhorst-Pack mesh. ΔE represents the difference in the system electronic energy with respect to the value calculated employing the most dense mesh, which includes 32^3 points. The total number of points in the grid is determined by the shrinking factor, SF, and is given by SF^3.

C. Determination of the Valence Band Maximum in Charged Supercells

The energy of periodic systems is defined with respect to an arbitrary value, usually obtained by setting the system electrostatic Ewald potential to zero. Such reference is not only system dependent; but it is also affected by the system charge state. Therefore, a reliable calculation of the formation of charged defects requires to know this reference shift. In this appendix we outline a method, introduced by Bailey *et al.* [156], that can be used to estimate the reference shift. In particular, the method finds the charged system valence band maximum with respect to the energy reference used in the pristine bulk material. It is therefore useful to estimate the electron electrochemical potential of equation 3.62.

As discussed in Section 3.2.2, the term including both the system valence band maximum, ε_{VBM}, and the potential alignment can be calculated by considering the difference between the electronic energy of the pristine bulk system, $E_0(N)$, and of the same system without one electron, $E_0(N-1)$: $\epsilon_V = E_0(N) - E_0(N-1)$. Such a difference is however extremely affected by the presence of finite-size effects arising from the spurious electrostatic interactions present in the charged system needed to calculate $E_0(N-1)$. Therefore, ϵ_V should be calculated incrementing the supercell size until the value converges. Figure C.1 reports the calculated value of ϵ_V as a function of the supercell size. It is clear from the picture that, even for extremely large supercells, we are still far from reaching convergence. This is not surprising, considering the long range nature of the electrostatic forces affecting the charged systems. Therefore, to obtain the infinite supercell limit, we have fitted the calculated points using a function of the form $y = A + bL^{-1}$. According to the study of Makov and Payne discussed in Section 3.2.1, such a function describes how the electronic energy of a charged supercell asymptotically behaves with respect to the supercell size, L. We obtained the limit value of 9.21 eV for an infinitely large system and we use this value to estimate the electrochemical potential of electrons in systems with charged defects.

Note that in the CRYSTAL code, the potential alignment term included in the Freysoldt-Neugebauer-Van de Walle correction scheme (equation 3.82) takes into

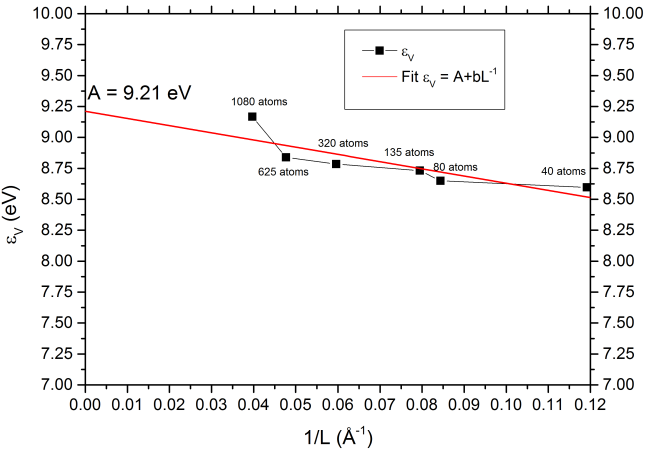

Figure C.1.: The plot shows how the quantity $\epsilon_V = E_0(N) - E_0(N-1)$ as a function of the reciprocal of the supercell size L^{-1}.

account only a part of the necessary alignment. The reason lies in the method employed to estimate the electrostatic potential in the CRYSTAL code, which is explained in reference [157]. To the best of our knowledge, the explicit calculation and extrapolation of ϵ_V is the only method which allows us to fully take into account the reference shift in the electronic energy of charged systems.

Bibliography

[1] I. H. Inoue. Electrostatic carrier doping to perovskite transition-metal oxides. *Semiconductor Science and Technology*, 20(4):S112, 2005.

[2] O. Muller and R. Roy. The major ternary structural families. Crystal chemistry of non-metallic materials. *Kristall und Technik*, 10(7):K86–K86, 1975.

[3] S. A. Bhalla, R. Guo, and R. Roy. The perovskite structure – a review of its role in ceramic science and technology. *Material Research Innovations*, 4(1):3–26, 2000.

[4] J. Richter, P. Holtappels, T. Graule, T. Nakamura, and L. J. Gauckler. Materials design for perovskite SOFC cathodes. *Monatshefte für Chemie - Chemical Monthly*, 140(9):985–999, 2009.

[5] H. Donnerberg. *Atomic Simulation of Electrooptic and Magnetooptic Oxide Materials*. Springer Berlin Heidelberg, Berlin, Heidelberg, 1999.

[6] M. E. Lines and A. M. Glass. *Principles and Applications of Ferroelectrics and Related Materials*. Oxford University Press, 2001.

[7] J. Zhu, H. Li, L. Zhong, P. Xiao, X. Xu, X. Yang, Z. Zhao, and J. Li. Perovskite oxides: Preparation, characterizations, and applications in heterogeneous catalysis. *ACS Catalysis*, 4(9):2917–2940, 2014.

[8] G. Pacchioni. Oxygen vacancy: The invisible agent on oxide surfaces. *Chem. Phys. Chem.*, 4(10):1041–1047, 2003.

[9] D. M. Smyth. Charge motion in ferroelectric thin films. *Ferroelectrics*, 116(1):117–124, 1991.

[10] W. L. Warren, G. E. Pike, K. Vanheusden, D. Dimos, B. A. Tuttle, and J. Robertson. Defect dipole alignment and tetragonal strain in ferroelectrics. *Journal of Applied Physics*, 79(12), 1996.

[11] A. Gruverman, O. Auciello, and H. Tokumoto. Nanoscale investigation of fatigue effects in Pb(Zr,Ti)O_3 films. *Applied Physics Letters*, 69(21), 1996.

[12] G. M. Choi and H. L. Tuller. Defect structure and electrical properties of single-crystal $Ba_{0.03}Sr_{0.97}TiO_3$. *Journal of the American Ceramic Society*, 71(4):201–205, 1988.

[13] S. Steinsvik, R. Bugge, J. Gjønnes, J. Taftø, and T. Norby. The defect structure of $SrTi_{1x}Fe_xO_{3y}$ (x = 00.8) investigated by electrical conductivity measurements and electron energy loss spectroscopy (EELS). *Journal of Physics and Chemistry of Solids*, 58(6):969 – 976, 1997.

[14] A. Lebon, P. Adler, C. Bernhard, A. V. Boris, A. V. Pimenov, A. Maljuk, C. T. Lin, C. Ulrich, and B. Keimer. Magnetism, charge order, and giant magnetoresistance in $SrFeO_{3-\delta}$ single crystals. *Phys. Rev. Lett.*, 92:037202, 2004.

[15] B. W. Veal and A. P. Paulikas. Dependence of hole concentration on oxygen vacancy order in $YBa_2Cu_3O_7$. *Physica C: Superconductivity*, 184(4):321 – 331, 1991.

[16] R. Merkle and J. Maier. How is oxygen incorporated into oxides? A comprehensive kinetic study of a simple solid-state reaction with $SrTiO_3$ as a model material. *Angewandte Chemie International Edition*, 47(21):3874–3894, 2008.

[17] C. Freysoldt, B. Grabowski, T. Hickel, J. Neugebauer, G. Kresse, A. Janotti, and C. G. Van de Walle. First-principles calculations for point defects in solids. *Rev. Mod. Phys.*, 86:253–305, 2014.

[18] W. Kohn and L. J. Sham. Self-consistent equations including exchange and correlation effects. *Phys. Rev.*, 140:A1133–A1138, 1965.

[19] J. P. Perdew, J. A. Chevary, S. H. Vosko, K. A. Jackson, M. R. Pederson, D. J. Singh, and C. Fiolhais. Atoms, molecules, solids, and surfaces: Applications of the generalized gradient approximation for exchange and correlation. *Phys. Rev. B*, 46:6671–6687, 1992.

[20] V. I. Anisimov, F. Aryasetiawan, and A. I. Lichtenstein. First-principles calculations of the electronic structure and spectra of strongly correlated systems: the LDA + U method. *Journal of Physics: Condensed Matter*, 9(4):767, 1997.

[21] C. Franchini. Hybrid functionals applied to perovskites. *Journal of Physics: Condensed Matter*, 26(25):253202, 2014.

[22] D. Ricci, G. Bano, G. Pacchioni, and F. Illas. Electronic structure of a neutral oxygen vacancy in srtio$_3$. *Phys. Rev. B*, 68:224105, 2003.

[23] E. A. Kotomin, Y. F. Zhukovskii, S. Piskunov, and D. E. Ellis. Hybrid DFT calculations of the F centers in cubic ABO_3 perovskites. *Journal of Physics: Conference Series*, 117(1):012019, 2008.

[24] J. Maier. *Physical Chemistry of Ionic Materials: Ions and Electrons in Solids*, pages 108–267. John Wiley & Sons, Ltd, 2005.

[25] J. Maier. Nanoionics: ion transport and electrochemical storage in confined systems. *Nat. Mater.*, 4:805–815, 2005.

[26] J. Maier. Nanoionics: ionic charge carriers in small systems. *Phys. Chem. Chem. Phys.*, 11:3011–3022, 2009.

[27] K. Reuter, C. Stampf, and M. Scheffler. *Handbook of Materials Modeling: Methods*, chapter Ab Initio Atomistic Thermodynamics and Statistical Mechanics of Surface Properties and Functions, pages 149–194. Springer Netherlands, Dordrecht, 2005.

[28] G. Shirane and Y. Yamada. Lattice-dynamical study of the 110K phase transition in $SrTiO_3$. *Phys. Rev.*, 177:858–863, 1969.

[29] P. A. Fleury. The effects of soft modes on the structure and properties of materials. *Annual Review of Materials Science*, 6(1):157–180, 1976.

[30] G. Venkataraman. Soft modes and structural phase transitions. *Bulletin of Materials Science*, 1(3):129–170, 1979.

[31] G. Shirane. Neutron scattering studies of structural phase transitions at Brookhaven. *Rev. Mod. Phys.*, 46:437–449, 1974.

[32] N. Choudhury, E. J. Walter, A. I. Kolesnikov, and C.-K. Loong. Large phonon band gap in $SrTiO_3$ and the vibrational signatures of ferroelectricity in $ATiO_3$ perovskites: First-principles lattice dynamics and inelastic neutron scattering. *Phys. Rev. B*, 77:134111, 2008.

[33] N. Sai and D. Vanderbilt. First-principles study of ferroelectric and antiferrodistortive instabilities in tetragonal srtio$_3$. *Phys. Rev. B*, 62:13942–13950, 2000.

[34] R. A. Evarestov, E. Blokhin, D. Gryaznov, E. A. Kotomin, and J. Maier. Phonon calculations in cubic and tetragonal phases of $SrTiO_3$: A comparative LCAO and plane-wave study. *Phys. Rev. B*, 83:134108, 2011.

[35] A. R. Akbarzadeh, I. Kornev, C. Malibert, L. Bellaiche, and J. M. Kiat. Combined theoretical and experimental study of the low-temperature properties of bazro$_3$. *Phys. Rev. B*, 72:205104, 2005.

[36] S. Yamanaka, M. Fujikane, T. Hamaguchi, H. Muta, T. Oyama, T. Matsuda, S. Kobayashi, and K. Kurosaki. Thermophysical properties of $BaZrO_3$ and $BaCeO_3$. *Journal of Alloys and Compounds*, 359(12):109 – 113, 2003.

[37] Y. Zhang, M. Liu, J. Wang, T. Shimada, and T. Kitamura. Strain tunable ferroelectric and dielectric properties of $BaZrO_3$. *Journal of Applied Physics*, 115(22), 2014.

[38] P. S. Dobal, A. Dixit, R. S. Katiyar, Z. Yu, R. Guo, and A. S. Bhalla. Micro-Raman scattering and dielectric investigations of phase transition behavior in the $BaTiO_3BaZrO_3$ system. *Journal of Applied Physics*, 89(12):8085–8091, 2001.

[39] S. Adachi, A. Kamitani, H. Wakana, and K. Tanabe. Deposition of SmBCO superconducting films on zr-rich $BaZrO_3$-buffered MgO substrates. *Superconductor Science and Technology*, 20(10):986, 2007.

[40] O. I. Aksimentyeva, V. P. Savchyn, V. P. Dyakonov, S. Piechota, Yu. Yu. Horbenko, I. Ye. Opainych, P. Yu. Demchenko, A. Popov, and H. Szymczak. Modification of polymer-magnetic nanoparticles by luminescent and conducting substances. *Molecular Crystals and Liquid Crystals*, 590(1):35–42, 2014.

[41] K.D Kreuer. Aspects of the formation and mobility of protonic charge carriers and the stability of perovskite-type oxides. *Solid State Ionics*, 125(14):285 – 302, 1999.

[42] K.D. Kreuer. Proton-conducting oxides. *Annual Review of Materials Research*, 33(1):333–359, 2003.

[43] E. Fabbri, A. D'Epifanio, E. Di Bartolomeo, S. Licoccia, and E. Traversa. Tailoring the chemical stability of $Ba(Ce_{0.8x}Zr_x)Y_{0.2}O_3$ protonic conductors for intermediate temperature solid oxide fuel cells (IT-SOFCs). *Solid State Ionics*, 179(1516):558 – 564, 2008.

[44] A. D'Epifanio, E. Fabbri, E. Di Bartolomeo, S. Licoccia, and E. Traversa. Design of $BaZr_{0.8}Y_{0.2}O_3$ protonic conductor to improve the electrochemical performance in intermediate temperature solid oxide fuel cells (IT-SOFCs). *Fuel Cells*, 8(1):69–76, 2008.

[45] A. B. Stambouli and E. Traversa. Fuel cells, an alternative to standard sources of energy. *Renewable and Sustainable Energy Reviews*, 6(3):295 – 304, 2002.

[46] C. Sun, R. Hui, and J. Roller. Cathode materials for solid oxide fuel cells: a review. *Journal of Solid State Electrochemistry*, 14(7):1125–1144, 2010.

[47] S. C. Singhal. Solid oxide fuel cells for stationary, mobile, and military applications. *Solid State Ionics*, 152153:405 – 410, 2002.

[48] A. Orera and P. R. Slater. New chemical systems for solid oxide fuel cells. *Chemistry of Materials*, 22(3):675–690, 2010.

[49] L. Malavasi, C. A. J. Fisher, and M. S. Islam. Oxide-ion and proton conducting electrolyte materials for clean energy applications: structural and mechanistic features. *Chem. Soc. Rev.*, 39:4370–4387, 2010.

[50] K. Katahira, Y. Kohchi, T. Shimura, and H. Iwahara. Protonic conduction in Zr-substituted $BaCeO_3$. *Solid State Ionics*, 138(12):91 – 98, 2000.

[51] N. Wakiya, N. Tajiri, T. Kiguchi, N. Mizutani, J. S. Cross, and K. Shinozaki. Activation energy of oxygen vacancy diffusion of Yttria-Stabilized-Zirconia thin film determined from DC current measurements below 150 C. *Japanese Journal of Applied Physics*, 45(6L):L525, 2006.

[52] F.A. Kröger and H. J. Vink. Relations between the concentrations of imperfections in crystalline solids. volume 3 of *Solid State Physics*, pages 307 – 435. Academic Press, 1956.

[53] E. Fabbri, D. Pergolesi, and E. Traversa. Materials challenges toward proton-conducting oxide fuel cells: a critical review. *Chem. Soc. Rev.*, 39:4355–4369, 2010.

[54] S. M. Haile, G. Staneff, and K. H. Ryu. Non-stoichiometry, grain boundary transport and chemical stability of proton conducting perovskites. *Journal of Materials Science*, 36(5):1149–1160, 2001.

[55] N. Bonanos, K.S. Knight, and B. Ellis. Perovskite solid electrolytes: Structure, transport properties and fuel cell applications. *Solid State Ionics*, 79:161 – 170, 1995. Proceedings of the 20th Commemorative Symposium on Solid State Ionics in Japan.

[56] H. Uchida, N. Maeda, and H. Iwahara. Relation between proton and hole conduction in $SrCeO_3$-based solid electrolytes under water-containing atmospheres at high temperatures. *Solid State Ionics*, 11(2):117 – 124, 1983.

[57] J. H. Shim, T. M. Gür, and F. B. Prinz. Proton conduction in thin film Yttrium-doped Barium Zirconate. *Applied Physics Letters*, 92(25), 2008.

[58] R. Dovesi, R. Orlando, A. Erba, C. M. Zicovich-Wilson, B. Civalleri, S. Casassa, L. Maschio, M. Ferrabone, M. De La Pierre, P. D'Arco, Y. Noël, M. Causá, M. Rérat, and B. Kirtman. CRYSTAL14: A program for the ab initio investigation of crystalline solids. *International Journal of Quantum Chemistry*, 114(19):1287–1317, 2014.

[59] B. T. Sutcliffe. *Fundamentals of Computational Quantum Chemistry*, pages 1–105. Springer Netherlands, Dordrecht, 1975.

[60] A. Szabo and N. S. Ostlund. *Modern Quantum Chemistry: Introduction to Advanced Electronic Structure Theory*. Dover Publications, INC., 1996.

[61] R. A. Evarestov. *Quantum Chemistry of Solids: LCAO Treatment of Crystals and Nanostructures*. Springer, 2007.

[62] P. Hohenberg and W. Kohn. Inhomogeneous electron gas. *Phys. Rev.*, 136:B864–B871, 1964.

[63] K. Capelle. A bird's eye view of density-functional theory. *[cond-mat.mtrl-sci]*, arXiv:cond-mat/0211443, 2006.

[64] P. A. M. Dirac. *Proc. Cambridge Phil. Soc.*, 26:376, 1930.

[65] D. M. Ceperley and B. J. Alder. Ground state of the electron gas by a stochastic method. *Phys. Rev. Lett.*, 45:566–569, 1980.

[66] R. Q. Hood, M. Y. Chou, A. J. Williamson, G. Rajagopal, R. J. Needs, and W. M. C. Foulkes. Quantum Monte Carlo investigation of exchange and correlation in silicon. *Phys. Rev. Lett.*, 78:3350–3353, 1997.

[67] R. Q. Hood, M. Y. Chou, A. J. Williamson, G. Rajagopal, and R. J. Needs. Exchange and correlation in silicon. *Phys. Rev. B*, 57:8972–8982, 1998.

[68] R. O. Jones and O. Gunnarsson. The density functional formalism, its applications and prospects. *Rev. Mod. Phys.*, 61:689–746, 1989.

[69] David C. Langreth and John P. Perdew. Theory of nonuniform electronic systems. I. Analysis of the gradient approximation and a generalization that works. *Phys. Rev. B*, 21:5469–5493, 1980.

[70] J. P. Perdew and W. Yue. Accurate and simple density functional for the electronic exchange energy: Generalized gradient approximation. *Phys. Rev. B*, 33:8800–8802, 1986.

[71] J. P. Perdew, K. Burke, and M. Ernzerhof. Generalized gradient approximation made simple. *Phys. Rev. Lett.*, 77:3865–3868, 1996.

[72] A. D. Becke. Density-functional exchange-energy approximation with correct asymptotic behavior. *Phys. Rev. A*, 38:3098–3100, 1988.

[73] C. Lee, W. Yang, and R. G. Parr. Development of the Colle-Salvetti correlation-energy formula into a functional of the electron density. *Phys. Rev. B*, 37:785–789, 1988.

[74] J. P. Perdew. Density functional theory and the band gap problem. *International Journal of Quantum Chemistry*, 28(S19):497–523, 1985.

[75] J. F. Janak. Proof that $\frac{\partial e}{\partial n_i} = \epsilon$ in density-functional theory. *Phys. Rev. B*, 18:7165–7168, 1978.

[76] J. P. Perdew, R. G. Parr, M. Levy, and J. L. Balduz. Density-functional theory for fractional particle number: Derivative discontinuities of the energy. *Phys. Rev. Lett.*, 49:1691–1694, 1982.

[77] L. J. Sham and M. Schlüter. Density-functional theory of the energy gap. *Phys. Rev. Lett.*, 51:1888–1891, 1983.

[78] J. P. Perdew and A. Zunger. Self-interaction correction to density-functional approximations for many-electron systems. *Phys. Rev. B*, 23:5048–5079, 1981.

[79] J. Tao, J. P. Perdew, V. N. Staroverov, and G. E. Scuseria. Climbing the density functional ladder: Nonempirical meta-generalized gradient approximation designed for molecules and solids. *Phys. Rev. Lett.*, 91:146401, 2003.

[80] A. D. Becke. A new mixing of HartreeFock and local density-functional theories. *The Journal of Chemical Physics*, 98(2), 1993.

[81] D. C. Langreth and J. P. Perdew. Exchange-correlation energy of a metallic surface: Wave-vector analysis. *Phys. Rev. B*, 15:2884–2901, 1977.

[82] A. D. Becke. Density-functional thermochemistry. III. the role of exact exchange. *The Journal of Chemical Physics*, 98(7), 1993.

[83] C. Adamo and V. Barone. Toward reliable density functional methods without adjustable parameters: The PBE0 model. *The Journal of Chemical Physics*, 110(13), 1999.

[84] J. P. Perdew, M. Ernzerhof, and K. Burke. Rationale for mixing exact exchange with density functional approximations. *The Journal of Chemical Physics*, 105(22), 1996.

[85] H. J. Monkhorst and J. D. Pack. Special points for Brillouin-zone integrations. *Phys. Rev. B*, 13:5188–5192, 1976.

[86] M. Catti. *Lattice Dynamics and Thermodynamic Properties*, pages 209–225. Springer Berlin Heidelberg, Berlin, Heidelberg, 1996.

[87] F. Pascale, C. M. Zicovich-Wilson, F. López Gejo, B. Civalleri, R. Orlando, and R. Dovesi. The calculation of the vibrational frequencies of crystalline compounds and its implementation in the CRYSTAL code. *Journal of Computational Chemistry*, 25(6):888–897, 2004.

[88] K. Doll, V. R. Saunders, and N. M. Harrison. Analytical HartreeFock gradients for periodic systems. *International Journal of Quantum Chemistry*, 82(1):1–13, 2001.

[89] X.-G. Wang, W. Weiss, Sh. K. Shaikhutdinov, M. Ritter, M. Petersen, F. Wagner, R. Schlögl, and M. Scheffler. The hematite (α- Fe_2O_3) (0001) surface: Evidence for domains of distinct chemistry. *Phys. Rev. Lett.*, 81:1038–1041, 1998.

[90] K. Reuter and M. Scheffler. Composition, structure, and stability of $RuO_2(110)$ as a function of oxygen pressure. *Phys. Rev. B*, 65:035406, 2001.

[91] J. Padilla and D. Vanderbilt. ***Ab initio*** study of $BaTiO_3$ surfaces. *Phys. Rev. B*, 56:1625–1631, 1997.

[92] M. W. Finnis. Accessing the excess: An atomistic approach to excesses at planar defects and dislocations in ordered compounds. *physica status solidi (a)*, 166(1):397–416, 1998.

[93] I. G. Batyrev, A. Alavi, and M. W. Finnis. Equilibrium and adhesion of Nb/sapphire: The effect of oxygen partial pressure. *Phys. Rev. B*, 62:4698–4706, 2000.

[94] B. Fultz. Vibrational thermodynamics of materials. *Progress in Materials Science*, 55(4):247 – 352, 2010.

[95] D. Yoshioka. *Statistical Physics*, pages 47–66. Springer Berlin Heidelberg, Berlin, Heidelberg, 2007.

[96] E. Heifets, E. A. Kotomin, Y. A. Mastrikov, S. Piskunov, and J. Maier. *Thermodynamics of ABO_3-type perovskite surfaces*, pages 491–518. In Tech, 2011.

[97] H. J. Monkhorst. Hartree-Fock density of states for extended systems. *Phys. Rev. B*, 20:1504–1513, 1979.

[98] W. Gao, T. A. Abtew, T. Cai, Y.-Y. Sun, S. Zhang, and P. Zhang. On the applicability of hybrid functionals for predicting fundamental properties of metals. *Solid State Communications*, 234235:10 – 13, 2016.

[99] P. P. Ewald. Die berechnung optischer und elektrostatischer gitterpotentiale. *Annalen der Physik*, 369(3):253–287, 1921.

[100] G. Makov and M. C. Payne. Periodic boundary conditions in *ab initio* calculations. *Phys. Rev. B*, 51:4014–4022, 1995.

[101] S. B. Zhang and J. E. Northrup. Chemical potential dependence of defect formation energies in GaAs: Application to Ga self-diffusion. *Phys. Rev. Lett.*, 67:2339–2342, 1991.

[102] J. Ihm, A. Zunger, and M. L. Cohen. Momentum-space formalism for the total energy of solids. *Journal of Physics C: Solid State Physics*, 12(21):4409, 1979.

[103] S. Lany and A. Zunger. Accurate prediction of defect properties in density functional supercell calculations. *Modelling and Simulation in Materials Science and Engineering*, 17(8):084002, 2009.

[104] M. Leslie and N. J. Gillan. The energy and elastic dipole tensor of defects in ionic crystals calculated by the supercell method. *Journal of Physics C: Solid State Physics*, 18(5):973, 1985.

[105] C. Freysoldt, J. Neugebauer, and C. G. Van de Walle. Fully *Ab Initio* finite-size corrections for charged-defect supercell calculations. *Phys. Rev. Lett.*, 102:016402, 2009.

[106] C. Freysoldt, J. Neugebauer, and C. G. Van de Walle. Electrostatic interactions between charged defects in supercells. *physica status solidi (b)*, 248(5):1067–1076, 2011.

[107] H.-P. Komsa, T. T. Rantala, and A. Pasquarello. Finite-size supercell correction schemes for charged defect calculations. *Phys. Rev. B*, 86:045112, 2012.

[108] H.-P. Komsa and A. Pasquarello. Finite-size supercell correction for charged defects at surfaces and interfaces. *Phys. Rev. Lett.*, 110:095505, 2013.

[109] S. Kim, K. J. Chang, and J.-S. Park. Finite-size supercell correction scheme for charged defects in one-dimensional systems. *Phys. Rev. B*, 90:085435, 2014.

[110] Y.-J. Gu, Z.-G. Liu, J.-H. Ouyang, Y. Zhou, and F.-Y. Yan. Synthesis, structure and electrical conductivity of $BaZr_{1x}Dy_xO_3$ ceramics. *Electrochimica Acta*, 75:332 – 338, 2012.

[111] W. B. Pearson. Landolt–Börnstein. Numerical data and functional relationships in science and technology. Group III. Crystal and solid state physics. Vol. 7. Crystal structure data of inorganic compounds. Parts a and g by W. Pies and A. Weiss. *Acta Crystallographica Section A*, 31(2):271–272, 1975.

[112] Bilbao Crystallographic Server. `http://http://www.cryst.ehu.es/`.

[113] R. A. Evarestov. Hybrid density functional theory LCAO calculations on phonons in Ba(Ti,Zr,Hf)O_3. *Phys. Rev. B*, 83:014105, 2011.

[114] R.I. Eglitis. Ab initio calculations of the atomic and electronic structure of $BaZrO_3$ (111) surfaces. *Solid State Ionics*, 230:43 – 47, 2013.

[115] A. Bilić and J. D. Gale. Ground state structure of $BaZrO_3$: A comparative first-principles study. *Phys. Rev. B*, 79:174107, 2009.

[116] T. S. Bjørheim, M. Arrigoni, D. Gryaznov, E. Kotomin, and J. Maier. Thermodynamic properties of neutral and charged oxygen vacancies in $BaZrO_3$ based on first principles phonon calculations. *Phys. Chem. Chem. Phys.*, 17:20765–20774, 2015.

[117] J. Robertson. Band offsets of wide-band-gap oxides and implications for future electronic devices. *Journal of Vacuum Science & Technology B*, 18(3):1785–1791, 2000.

[118] S. Parida, S. K. Rout, L. S. Cavalcante, E. Sinha, M. Siu Li, V. Subramanian, N. Gupta, V. R. Gupta, J. A. Varela, and E. Longo. Structural refinement, optical and microwave dielectric properties of $BaZrO_3$. *Ceramics International*, 38(3):2129 – 2138, 2012.

[119] L. P. Bouckaert, R. Smoluchowski, and E. Wigner. Theory of Brillouin zones and symmetry properties of wave functions in crystals. *Phys. Rev.*, 50:58–67, 1936.

[120] K. van Benthem, C. Elsässer, and R. H. French. Bulk electronic structure of $SrTiO_3$: Experiment and theory. *Journal of Applied Physics*, 90(12), 2001.

[121] R. E. Cohen and H. Krakauer. Electronic structure studies of the differences in ferroelectric behavior of $BaTiO_3$ and $PbTiO_3$. *Ferroelectrics*, 136(1):65–83, 1992.

[122] P. Otto. Calculation of the polarizability and hyperpolarizabilities of periodic quasi-one-dimensional systems. *Phys. Rev. B*, 45:10876–10885, 1992.

[123] M. Ferrero, M. Rérat, R. Orlando, and R. Dovesi. The calculation of static polarizabilities of 1-3D periodic compounds. the implementation in the CRYSTAL code. *Journal of Computational Chemistry*, 29(9):1450–1459, 2008.

[124] X. Gonze and C. Lee. Dynamical matrices, born effective charges, dielectric permittivity tensors, and interatomic force constants from density-functional perturbation theory. *Phys. Rev. B*, 55:10355–10368, 1997.

[125] Ph. Ghosez, J.-P. Michenaud, and X. Gonze. Dynamical atomic charges: The case of ABO_3 compounds. *Phys. Rev. B*, 58:6224–6240, 1998.

[126] W. Zhong, R. D. King-Smith, and D. Vanderbilt. Giant LO-TO splittings in perovskite ferroelectrics. *Phys. Rev. Lett.*, 72:3618–3621, 1994.

[127] C. H. Perry, D. J. McCarthy, and G. Rupprecht. Dielectric dispersion of some perovskite zirconates. *Phys. Rev.*, 138:A1537–A1538, 1965.

[128] J. W. Bennett, I. Grinberg, and A. M. Rappe. Effect of symmetry lowering on the dielectric response of $BaZrO_3$. *Phys. Rev. B*, 73:180102, 2006.

[129] B. Magyari-Köpe, L. Vitos, G. Grimvall, B. Johansson, and J. Kollár. Low-temperature crystal structure of $casio_3$ perovskite: An *ab initio* total energy study. *Phys. Rev. B*, 65:193107, 2002.

[130] S. Yamanaka, T. Hamaguchi, T. Oyama, T. Matsuda, S. Kobayashi, and K. Kurosaki. Heat capacities and thermal conductivities of perovskite type $BaZrO_3$ and $BaCeO_3$. *Journal of Alloys and Compounds*, 359(12):1 – 4, 2003.

[131] K. Kurosaki, R. J. M. Konings, F. Wastin, and S. Yamanaka. The low-temperature heat capacity and entropy of $SrZrO_3$ and $BaZrO_3$. *Journal of Alloys and Compounds*, 424(12):1 – 3, 2006.

[132] H. B. Callen. *Thermodynamics.* John Wiley & Sons, Inc., New York, N.Y., 1960.

[133] Y. .F. Zhukovskii, E. A. Kotomin, S. Piskunov, and D. E. Ellis. A comparative ab initio study of bulk and surface oxygen vacancies in $PbTiO_3$, $PbZrO_3$ and $SrTiO_3$ perovskites. *Solid State Communications*, 149(3334):1359 – 1362, 2009.

[134] R. I. Eglitis, N. E. Christensen, E. A. Kotomin, A. V. Postnikov, and G. Borstel. First-principles and semiempirical calculations for F centers in $KNbO_3$. *Phys. Rev. B*, 56:8599–8604, 1997.

[135] J. Carrasco, F. Illas, N. Lopez, E. A. Kotomin, Yu. F. Zhukovskii, R. A. Evarestov, Yu. A. Mastrikov, S. Piskunov, and J. Maier. First-principles calculations of the atomic and electronic structure of F centers in the bulk and on the (001) surface of $SrTiO_3$. *Phys. Rev. B*, 73:064106, 2006.

[136] M. J. S. Dewar and J. Kelemen. LCAO MO theory illustrated by its application to H_2. *Journal of Chemical Education*, 48(8):494, 1971.

[137] R. Evarestov, E. Blokhin, D. Gryaznov, E. A. Kotomin, R. Merkle, and J. Maier. Jahn-Teller effect in the phonon properties of defective $SrTiO_3$ from first principles. *Phys. Rev. B*, 85:174303, 2012.

[138] P. G. Sundell, M. E. Björketun, and G. Wahnström. Thermodynamics of doping and vacancy formation in $BaZrO_3$ perovskite oxide from density functional calculations. *Phys. Rev. B*, 73:104112, 2006.

[139] D. Gryaznov, E. Blokhin, A. Sorokine, E. A. Kotomin, R. A. Evarestov, A. Bussmann-Holder, and J. Maier. A comparative ab initio thermodynamic study of oxygen vacancies in ZnO and $SrTiO_3$: Emphasis on phonon contribution. *The Journal of Physical Chemistry C*, 117(27):13776–13784, 2013.

[140] M. I. Mendelev B. Bokstein and D. J. Srolovitz. *Thermodynamics and Kinetics in Material Science: A Short Course*. Oxford University Press, New York, N.Y., 2005.

[141] C. Yu, Z. Chen, J. J. Wang, W. Pfenninger, N. Vockic, J. T. Kenney, and K. Shum. Temperature dependence of the band gap of perovskite semiconductor compound $CsSnI_3$. *Journal of Applied Physics*, 110(6), 2011.

[142] K. J. Leonard, S. Sathyamurthy, and M. P. Paranthaman. Characterization of $BaZrO_3$ nanoparticles prepared by reverse micelle synthesis. *Chemistry of Materials*, 17(15):4010–4017, 2005.

[143] A. Calleja, X. Granados, S. Ricart, J. Oro, J. Arbiol, N. Mestres, A. E. Carrillo, X. Palmer, F. Cano, J. A. Tornero, T. Puig, and X. Obradors. High temperature transformation of electrospun $BaZrO_3$ nanotubes into nanoparticle chains. *CrystEngComm*, 13:7224–7230, 2011.

[144] R. I. Eglitis. First-principles calculations of $BaZrO_3$ (001) and (011) surfaces. *Journal of Physics: Condensed Matter*, 19(35):356004, 2007.

[145] E. Heifets, J. Ho, and B. Merinov. Density functional simulation of the $BaZrO_3$ (011) surface structure. *Phys. Rev. B*, 75:155431, 2007.

[146] J. Ho, E. Heifets, and B. Merinov. Ab initio simulation of the $BaZrO_3$ (001) surface structure. *Surface Science*, 601(2):490 – 497, 2007.

[147] Y. X. Wang, M. Arai, T. Sasaki, and C. L. Wang. First-principles study of the (001) surface of cubic $BaZrO_3$ and $BaTiO_3$. *Applied Physics Letters*, 88(9), 2006.

[148] E. Heifets, R. I. Eglitis, E. A. Kotomin, J. Maier, and G. Borstel. *Ab initio* modeling of surface structure for $SrTiO_3$ perovskite crystals. *Phys. Rev. B*, 64:235417, 2001.

[149] Thermodynamic properties of compounds, CaB_6 to BaO-WO_3: Datasheet from Landolt-Börnstein - group IV physical chemistry · volume 19a1. Copyright 1999 Springer-Verlag Berlin Heidelberg.

[150] Thermodynamic properties of compounds, SbO_2 to Rh_2O_3: Datasheet from Landolt-Börnstein - group IV physical chemistry · volume 19a4. Copyright 2001 Springer-Verlag Berlin Heidelberg.

[151] C. Kjølseth, L.-Y. Wang, R. Haugsrud, and T. Norby. Determination of the enthalpy of hydration of oxygen vacancies in Y-doped $BaZrO_3$ and $BaCeO_3$ by TG-DSC. *Solid State Ionics*, 181(3940):1740 – 1745, 2010.

[152] M. Shirpour, B. Rahmati, W. Sigle, P. A. van Aken, R. Merkle, and J. Maier. Dopant segregation and space charge effects in proton-conducting $BaZrO_3$ perovskites. *The Journal of Physical Chemistry C*, 116(3):2453–2461, 2012.

[153] M. Shirpour, R. Merkle, and J. Maier. Space charge depletion in grain boundaries of $BaZrO_3$ proton conductors. *Solid State Ionics*, 225:304 – 307, 2012. Solid State Ionics 18 Proceedings of the 18th International Conference on Solid State Ionics Warsaw, Poland, July 3 -8, 2011.

[154] M. Shirpour, G. Gregori, L. Houben, R. Merkle, and J. Maier. High spatially resolved cation concentration profile at the grain boundaries of Sc-doped $BaZrO_3$. *Solid State Ionics*, 262:860 – 864, 2014. Solid State Ionics 19 Proceedings of the 19th International Conference on Solid State Ionics.

[155] Stuttgart-Cologne pseudopotentials library. `http://www.tc.uni-koeln.de/PP/index.en.html`.

[156] C. L. Bailey, L. Liborio, G. Mallia, S. Tomić, and N. M. Harrison. Calculating charged defects using CRYSTAL. *Journal of Physics: Conference Series*, 242(1):012004, 2010.

[157] V. R. Saunders, C. Freyria-Fava, R. Dovesi, L. Salasco, and C. Roetti. On the electrostatic potential in crystalline systems where the charge density is expanded in Gaussian functions. *Molecular Physics*, 77(4):629–665, 1992.

Europass Curriculum Vitae

Personal information

Surname(s) / First name(s)	**Arrigoni, Marco**
Telephone(s)	+49-7116891738
Email(s)	m.arrigoni@fkf.mpg.de
Nationality(-ies)	Italian
Date of birth	06.06.1987

Education and training

Dates	August 2013 - to date
Occupation	PhD student in Chemistry
Name and type of organization providing education and training	Max Planck Institute for Solid State Research Department of Physical Chemistry of Solids (Prof. J. Maier) Stuttgart, Germany
Principal subjects/ occupational skills covered	First principles DFT calculations of point defects in oxides. *Ab initio* thermodynamic study of perovskite oxide surfaces. Atomistic DFT modeling of point defects in oxides at non-zero temperature.
Dates	December 2012 - June 2013
Occupation	Postgraduate Research Assistant
Name and type of organization providing education and training	Università degli Studi di Milano-Bicocca Department of Material Science - Quantum Chemistry Lab (Prof. G. Pacchioni) Milan, Italy
Principal subjects/ occupational skills covered	First principles DFT and QM/MM calculations of silica nanoparticle interfaces with water (continuation of Master's Thesis research).
Dates	September 2010 - November 2012
Title of qualification awarded	Master's degree in Material Science
Name and type of organization providing education and training	Università degli Studi di Milano-Bicocca Milan, Italy
Thesis title	Geometric and electronic structure of the silica-water interface as a function of the pH.
Dates	September 2006 - March 2010
Title of qualification awarded	Bachelor's degree in Material Science
Name and type of organization providing education and training	Università degli Studi di Milano-Bicocca Milan, Italy
Thesis title	Electronic structure of Bi-doped silica.
Dates	September 2001 - July 2006
Title of qualification awarded	High School Diploma
Name and type of organization providing education and training	Liceo Scientifico "G. Maironi da Ponte" Presezzo (BG), Italy

Personal skills and competences

Mother tongue(s)	**Italian**
Other language(s)	English (fluent), German (basic-intermediate)

Additional information

Publications

M. Arrigoni, E. A. Kotomin and J. Maier, First principles study of perovskite ultrathin films: stability and confinement effects. *Isr. J. Chem.* (in press)

M. Arrigoni, T. S. Bjørheim, E. A. Kotomin and J. Maier, First principles study of confinement effects for oxygen vacancies in $\mathrm{BaZrO_3}$ (001) ultra-thin films. *Phys. Chem. Chem. Phys.* **18**, 9902 (2016)

M. Arrigoni, E. A. Kotomin and J. Maier, Large-scale modeling of defects in advanced oxides: oxygen vacancies in $\mathrm{BaZrO_3}$ crystals. In *High Performance Computing in Science and Engineering 15*, Springer International Publishing Switzerland, 2016, pages 187-198

T. S. Bjørheim, *M. Arrigoni*, S. W. Saeed, E. A. Kotomin and J. Maier, Surface segregation entropy of protons and oxygen vacancies in $\mathrm{BaZrO_3}$. *Chem. Mater.* **28**(5), 1363 (2016)

T. S. Bjørheim, *M. Arrigoni*, D. Gryaznov, E. A. Kotomin and J. Maier, Thermodynamic properties of neutral and charged oxygen vacancies in $\mathrm{BaZrO_3}$ based on first principles phonon calculations. *Phys. Chem. Chem. Phys.* **17**, 20765 (2015)

M. Arrigoni, E. A. Kotomin, D. Gryaznov and J. Maier, Confinement effects for the F center in non-stoichiometric $\mathrm{BaZrO_3}$ ultrathin films. *Phys. Status Solidi B* **252**, 139 (2015)

M. A. Brown, *M. Arrigoni*, F. Héroguel, A. Beloqui Redondo, L. Giordano, J. A. van Bokhoven and G. Pacchioni, pH dependent electronic and geometric structure at the water-silica nanoparticle interface. *J. Phys. Chem. C* **118**, 29007 (2014)

Marco Arrigoni
Max Planck Institute for Solid State Research
Stuttgart, Germany
E-mail: m.arrigoni@fkf.mpg.de

List of attended conferences and workshops

Conferences:

- Oral contribution at the *E-MRS 2014 Spring Meeting*, Lille, France;
- Poster contribution at the *High Performance Computing Center Stuttgart 2014 Annual Workshop*, Stuttgart, Germany;
- Poster contribution at the *Materials Science and Technology Symposium 2014*, Pittsburgh, USA;
- Oral contribution at the *E-MRS 2015 Spring Meeting*, Lille, France;
- Poster contribution at the *20th International Conference on Solid State ionics*, Keystone (CO), USA;
- Oral contribution at the *High Performance Computing Center Stuttgart 2015 Annual Workshop*, Stuttgart, Germany;
- Oral contribution at the *E-MRS 2015 Spring Meeting*, Lille, France.

Workshops and Schools

- *Fortran for Scientific Computing*, High Performance Computing Center Stuttgart, Stuttgart, Germany;
- *Ab Initio Modeling in Solid State Chemistry - MSSC2015*, London, UK;
- *2016 University of Oslo Solid State Electrochemistry Winter Seminar*, Oslo, Norway;
- *Introduction to Unified Parallel C (UPC) and Co-array Fortran (CAF)*, High Performance Computing Center Stuttgart, Stuttgart, Germany;
- *International School of Electrochemical Energy Conversion and Storage*, Stuttgart, Germany;
- *Parallel Programming Workshop - MPI and Open MP for Beginners and Advanced Topics in Parallel Programming*, High Performance Computing Center Stuttgart, Stuttgart, Germany.